DETERMINING MULTILAYER FORMATION PROPERTIES FROM TRANSIENT TEMPERATURE AND PRESSURE MEASUREMENTS

A Dissertation

by

WEIBO SUI

Submitted to the Office of Graduate Studies of
Texas A&M University
in partial fulfillment of the requirements for the degree of

DOCTOR OF PHILOSOPHY

August 2009

Major Subject: Petroleum Engineering

DETERMINING MULTILAYER FORMATION PROPERTIES FROM TRANSIENT TEMPERATURE AND PRESSURE MEASUREMENTS

A Dissertation

by

WEIBO SUI

Submitted to the Office of Graduate Studies of
Texas A&M University
in partial fulfillment of the requirements for the degree of

DOCTOR OF PHILOSOPHY

Approved by:

Co-Chairs of Committee,	Christine Ehlig-Economides
	Ding Zhu
Committee Members,	A. Daniel Hill
	Yalchin Efendiev
Head of Department,	Stephen A. Holditch

August 2009

Major Subject: Petroleum Engineering

ABSTRACT

Determining Multilayer Formation Properties from Transient Temperature and Pressure Measurements. (August 2009)

Weibo Sui, B.S., China University of Petroleum (Beijing);

M.S., China University of Petroleum (Beijing)

Co-Chairs of Advisory Committee: Dr. Christine Ehlig-Economides
Dr. Ding Zhu

The Multilayer Transient Test is a well-testing technique designed to determine formation properties in multiple layers, and it has been proved effective during the past two decades. To apply the Multilayer Transient Test, a combination of rate profiles from production logs and transient rate and pressure measurements are required at multiple surface rates. Therefore, this method can be time consuming and may involve significant errors due to inaccurate transient flow rate measurements. A new testing approach is proposed after realizing the limitations of the Multilayer Transient Test. The new testing approach replaces the transient flow rate measurement with transient temperature measurement by using multiple temperature sensors. This research shows that formation properties can be quantified in multiple layers by analyzing measured transient temperature and pressure data.

A single-phase wellbore/reservoir coupled thermal model is developed as the forward model. The forward model is used to simulate the temperature and pressure response along the wellbore during the transient test. With the forward model, this work proves that the transient temperature and pressure are sufficiently sensitive to formation properties and can be used for multilayer reservoir characterization.

The inverse model is formulated by incorporating the forward model to solve formation properties using nonlinear least-square regression. For the hypothetical cases, the proposed new multilayer testing method has successfully been applied for investigating formation properties in commingled multilayer reservoirs. Layer

permeability, damaged permeability, and damaged radius can be uniquely determined using single-point transient pressure data and multipoint transient temperature data at appropriate locations. Due to the proposed data acquisition scheme, only one surface flow rate change is needed to implement this testing approach, which significantly reduces the test duration compared to the standard multilayer transient testing approach using a series of flow rate changes. Of special interest, this is the first test design that shows promise for determination of the damaged radius, which can be useful for well stimulation design. In addition, temperature resolution, data noise, and data rate impacts have been studied along with a data filtering approach that enable selection of suitable pressure and temperature sensor technologies for applying the new testing method.

DEDICATION

This dissertation is dedicated to my beloved parents Changfu Sui and Yaqin Zhang for their unconditional support and encouragement while I pursued my dream. This dissertation is also dedicated to my husband Jianye who has been being there assisting and understanding me during every step of my doctorate program, and to my wonderful son Jiarui.

ACKNOWLEDGEMENTS

I would like to express my gratitude to my co-advisors, Drs. Ehlig-Economides and Zhu, for their support, patience, and encouragement throughout my graduate studies. They also gave me innumerable lessons and insights on the workings of academic research in general, which will benefits my future research and work.

I also thank my committee members, Dr. Hill and Dr. Efendiev, for spending time in discussion with me and every precious advice throughout the course of this research.

Thanks also go to my friends and colleagues and the department faculty and staff for making my time at Texas A&M University a great experience.

NOMENCLATURE

A_j	coefficient defined in Eq. 2.112
$a_{\lg}$	logarithmic spatial transform coefficient
$a_{\lg t}$	logarithmic temporal transform coefficient
B_j	coefficient defined in Eq. 2.102
b_j	coefficient for outer boundary condition
C	wellbore storage coefficient
C_D	dimensionless wellbore storage coefficient
C_f	reservoir rock compressibility
C_p	heat capacity of fluid
C_{pr}	heat capacity of formation rock
$\mathbf{C}_n$	weight matrix for observations
c_t	total system compressibility
D	bottom depth of reservoir
$\mathbf{d}$	observation data
$d\hat{q}_i$	normalized layer flow rate change
E	energy
E_{KE}	kinetic energy
E_{VS}	viscous shear energy term
$\mathbf{e}$	intermediate vector
f	friction factor
$\mathbf{f}$	objective function
$\mathbf{G}$	sensitivity matrix
$\mathbf{g}$	predicted data

g	gravity acceleration
g_T	geothermal gradient
$\mathbf{H}$	Hessian matrix
H	enthalpy
h	thickness
h_a	heat convection coefficient
$\mathbf{I}$	identity matrix
$\mathbf{J}$	Jacobian matrix
I_0, K_0	zero order modified Bessel function of the first and second kind
I_1, K_1	first order modified Bessel function of the first and second kind
K_T	thermal conductivity
K_{JT}	Joule-Thomson coefficient
k	permeability
k_s	damage permeability
M	number of time points used for regression
$m(p)$	pseudo-pressure function
N	number of producing layers in reservoir system
N_p	cumulative production rate
NT	number of time step during a transient flow test
n	number of layers in reservoir system
p	pressure
p_i	reservoir initial pressure
p_{wf}	flowing bottomhole pressure
p_j	reservoir pressure in layer j
p_{jD}	dimensionless reservoir pressure in Layer j
p_{sc}	pressure under standard condition

$\mathbf{q}$	conductive heat flux
q	surface production rate
$q_{bc,j}$	flow rate before surface rate change in Layer j
q_j	flow rate for Layer j
q_{jD}	dimensionless flow rate for Layer j
q_{last}	last production rate before rate change
R	wellbore radius
r	radial coordinate
r_D	dimensionless radial distance
r_e	reservoir outer radius
r_{eD}	dimensionless reservoir outer radius
r_s	damage radius
r_{ti}	tubing inner radius
r_{wb}	wellbore radius
s	skin factor
s_j	skin factor in Layer j
T	temperature
T_e	temperature at external boundary of reservoir
T_{Ge}	geothermal temperature
T_I	inflow temperature
T_{sc}	temperature under standard condition
t	time
t_D	dimensionless time reference to Layer j
t_N	total time length of the transient test
t_{pH}	pseudoproducing time

U	internal energy
U_T	overall heat transfer coefficient
V	volume
$\mathbf{v}$	velocity vector
v	velocity
$\mathbf{x}$	parameter vector
$\mathbf{w}$	derivative vector
z	vertical coordinate

Greek

β	thermal expansion coefficient
γ	pipe open ratio
$\delta\mathbf{x}$	upgrading parameter
θ	wellbore inclination
ι	Laplace space variable
κ	permeability-thickness fraction
λ	Marquardt parameter
μ	viscosity
π	total molecular stress tensor
ρ	density
$\boldsymbol{\tau}$	shear stress tensor
ϕ	porosity
ω	porosity-thickness fraction

Superscripts

n	time step index
$\mathbf{T}$	matrix transform

Subscripts

c	calculated pressure or temperature data
f	formation fluid
I	inflow
i, j, k	position index
m	iteration step
NR	number of grid block in r direction
NZ	number of grid block in z direction
o	observed pressure or temperature data
r	radial direction; rock
T	total
wb	bulk wellbore properties
z	vertical direction

TABLE OF CONTENTS

Page

Page

LIST OF FIGURES

Page

Page

Page

Page

LIST OF TABLES

Page

1 INTRODUCTION

1.1 BACKGROUND

In most multilayered reservoirs, individual productive layers usually develop different thickness, porosity, permeability, and skin factor. An evaluation of multilayer formation properties will benefit well performance and stimulation design. With a good knowledge of multilayer formation properties, differential depletion may be predicted and stimulation design may be improved greatly. Therefore, multilayer reservoir characterization has a significant effect on production management.

Multilayer Transient Test (MLT) is a well testing method that is designed for determining individual layer properties (permeability and skin) for multiple layers commingled in a well, and this testing method has proven effective during the past two decades. However, traditional MLT requires a combination of rate profiles from production log and transient rate and pressure measurements acquired at multiple surface rates. This method can be time consuming and may involve significant errors depending on the accuracy of the transient flow rate measurements.

Recent interest in the installation of permanent downhole pressure and temperature sensors may provide a new opportunity for multilayer reservoir characterization. Current downhole sensors enable monitoring downhole pressure and temperature in real time. With multiple downhole temperature sensors, the temperature variations as a function of time and depth can be recorded without any intervention. Motivated by the emerging monitoring technology, an entirely new testing and analysis approach is proposed in this study. Instead of the transient rate profiles measured by a production logging string, we propose to use downhole transient temperature and pressure measurements for evaluating individual layer properties (permeability, damage radius, damage permeability) in multilayered reservoirs.

This dissertation follows the style of *SPE Journal.*

1.2 LITERATURE REVIEW

1.2.1 Multilayer Transient Test

Most oil and gas reservoirs are stratified with different layer properties as a result of sedimentary depositional processes. Since layer properties are critical information for multilayer commingled production, many testing and analysis approaches have been presented to understand the behavior of multilayered reservoir and to quantify formation properties.

Lefkovits (1961) was the precursor of studying the behavior of commingled multilayer reservoirs. In his work, after presenting detailed mathematical derivation for a two-layer commingled reservoir, the buildup curves were analyzed to determine the average formation properties such as permeability-thickness product, the wellbore damage and the static pressure. He also found that early-time layer flow rate was governed basically by permeability thickness product and skin, and the late-time flow rate increasingly depends on oil-filled volume and compressibility. Nevertheless, individual layer properties cannot be determined from his method. Following Lefkovits' work, many authors improved his mathematical model. They extended the commingled system to interlayer formation crossflow system, and the number of layers can be arbitrary. A comprehensive literature survey can be found in Ehlig-Economides' work (1987). However, those methods still used conventional drawdown or buildup tests, from which the individual layer properties cannot be interpreted for more than two-layer reservoirs.

Although rigorous mathematical models for the multilayered reservoir have been developed by many authors, the quantitative interpretation technique was first introduced by a series of studies in 1980s. Kuchuk et al. (1986a) first presented a new testing and analysis technique called "multilayer test", which made it possible to uniquely determine individual-layer permeabilities and skin factors for reservoirs with commingled layers. Their multilayer testing technique starts with the well flowing at a constant production or injection rate. A production log (PL) flow rate survey is acquired during stabilized flow. Then the flow meter is stationed above one of the layers to be characterized, and a step

change in surface rate is made while the PL string is kept in a stationary position. After some time, usually several hours, another flow rate survey is acquired, the PL string is stationed above another of the layers, and the surface flow rate is changed again. The test continues repeating these same steps until transient measurements of pressure and flow rate have been made above each of the layers to be characterized. In the multilayer transient test analysis (Ehlig-Economides, 1987), stabilized profile data are used to determine individual layer pressures, and transient pressure and flow rate data are used to estimate individual layer properties using nonlinear least-squares regression. Based on their analysis method, a field example was presented by Kuchuk et al. (1986b) and good results were achieved, which proved the effectiveness of multilayer tests.

Ehlig-Economides (1987) presented the analytical solutions for both commingled and interlayer crossflow reservoirs with arbitrary number of layers and took into account the effects of skin and wellbore storage in solutions. Such analytical solutions provided the theoretical support for multilayer test technique. However, their data acquisition technique of acquiring simultaneous measurement of both flow rate and pressure following a single rate change has been done only once in the field, even though it did provide a much shorter test duration. By introducing the step-wise changes in the surface flow rates, Shah et al. (1988) made the Ehlig-Economides model (1987) applicable in practice.

The more general analytic solution for multilayer test in commingled reservoirs was presented by Kuchuk and Wilkinson (1991) later on. Their solutions are applicable to a variety of commingled reservoir systems in which individual layers may have different initial and outer-boundary conditions. The vertical wellbore can commingle layers with completely general model characterizations including partially penetrated or vertically fractured wellbores, dual porosity, the usual boundary options, and even a horizontal lateral. Their study extended the application of the multilayer test in practice.

During the past decades, the multilayer test technique has been gradually improved by some meaningful works (Spath et al., 1994; Larsen, 1999; Prats et al., 1999) and has been applied for more complex reservoir and wellbore conditions. Since

the fundamental principles are still the same, the inherent drawback cannot be eliminated. Relatively long testing duration will undoubtedly impact production, and the possibly inaccurate transient flow rate measurement may also jeopardize later analysis results. Recently, some authors (Spivey, 2006; Poe et al., 2006; Manrique and Poe, 2007) proposed combining production data with PL rate surveys spaced over time, avoiding the need for multirate testing. However, their approach requires multiple production logs to be run to get the transient layer flow rate information during a long production period, thereby requiring several interventions for the PL data acquisition.

The multilayer testing models have enabled the observation of the characteristics of multilayer reservoir behavior. The testing techniques depend on the acquisition of transient downhole pressure and layer flow rate data that are sensitive to layer properties. The new testing approach proposed in this research work was prompted by the successful working principles of traditional multilayer tests. In this work, the transient flow rate measurements are replaced by transient temperature measurements, which are combined with transient pressure measurement for determination of individual layer permeability and skin values.

1.2.2 Downhole Temperature Monitoring

As an important component of production logs, temperature log has been used for many years in oil and gas industry. Several major applications (Hill, 1990) of temperature logging include detecting location of gas entries, detection of casing leaks and fluid movement behind casing, detecting location of lost-circulation zones, evaluation of cement placement, and qualitative identification of injection or production zones.

In recent years, with a popular application of intelligent wells in oil and gas industry, some new techniques have been introduced for downhole temperature monitoring, and downhole temperature has started attracting interest again as an effective tool for real-time production and reservoir management. Current downhole temperature monitoring technology uses either fiber-optic temperature sensors or a temperature sensor array system.

The representative products of fiber-optic temperature sensors are Distributed Temperature Sensor System (DTS) and Fiber Bragg Grating Sensor (FBG) (Grattan and Sun, 2000). The DTS system has the advantage of making the distributed sensing for temperature along the wellbore in real time, and numerous works about DTS applications have been published in recent years (Carnahan et al., 1999; Kragas et al., 2001; Johnson et al., 2006; Nath et al., 2007; Mahrooqi et al., 2007.). Although the temperature sensors with the FBG technique can only measure temperature at specific points instead of distributed sensing, the FBG technique is also attractive in some situations due to a higher temperature resolution and accuracy it can realize.

Another option for downhole temperature monitoring is the digital temperature sensor array system which consists of many high-resolution miniature digital temperature sensors. The proposed testing technique in this work has not get field demonstration, any of the above mentioned temperature sensors satisfy the hardware requirement. The selection for practical application will depend on specific resolution requirements and well completion types.

1.2.3 Transient Temperature Modeling and Interpretations

The temperature modeling and interpretation originated together with the application of temperature logging, which has been used in various applications since Schlumberger et al. (1937) identified its usefulness in 1930s. Corresponding to the various applications, the investigators have presented a number of models to simulate steady-state or transient temperature variations.

Many early models were based on the line-source solutions given by Carslaw and Jaeger (1959). Ramey (1962) proposed an approximate method for predicting temperature of either a single-phase incompressible liquid or a single-phase ideal gas flowing in injection or production wells. Ramey's method assumes that heat transfer in the wellbore is steady-state, while heat transfer to the earth is represented as unsteady radial conduction. This result in a simplified time function giving reasonably accurate results after sufficient time has elapsed.

Satter (1965) improved Ramey's method by considering phase changes occurring within steam-injection projects. Sagar et al. (1991) extended Ramey's method for wellbore with multiphase flow, accounting for kinetic energy and Joule-Thompson effects. Hasan and Kabir (1991) later complemented Ramey's method by studying the early-time thermal behavior and adopting an appropriate inner boundary condition at the formation/wellbore interface that was represented by the Fourier's law of heat conduction. In Hasan's work, the superposition principle was used to account for the gradual changes in heat transfer rate between the wellbore and the formation.

To simplify the heat transfer problem in the formation and obtain analytical solutions, most existing temperature models were developed for studying the temperature distribution above productive intervals. Some numerical thermal models coupled the wellbore and reservoir together and can consider the heat convection in productive intervals, but usually these models neglect small thermal effects such as decompression of the fluid and the frictional heating that occurs in the formation.

In this research work, sufficient resolution in the transient temperature profiles measured across reservoir intervals is prerequisite, and they must also be predicted accurately by a forward model. Therefore, a rigorous numerical wellbore/reservoir coupled thermal model must be formulated, and small thermal effects must be rigorously addressed. An existing thermal simulator developed by Maubeuge et al. (1994a and 1994b) considered the Joule-Thomson effect that occurs in the formation and is the precursor to the forward model in this work. The Maubeuge et al. model can be used for simulation of multilayered temperature variation in the reservoir, but their simulator does not have a rigorous wellbore simulator to calculate transient wellbore temperature variations and is therefore not sufficient for this research.

In recent years, with the rapid development of permanent temperature sensors, the new temperature measurement technology has encouraged new studies emphasizing quantitative temperature interpretations. Until now, quantitative temperature interpretations have been mainly focused on flow profiling aimed at obtaining flow rate distribution along productive intervals (Yoshioka et al., 2005a, 2005b, 2007a, and

2007b; Brown et al., 2003; Ouyang and Belanger, 2006; Pinzon et al., 2007), and a steady-state thermal model was used in those works.

Assuming the availability of distributed pressure and temperature measurements, Yoshioka (2007) developed a multiphase steady-state wellbore/reservoir thermal model to detect the gas/water breakthrough in a horizontal production well. The Yoshioka et al. model first coupled a rigorous wellbore and reservoir model together to investigate the temperature variations along the wellbore and inside the formation considering the small thermal effects. Since the Yoshioka et al. model is only applicable for steady-state flow conditions; it cannot be used to determine layer permeability and skin simultaneously. In their simulator, the reservoir flow model is using pseudo-steady-state horizontal well productivity equation, and the reservoir thermal model is derived from 1D steady-state energy balance equation. In this study, the rigorous multiphase wellbore model developed by Yoshioka et al. will be simplified for single-phase liquid or gas flow, and then coupled with the newly developed transient reservoir flow/thermal model.

Similarly, based on steady temperature analysis, other studies (Brown et al., 2005; Fryer et al., 2005; Lanier et al., 2003; Pinzon et al., 2007) presented some flow profile interpretation results based on DTS field data. Concerning the problem of solution nonuniqueness, they suggested that for a new well, layer permeability is the most possible parameter to be adjusted to obtain a fit between DTS-measured temperature profiles and the model output; while the later time temperature fit should be achieved by adjusting layer pressures or fluid properties. Basically, all of those models suffer from the fundamental limitation that the steady-state flow offers are equations for several unknowns.

This work will show that the current steady-state temperature interpretation cannot provide layer permeability and skin simultaneously. Additionally, the distributed temperature profiles are not required in the new proposed testing technology. Instead multipoint array temperature measurements may be better for the proposed approach.

1.3 OBJECTIVES

Multilayer Transient Tests have been used for detailed characterization of multilayered reservoirs. However, the long duration of the test and possible flow rate measurement errors limit its application in field. Inspired by the successful working principles of Multilayer Transient Tests, we will develop a new testing approach for evaluating individual layer properties. The objective of this study is to determine layer permeability and damage skin factor from transient pressure and temperature measurements. The transient downhole pressure is measured by the permanent downhole pressure gauge and is used to reveal the behavior of the total system, while the transient temperature is recorded by downhole temperature sensors and is used to reveal the behavior of individual producing intervals. Although distributed temperature data have been investigated by many authors for flow profiling, no previous studies used temperature data to evaluate formation properties in multilayered reservoirs. Additionally, it should be noted that the skin factor addressed in this study is formation damage skin. The proposed new testing approach may enable quantification of the skin as an independent parameter, which has never been shown in previous studies.

This dissertation is written in six sections. In Section 1, the research background and objective are introduced, and the available literature about Multilayer Transient Test, downhole temperature monitoring and transient temperature modeling and interpretation are reviewed. In Section 2, a rigorous wellbore/reservoir coupled thermal model is established as the forward model. Section 3 presents the solutions for the forward model and the forward model validation in three different ways. An illustrative example is also presented to show the simulation results from the forward model. Section 4 develops the inverse model formulation, and presents the proposed test procedure in detail. In Section 5, we present the results of feasibility studies of model application and a hypothetical case is used to illustrate the whole testing and analysis procedure. Some practical implications about this model are also discussed in this part. In the end, we draw conclusions based on the preceding results and discussions in Section 6.

2 FORWARD MODEL

2.1 INTRODUCTION

In this section, a forward model is established to simulate transient temperature and pressure behavior during the transient flow test. The forward model consists of a wellbore model and a reservoir model.

The wellbore model includes a wellbore flow model and a wellbore thermal model. The wellbore flow model is formulated by mass balance and momentum balance, and the wellbore thermal model is formulated by energy balance equations. The wellbore flow model is used for solving wellbore fluid velocity and pressure profiles, and the wellbore flowing fluid temperature profiles are solved from the wellbore thermal model. In this research work, the wellbore flow model is treated as sequential steady-state and the thermal model is treated as transient since wellbore fluid flow will become stabilized much faster than the wellbore fluid heat transfer process. At each time step, wellbore flowing fluid velocity, pressure, and temperature profiles are updated by using reservoir information.

On the reservoir side, the reservoir model includes the flow part and thermal part. The reservoir flow model is derived based on Multilayer Transient Testing theory and is solved analytically. The reservoir thermal model is formulated by transient energy balance equation considering various subtle thermal effects in the formation.

The wellbore and reservoir models are coupled together by applying appropriate boundary conditions and are solved iteratively in next Section.

---

* Part of this chapter is reprinted with permission from "Model for Transient Temperature and Pressure Behavior in Commingled Vertical Wells" by Sui, W., Zhu, D., Hill, A.D., and Ehlig-Economides, C., 2007. Paper SPE 115200 presented at the SPE Russian Oil & Gas Technical Conference and Exhibition, Moscow, Russia, 28-30 October.

2.2 WELLBORE MODEL

In this section, the steady-state wellbore flow model and the transient wellbore thermal model will be established by deriving mass, momentum, and energy balance equations over a differential volume element that is shown in **Fig. 2.1**.

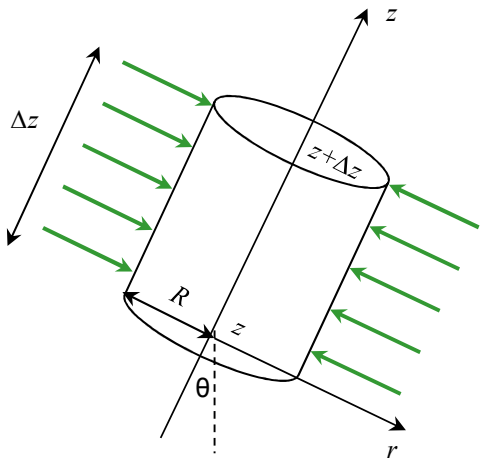

Fig. 2.1 Differential volume element of a wellbore

2.2.1 Wellbore Flow Model

Here the wellbore flow model developed by Yoshioka (2007) is simplified for single-phase fluid flow to simulate wellbore flowing fluid velocity and pressure profiles in vertical or deviated producing wells. The velocity vector we are using here has three components and it could be represented by

$$\mathbf{v} = \begin{pmatrix} v_z \\ v_r \\ v_\theta \end{pmatrix} = \begin{cases} \begin{pmatrix} v \\ 0 \\ 0 \end{pmatrix} & \text{otherwise} \\ \\ \begin{pmatrix} 0 \\ v_I \\ 0 \end{pmatrix} & \text{at } r = R \end{cases} \qquad \text{.....2.1}$$

where the subscript *I* means inflow properties. Equation 2.2 indicates that there is no slip at wall ($r = R$) and the radio velocity only exists at the wall. Thus the axial velocity will be represented by v and the radial velocity is represented by v_I in later derivations.

Mass balance

Conservation of mass can be derived using the incoming mass flux and outgoing mass flux as

$$\begin{bmatrix}\text{rate of}\\ \text{increase}\\ \text{of mass}\end{bmatrix} = \begin{bmatrix}\text{rate of}\\ \text{mass}\\ \text{in}\end{bmatrix} - \begin{bmatrix}\text{rate of}\\ \text{mass}\\ \text{out}\end{bmatrix} \quad \text{.....2.2}$$

To consider different completion types such as open hole and perforated liner, we introduce a pipe open ratio parameter as

$$\gamma = \frac{\text{Open area of pipe}}{\text{Surface area of pipe}} \quad \text{.....2.3}$$

The physical meaning of γ can be understood from **Fig. 2.2** . From **Fig. 2.2**, we can see that the open area of the pipe can be expressed using γ as $2\pi R\gamma\Delta z$.

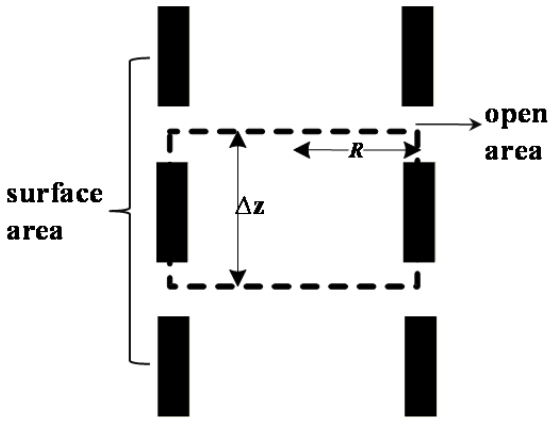

Fig. 2.2 Pipe open ratio definition

Considering the fluid is entering into the volume element from bottom in z direction and from the wall at $r = R$, the mass balance equation is given as follows.

$$\pi R^2 \Delta z \frac{\partial \rho}{\partial t} = 2\pi R \gamma \Delta z (\rho_I v_I) + \pi R^2 (\rho v)_z - \pi R^2 (\rho v)_{z+\Delta z} \quad \text{.....2.4}$$
$$= 2\pi R \gamma \Delta z \rho_I v_I + \pi R^2 [(\rho v)_z - (\rho v)_{z+\Delta z}]$$

After rearrangement and simplification, taking the limit of $\Delta z \to 0$ yield,

$$\frac{\partial \rho}{\partial t} = \frac{2\gamma}{R} \rho_I v_I - \frac{\partial}{\partial z}(\rho v) \quad \text{.....2.5}$$

For steady-state condition, we have

$$\frac{\partial}{\partial z}(\rho v) = \frac{2\gamma \rho_I v_I}{R} \quad \text{.....2.6}$$

Momentum balance

Similarly, the moment balance over the volume element is written as

$$\begin{bmatrix} \text{rate of} \\ \text{increase} \\ \text{of momentum} \end{bmatrix} = \begin{bmatrix} \text{rate of} \\ \text{momentum} \\ \text{in} \end{bmatrix} - \begin{bmatrix} \text{rate of} \\ \text{momentum} \\ \text{out} \end{bmatrix} + \begin{bmatrix} \text{external} \\ \text{force on} \\ \text{the fluid} \end{bmatrix} \quad \text{.....2.7}$$

In the defined system, we assume there is only single-phase Newtonian fluid flow, only z-momentum is considered and there is no slip on the wall. The external force on the fluid is gravity. The steady-state condition is used here, thus the momentum balance equation can be given by

$$\frac{dp}{dx} = -\frac{\rho v^2 f}{R} - \frac{d(\rho v^2)}{dx} - \rho g \sin\theta \quad \text{.....2.8}$$

where *f* in the first term of the RHS of the equation denotes the frictional factor.

2.2.2 Wellbore Thermal Model

The wellbore thermal model is used to describe wellbore temperature behavior during a transient test. Conservation of energy can be similarly derived by considering the incoming and outgoing energy flux, work done by external forces and other possible sources in system,

$$\begin{bmatrix}\text{rate of}\\ \text{increase of}\\ \text{energy}\end{bmatrix}=\begin{bmatrix}\text{rate of}\\ \text{energy in}\end{bmatrix}-\begin{bmatrix}\text{rate of}\\ \text{energy out}\end{bmatrix}+\begin{bmatrix}\text{rate of}\\ \text{work done on system}\\ \text{by external forces}\end{bmatrix}+\begin{bmatrix}\text{source}\end{bmatrix} \quad \text{.....2.9}$$

Since the total energy is transported by three different mechanisms of (a) the convective mechanism, (b) the work done by molecular mechanisms, and (c) the heat transported by molecular mechanisms, here we introduce the combined energy flux vector to help derive the energy balance equation. The combined energy flux vector $\mathbf{e}$ is defined as (Bird et al., 2002)

$$\mathbf{e}=\left(\frac{1}{2}\rho v^2+\rho\hat{U}\right)\mathbf{v}+\left[\boldsymbol{\pi}\cdot\mathbf{v}\right]+\mathbf{q} \quad \text{.....2.10}$$

where the first term of Eq. **2.10** represents the energy transported by convection, $\hat{U}$ denotes the internal energy; the second term represents the energy transported by molecular mechanisms and $\boldsymbol{\pi}$ denotes the molecular stress tensor, the last term represents the energy transported by heat $\mathbf{q}$. And the total molecular stress tensor $\boldsymbol{\pi}$ can be split into two parts: $\boldsymbol{\pi}=p\boldsymbol{\delta}+\boldsymbol{\tau}$ where p means the normal stress and $\boldsymbol{\tau}$ means the shear stress, so that $\left[\boldsymbol{\pi}\cdot\mathbf{v}\right]=p\mathbf{v}+\left[\boldsymbol{\tau}\cdot\mathbf{v}\right]$. According to the definition of enthalpy H,

$$H=U+\frac{p}{\rho} \quad \text{.....2.11}$$

Eq. **2.10** can be written as the general form of energy flux,

$$\mathbf{e}=\left(\frac{1}{2}\rho v^2+\rho\hat{H}\right)\mathbf{v}+\left[\boldsymbol{\tau}\cdot\mathbf{v}\right]+\mathbf{q} \quad \text{.....2.12}$$

The rate of increase of energy of the volume element $\pi R^2\Delta z$ is

$$\begin{bmatrix}\text{rate of}\\ \text{increase of}\\ \text{energy}\end{bmatrix}=\pi R^2\Delta z\frac{\partial}{\partial t}\left(\frac{1}{2}\rho v^2+\rho\hat{U}\right) \quad \text{.....2.13}$$

in which $\frac{1}{2}\rho v^2$ is the kinetic energy per unit volume and $\rho\hat{U}$ is the internal energy per unit volume.

The rate of energy in is

$$\begin{bmatrix}\text{rate of}\\ \text{energy in}\end{bmatrix} = 2\pi R\Delta z\left(e_r\right)_R + \pi R^2\left(e_z\right)_z \quad \text{.....2.14}$$

where e_r and e_z denote the combined energy flux components in radial and vertical direction respectively.

The rate of energy out is

$$\begin{bmatrix}\text{rate of}\\ \text{energy out}\end{bmatrix} = \pi R^2\left(e_z\right)_{z+\Delta z} \quad \text{.....2.15}$$

Since here we only have gravity forces, the rate of work done on system by external forces is

$$\begin{bmatrix}\text{rate of}\\ \text{work done on system}\\ \text{by external forces}\end{bmatrix} = -\pi R^2\Delta z\rho vg\sin\theta \quad \text{.....2.16}$$

The source term is zero. Substituting Eqs. **2.13** to **2.16** into Eq. **2.9** yields

$$\pi R^2\Delta z\frac{\partial}{\partial t}\left(\frac{1}{2}\rho v^2 + \rho\hat{U}\right) = 2\pi R\Delta z\left(e_r\right)_R + \pi R^2\left(e_z\right)_z - \pi R^2\left(e_z\right)_{z+\Delta z} - \pi R^2\Delta z\rho vg\sin\theta \quad \text{.....2.17}$$

Dividing $\pi R^2\Delta z$ and taking $\Delta z\rightarrow 0$ yield,

$$\frac{\partial}{\partial t}\left(\frac{1}{2}\rho v^2 + \rho\hat{U}\right) = \frac{2\left(e_r\right)_R}{R} - \frac{\partial\left(e_z\right)}{\partial z} - \rho vg\sin\theta \quad \text{.....2.18}$$

The detailed derivation of $(e_r)_{\mathrm{R}}$ and (e_z) can be found in Yoshioka's work (2007), and the energy balance equation becomes

$$\frac{\partial}{\partial t}\left(\rho\hat{U}\right) = \frac{2\gamma}{R}\rho_I\hat{H}_I v_I + \frac{2\left(1-\gamma\right)}{R}q_I - \frac{\partial}{\partial z}\left(\rho\hat{H}v\right) - \rho vg\sin\theta + E_{KE} + E_{VS} \quad \text{.....2.19}$$

The transient term can be expanded as

$$\frac{\partial}{\partial t}\left(\rho\hat{U}\right) = \rho\frac{\partial\hat{U}}{\partial t} + \hat{U}\frac{\partial\rho}{\partial t} \quad \text{.....2.20}$$

From the definition of enthalpy (Eq. **2.11**), Eq. **2.20** becomes

$$\frac{\partial}{\partial t}\left(\rho\hat{U}\right)=\rho\frac{\partial}{\partial t}\left(\hat{H}-\frac{p}{\rho}\right)+\left(\hat{H}-\frac{p}{\rho}\right)\frac{\partial\rho}{\partial t}$$
$$=\rho\frac{\partial\hat{H}}{\partial t}-\frac{\partial p}{\partial t}+\hat{H}\frac{\partial\rho}{\partial t} \quad \text{.....2.21}$$

Substituting Eq. **2**.**21** into Eq. **2**.**19** gives

$$\rho\frac{\partial\hat{H}}{\partial t}-\frac{\partial p}{\partial t}+\hat{H}\frac{\partial\rho}{\partial t}=\frac{2\gamma}{R}\rho_I\hat{H}_I v_I+\frac{2(1-\gamma)}{R}q_I-\frac{\partial}{\partial z}\left(\rho\hat{H}v\right) \quad \text{.....2.22}$$
$$-\rho vg\sin\theta+E_{KE}+E_{VS}$$

From mass balance equation (Eq. **2**.**6**), Eq. **2**.**22** can be written as

$$\rho\frac{\partial\hat{H}}{\partial t}-\frac{\partial p}{\partial t}+\hat{H}\left[-\frac{\partial}{\partial x}(\rho v)+\frac{2\gamma\rho_I v_I}{R}\right]$$
$$=\frac{2\gamma}{R}\rho_I\hat{H}_I v_I+\frac{2(1-\gamma)}{R}q_I-\frac{\partial}{\partial z}\left(\rho\hat{H}v\right)-\rho vg\sin\theta+E_{KE}+E_{VS} \quad \text{.....2.23}$$

Manipulation and simplification yield

$$\rho\frac{\partial\hat{H}}{\partial t}-\frac{\partial p}{\partial t}=\frac{2\gamma}{R}\rho_I v_I\left(\hat{H}_I-\hat{H}\right)+\frac{2(1-\gamma)}{R}q_I-\rho v\frac{\partial\hat{H}}{\partial z} \quad \text{.....2.24}$$
$$-\rho vg\sin\theta+E_{KE}+E_{VS}$$

To evaluate the enthalpy in Eq. **2**.**24**, we make use of the standard equilibrium thermodynamic formula,

$$d\hat{H}=\left(\frac{\partial\hat{H}}{\partial T}\right)_p dT+\left(\frac{\partial\hat{H}}{\partial p}\right)_T dp$$
$$=\hat{C}_p dT+\frac{1}{\rho}\left[1-\frac{1}{\hat{V}}\left(\frac{\partial\hat{V}}{\partial T}\right)_p T\right]dp \quad \text{.....2.25}$$
$$=\hat{C}_p dT+\frac{1}{\rho}(1-\beta T)dp$$

where $\hat{C}_p$ and β are heat capacity and thermal expansion coefficient respectively. The thermal expansion coefficient is defined as follows,

$$\beta=-\frac{1}{\rho}\left(\frac{\partial\rho}{\partial T}\right)_P=\frac{1}{V}\left(\frac{\partial V}{\partial T}\right)_p \quad \text{.....2.26}$$

Thus we have

$$\frac{\partial \hat{H}}{\partial t} = \hat{C}_p \frac{\partial T}{\partial t} + \frac{1}{\rho}(1-\beta T)\frac{\partial p}{\partial t} \quad \text{.....2.27}$$

$$\frac{\partial \hat{H}}{\partial z} = \hat{C}_p \frac{\partial T}{\partial z} + \frac{1}{\rho}(1-\beta T)\frac{\partial p}{\partial z} \quad \text{.....2.28}$$

Let the pressure at the boundary, p_I, be the same as the pressure of wellbore p, thus the enthalpy difference is calculated by

$$\begin{aligned} \hat{H}_I - \hat{H} &= \hat{C}_p(T_I - T) + \frac{1}{\rho}(1-\beta T)(p_I - p) \\ &= \hat{C}_p(T_I - T) \end{aligned} \quad \text{.....2.29}$$

Substitute Eqs. **2.27** to **2.29** into Eq.**2.24**, we obtain

$$\begin{aligned} \rho\hat{C}_p \frac{\partial T}{\partial t} - \beta T \frac{\partial p}{\partial t} = \frac{2\gamma}{R}\rho_I v_I \hat{C}_p(T_I - T) + \frac{2(1-\gamma)}{R} q_I - \rho v \hat{C}_p \frac{\partial T}{\partial z} \\ - v(1-\beta T)\frac{\partial p}{\partial z} - \rho v g \sin\theta + E_{KE} + E_{VS} \end{aligned} \quad \text{.....2.30}$$

Dividing by $\rho v \hat{C}_p$, Eq. **2.30** becomes

$$\begin{aligned} \frac{1}{v}\frac{\partial T}{\partial t} - \frac{\beta T}{\rho v \hat{C}_p}\frac{\partial p}{\partial t} = \frac{2\gamma}{R}\frac{\rho_I v_I}{\rho v}(T_I - T) + \frac{2(1-\gamma)}{R\rho v \hat{C}_p} q_I - \frac{\partial T}{\partial z} \\ - \frac{(1-\beta T)}{\rho \hat{C}_p}\frac{\partial p}{\partial z} - \frac{g\sin\theta}{\hat{C}_p} + \frac{(E_{KE} + E_{VS})}{\rho \hat{C}_p} \end{aligned} \quad \text{.....2.31}$$

Since Joule-Thomson coefficient is defined as

$$K_{JT} = \frac{\beta T - 1}{\rho \hat{C}_p} \quad \text{.....2.32}$$

The exchanging heat flux by conduction between wellbore fluid and formation can be expressed by

$$q_I = U_T\left(T_r\big|_{r=r_{wb}} - T\right) \quad \text{.....2.33}$$

where U_T denotes the overall heat transfer coefficient. Substituting Eq. **2.33** into Eq. **2.31** yields

$$\frac{1}{v}\frac{\partial T}{\partial t}-\frac{\beta T}{\rho v\hat{C}_p}\frac{\partial p}{\partial t}$$
$$=\frac{2\gamma}{R}\frac{\rho_I v_I}{\rho v}\left(T_I-T\right)+\frac{2(1-\gamma)}{R\rho v\hat{C}_p}U_T\left(T_r\big|_{r=r_w}-T\right)-\frac{\partial T}{\partial z}+K_{JT}\frac{\partial p}{\partial z} \quad \text{.....2.34}$$
$$-\frac{g\sin\theta}{\hat{C}_p}+\frac{\left(E_{KE}+E_{VS}\right)}{\rho\hat{C}_p}$$

where the kinetic and viscous term can be neglected, then Eq. **2.34** can be written as

$$\frac{1}{v}\frac{\partial T}{\partial t}-\frac{\beta T}{\rho v\hat{C}_p}\frac{\partial p}{\partial t}=\frac{2\gamma}{R}\frac{\rho_I v_I}{\rho v}\left(T_I-T\right)+\frac{2(1-\gamma)}{R\rho v\hat{C}_p}U_T\left(T_r\big|_{r=r_w}-T\right)-\frac{\partial T}{\partial z}$$
$$+K_{JT}\frac{\partial p}{\partial z}-\frac{g\sin\theta}{\hat{C}_p}=0 \quad \text{.....2.35}$$

which is the final form of the wellbore thermal model.

2.3 RESERVOIR FLOW MODEL

For a commingled multilayer reservoir without interlayer crossflow (**Fig. 2.3**), the reservoir layer flow rate and pressure distribution during a transient flow period can be determined by using the model developed by Ehlig-Economides (1987).

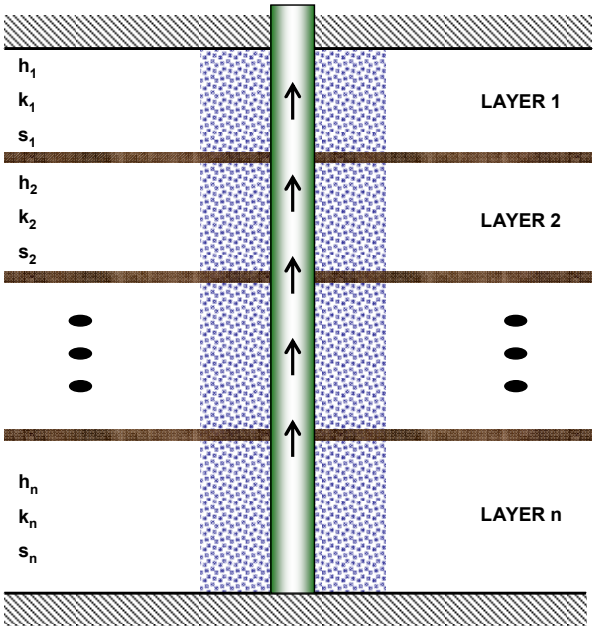

Fig. 2.3 Schematic plot of a commingled multilayer reservoir

To apply Ehlig-Economides model, each productive layer is assumed homogeneous and isotropic with a single flow phase of constant viscosity, small and constant compressibility. The permeability, porosity, and thickness of each layer can be different. Additionally, hydrostatic equilibrium is assumed for the initial reservoir condition with layer having the same initial reservoir potential.

2.3.1 Layer Pressure and Flow Rate Calculation

During the transient flow test, the layer flow rates and reservoir pressure distribution can be determined by solving the diffusivity equation in each productive layer. If the well has a no-flow outer boundary and a constant rate inner boundary condition, the *j*th layer diffusivity equation is given by

$$(kh)_j \nabla^2 p_j = (\phi h)_j c_t \mu \frac{\partial p_j}{\partial t} \quad \text{.....2.36}$$

where p_j denotes the formation pressure in the *j*th layer. The inner boundary at the well is given by the following two equations and it can take into account the skin factor s_j

and wellbore storage effects which is denoted by C,

$$p_{wf} = p_j(r_w,t) - s_j r_w \left.\frac{\partial p_j}{\partial r}\right|_{r_w} \quad \text{.....2.37}$$

and

$$-q = C\frac{dp_{wf}}{dt} - \frac{2\pi}{\mu}\sum_{j=1}^{n}\left[(kh)_j r_w \left.\frac{\partial p_j}{\partial r}\right|_{r_w}\right] \quad \text{.....2.38}$$

For the no-flow outer boundary, we have

$$\left.\frac{\partial p_j}{\partial r}\right|_{r_e} = 0 \quad \text{.....2.39}$$

The individual layer flow rate can be represented by

$$-q_j(t) = -\frac{2\pi(kh)_j}{\mu} r_w \left.\frac{\partial p_j}{\partial r}\right|_{r_w} \quad \text{.....2.40}$$

Finally, the initial condition is given by

$$p_j(r,0) = p_i \quad \text{.....2.41}$$

The solutions of the above equations are presented in Section 3.

2.3.2 Pressure Distribution within the Damage Region

In this research work, one of the advantages of the proposed testing and analysis approach is that the damage skin factor is possible to be evaluated by downhole temperature and pressure monitoring. Damage skin is used to describe the reduction in permeability to the near-wellbore region, and it is usually caused by the drilling and completion processes. Since the formation damage can significantly affect the well productivity, it will be helpful to know the damage skin factor.

In the solutions of the reservoir flow model, the damage skin takes effects as an extra pressure drop on the bottomhole flowing pressure. However, in this study we must consider the actual pressure variations within the damage region with the reduced formation permeability, because actual pressure variations within the damage region are

required for generating reservoir temperature distributions, which are used to reflect the damage skin in the testing and analysis method.

With the assumption of homogeneous formation properties in this work, given the damage radius, the pressure distribution within the damage region can be obtained by interpolating between original layer pressure distribution and bottomhole flowing pressure. In **Fig. 2.4**, we can see that the extra pressure drop due to the damage skin as $\Delta p(s)$. Since the dimensionless pressure drop p_{jD} is logarithmic linear with respect to the dimensionless radial distance r_D, the actual pressure drop within the damage radius r_{sD} could be obtained by doing interpolation using p_{wD} and $p_{jD}(r_{sD})$ The interpolated pressure distribution is shown in **Fig. 2.5** with the red dash line.

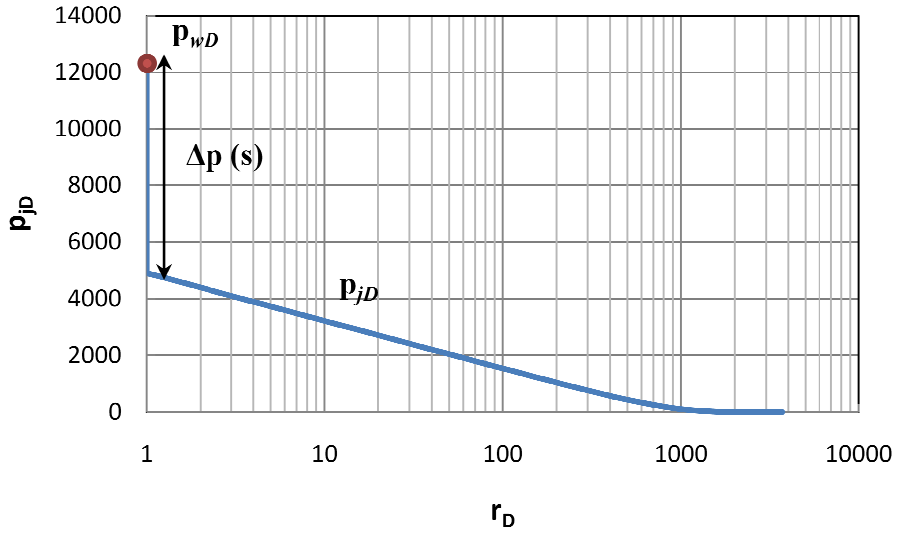

Fig. 2.4 Dimensionless layer pressure distribution without interpolation

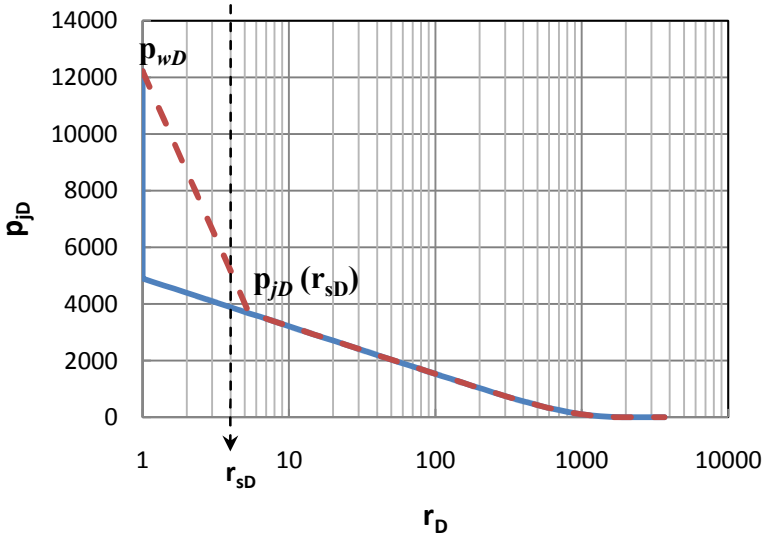

Fig. 2.5 Dimensionless layer pressure distribution after interpolation

2.4 RESERVOIR THERMAL MODEL

The reservoir thermal model has been developed to solve the reservoir temperature distribution during the transient flow test. The transient reservoir thermal model is derived from the general energy balance equation (Bird et al., 2002),

$$\frac{\partial}{\partial t}\rho\hat{U} = -\nabla\cdot\left(\rho\hat{U}\mathbf{v}\right) - p\nabla\cdot\mathbf{v} - \left(\boldsymbol{\tau}:\nabla\mathbf{v}\right) - \nabla\cdot\mathbf{q} \quad \text{.....2.42}$$

where the LHS of **Eq. 2.42** represents the accumulation rate of internal energy per unit volume; the first term in the RHS represents the net rate of internal energy addition per unit volume by convective transport; the second term in the RHS represents the reversible rate of internal energy increase per unit volume by compression; the third term in the RHS represents the irreversible rate of internal energy increase per unit volume by viscous dissipation, $-\left(\boldsymbol{\tau}:\nabla\mathbf{v}\right)$ is the viscous dissipation heating that describes the degradation of mechanical energy into thermal energy. The last term in the RHS represents the rate of internal energy addition per unit volume by heat conduction.

With Fourier's law, assuming the conductivity coefficient K_T is constant in formation, the conduction term can be calculated by

$$\mathbf{q} = -K_T \nabla^2 T \quad \text{.....2.43}$$

Considering the internal energy of both formation fluid and rock, we have the bulk internal energy term defined as

$$\rho\hat{U} = \phi\rho_f U_f + (1-\phi)\rho_r \hat{U}_r \quad \text{.....2.44}$$

where $\hat{U}$ denotes the internal energy per unit volume, the subscript "*f*" represents formation fluid, and "*r*" represents rock. For simplicity, the subscript "*f*" will be omitted in the following part of this paper.

For fluid flow in porous media, the term $-(\boldsymbol{\tau} : \nabla \mathbf{v})$ can be replaced by $-(\mathbf{v} \cdot \nabla p)$ (Al-Hadhrami et al., 2003). Substitute Eqs. 2.43 and 2.44 into Eq. 2.42, we have

$$\frac{\partial}{\partial t}\left[\phi\rho U + (1-\phi)\rho_r \hat{U}_r\right] = -\nabla \cdot \left(\rho\hat{U}\mathbf{v}\right) - p(\nabla \cdot \mathbf{v}) - \mathbf{v} \cdot \nabla p + K_T \nabla^2 T \quad \text{.....2.45}$$

From the definition of enthalpy,

$$\hat{H} = \hat{U} + p/\rho \quad \text{.....2.46}$$

the total derivative of enthalpy can be derived by using thermodynamic equilibrium relationships (Bird et al., 2002),

$$d\hat{H} = \hat{C}_p dT + \frac{1}{\rho}(1 - \beta T) dp \quad \text{.....2.47}$$

Substitution of Eq. **2.46** into Eq. **2.45** and manipulation yield

$$\frac{\partial}{\partial t}\left[\phi\rho\hat{H} - \phi p + (1-\phi)\rho_r \hat{U}_r\right] = -\nabla \cdot \left(\rho\hat{H}\mathbf{v}\right) + K_T \nabla^2 T \quad \text{.....2.48}$$

Assume the rock density is constant and the internal energy of rock can be approximated by heat capacity and temperature change, we have

$$d\hat{U}_r \cong d\hat{H}_r = \hat{C}_{pr} dT_r \quad \text{.....2.49}$$

Substitution of Eq. **2.49** into Eq. **2.48** and rearrangement result in

$$\begin{aligned} &\phi\rho\frac{\partial\hat{H}}{\partial t} + \hat{H}\frac{\partial(\rho\phi)}{\partial t} - \phi\frac{\partial p}{\partial t} + \rho_r \hat{C}_{pr}(1-\phi)\frac{\partial T_r}{\partial t} + T_r \frac{\partial}{\partial t}\left[\rho_r \hat{C}_{pr}(1-\phi)\right] \quad \text{.....2.50} \\ &= -\hat{H}\nabla \cdot \rho\mathbf{v} - \rho\mathbf{v} \cdot \nabla\hat{H} + K_T \nabla^2 T \end{aligned}$$

From the mass balance equation of formation fluid,

$$\frac{\partial}{\partial t}(\rho\phi) = -\nabla \cdot \rho\mathbf{v} \quad \text{.....2.51}$$

From the mass balance equation of formation rock,

$$\frac{\partial}{\partial t}[\rho_r(1-\phi)] = 0 \quad \text{.....2.52}$$

Eq. **2.50** can be rewritten as

$$\phi\rho\frac{\partial \hat{H}}{\partial t} - \phi\frac{\partial p}{\partial t} + \rho_r \hat{C}_{pr}(1-\phi)\frac{\partial T_r}{\partial t} = -\rho\mathbf{v}\cdot\nabla\hat{H} + K_T\nabla^2 T \quad \text{.....2.53}$$

Substitution of Eq. **2.47** into Eq. **2**.**53** and manipulation yield

$$\begin{aligned}&\phi\rho\hat{C}_p\frac{\partial T}{\partial t} - \phi\beta T\frac{\partial p}{\partial t} + \rho_r\hat{C}_{pr}(1-\phi)\frac{\partial T_r}{\partial t} \\ &= -\rho\mathbf{v}\cdot\hat{C}_p\nabla T + (\beta T - 1)\mathbf{v}\cdot\nabla p + K_T\nabla^2 T\end{aligned} \quad \text{.....2.54}$$

If we define the average property of formation fluid and rock,

$$\overline{\rho C_p} = \phi\rho C_p + (1-\phi)\rho_r C_{pr} \quad \text{.....2.55}$$

Suppose the heat transfer between formation fluid and rock grains is instantaneous, assuming that the thermal equilibrium between the formation fluid and rock can be reached instantly, we have $T = T_r$. Eq. **2.54** can be rewritten as

$$\overline{\rho\hat{C}_p}\frac{\partial T}{\partial t} - \phi\beta T\frac{\partial p}{\partial t} = -\rho\mathbf{v}\cdot\hat{C}_p\nabla T + (\beta T - 1)\mathbf{v}\cdot\nabla p + K_T\nabla^2 T \quad \text{.....2.56}$$

For radial-cylindrical coordinate system, assume there is no flow in z and θ direction, the energy balance becomes

$$\begin{aligned}&\overline{\rho\hat{C}_p}\frac{\partial T}{\partial t} - \phi\beta T\frac{\partial p}{\partial t} \\ &= -\rho\hat{C}_p v_r\frac{\partial T}{\partial r} + (\beta T - 1)v_r\frac{\partial p}{\partial r} + K_T\left[\frac{1}{r}\frac{\partial}{\partial r}\left(r\frac{\partial T}{\partial r}\right) + \frac{\partial^2 T}{\partial z^2}\right]\end{aligned} \quad \text{.....2.57}$$

From Darcy's law,

$$v_r = -\frac{k}{\mu}\frac{dp}{dr} \quad \text{.....2.58}$$

Substitution of Eq. **2.58** into Eq. **2.57** results in

$$\overline{\rho\hat{C}_p}\frac{\partial T}{\partial t}-\phi\beta T\frac{\partial p}{\partial t}$$
$$=-\frac{k\rho\hat{C}_p}{\mu}\frac{\partial p}{\partial r}\frac{\partial T}{\partial r}+\frac{k(\beta T-1)}{\mu}\left(\frac{\partial p}{\partial r}\right)^2+K_T\left[\frac{1}{r}\frac{\partial}{\partial r}\left(r\frac{\partial T}{\partial r}\right)+\frac{\partial^2 T}{\partial z^2}\right] \quad \text{.....2.59}$$

For the reservoir energy balance equation, the boundary and initial conditions can be given by Eq. **2.60** to Eq. **2.64**. The outer boundary condition is

$$T=T_{e1} \text{ at } r=r_e \quad \text{.....2.60}$$

where T_{e1} is the geothermal temperature at reservoir radial outer boundary. The inner boundary condition is given by

$$-K_T\left.\frac{dT}{dr}\right|_{r=r_{wb}}=U_T{}^*\left(T_f-T\big|_{r=r_{wb}}\right) \text{ at } r=r_{wb} \quad \text{.....2.61}$$

where $U_T{}^*$ is the overall heat transfer coefficient based on radius of $r=r_{wb}$ and $U_T{}^*=r_{ti}U_T/r_{wb}$. The upper boundary condition is

$$T=T_{e2} \text{ at } z=0 \quad \text{.....2.62}$$

where T_{e2} is the geothermal temperature at reservoir upper boundary. The bottom boundary condition is

$$T=T_{e3} \text{ at } z=D \quad \text{.....2.63}$$

where T_{e3} is the geothermal temperature at reservoir upper boundary. The initial boundary condition is

$$T=T_{ei} \text{ at } t=0 \quad \text{.....2.64}$$

where T_{ei} is the geothermal temperature at initial condition.

Here we assume the geothermal temperature boundary conditions for the outer, upper, and lower boundaries. At the inner boundary, radiation boundary condition is used to describe the heat exchange between the wellbore and the formation. The finite difference equations for reservoir thermal model are formulated in Section 3.

Now the transient formation energy balance equation is analyzed to show which phenomena are represented by each of the terms in Eq. **2.65**. The transient temperature

variation (term 1) is related to transient formation fluid expansion or compression (term 2), heat convection (term 3), fluid expansion or compression (term 4), viscous dissipation (term 5), and heat conduction (term 6).

$$\underbrace{\overline{\rho\hat{C}_p}\frac{\partial T}{\partial t}}_{\text{term 1}} \underbrace{-\phi\beta T\frac{\partial p}{\partial t}}_{\text{term 2}} = \underbrace{-\rho\mathbf{v}\hat{C}_p\cdot\nabla T}_{\text{term 3}} + \underbrace{\beta T\mathbf{v}\cdot\nabla p}_{\text{term 4}} \underbrace{-\mathbf{v}\cdot\nabla p}_{\text{term 5}} \underbrace{+K_T\nabla^2 T}_{\text{term 6}} \quad \text{.....2.65}$$

When the formation fluid flows towards wellbore from the outer reservoir boundary through porous media, all of the thermal phenomena take place simultaneously. The heat conduction is driven by the temperature difference; the heat convection happens due to the energy transferred by mass transport; the viscous dissipation heating happens due to the work done by viscous forces and it will result in fluid temperature increase; the fluid expansion or compression takes place because of the reservoir pressure variations and it will cause fluid temperature decrease or increase.

The combined viscous dissipation (term 6) and fluid expansion/compression (term 5) terms comprise the Joule-Thomson effect, which is the main reason for the fluid temperature changes in the formation. Heat conduction and convection affect the speed of temperature changes in the formation.

In this work, the skin factor represents the formation damage skin and is defined by the Hawkin equation (Hawkins, 1956),

$$s = \left(\frac{k}{k_s} - 1\right)\ln\frac{r_s}{r_w} \quad \text{.....2.66}$$

Layers with positive skin factors will have a greater pressure gradient within the damage zone. During the early-time transient flow period, the reservoir pressure variation within the damage zone would be larger than that in other producing intervals. Since the transient temperature variation depends on the reservoir pressure variation, the damage zone will lead to different layer transient temperature behavior depending on the layer skin. Sensitivity studies will illustrate this point.

3 FORWARD MODEL SOLUTION AND VALIDATION

The forward model has been formulated in Section 2. In this section, the solution procedure for each model component will be presented in detail. The wellbore model and reservoir thermal model are solved numerically using finite difference method, and the reservoir flow model is solved analytically using Laplace transform. The program chart of the forward model solution is presented to show how the wellbore and reservoir models are coupled together. Then some comparison cases are used for forward model validation. In the end, an illustrative example is presented to illustrate the forward model behavior.

3.1 FINITE DIFFERENCE EQUATIONS FOR WELLBORE MODEL

The wellbore flow and thermal models derived in section 2.2 are solved numerically by using finite difference method. The mesh cell configuration is depicted in **Fig. 3.1**.

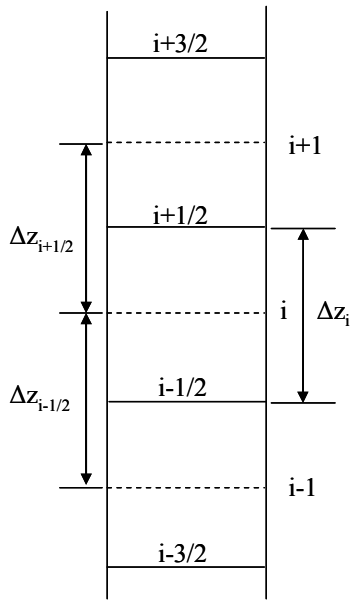

Fig. 3.1 Mesh cell configuration for wellbore model

The mass and energy balance equations are differenced over the mesh cells indicated by solid lines in **Fig. 3.1**; the momentum balance equation is differenced over the dashed mesh cells. This forms the staggered spatial difference scheme.

The finite difference equations for mass and momentum balance equations are straight forward. For mass balance equation, Eq. **2.6** becomes

$$\frac{\rho_{i+1/2}v_{i+1/2}-\rho_{i-1/2}v_{i-1/2}}{\Delta z_i}-\frac{2\gamma}{R}\left(\rho_I v_I\right)_i=0 \quad \text{.....3.1}$$

The velocity at node *i* can be calculated by

$$v_{i+1/2}=\frac{\rho_{i-1/2}v_{i-1/2}}{\rho_{i+1/2}}+\frac{\Delta z_i}{\rho_{i+1/2}}\frac{2\gamma}{R}\left(\rho_I v_I\right)_i \quad \text{.....3.2}$$

And for momentum balance equation, Eq. **2.8** becomes

$$\frac{p_{i+1}^{n+1}-p_i^{n+1}}{\Delta z_{i+1/2}}=-\frac{\left(\rho f v^2\right)_{i+1/2}^{n+1}}{R}-\frac{2\gamma}{R}\left(\rho_I v_I v\right)_{i+1/2}^{n+1}-\left(\rho v\right)_{i+1/2}^{n+1}\frac{v_{i+1}^{n+1}-v_i^{n+1}}{\Delta z_{i+1/2}}-\left(\rho g\sin\theta\right)_{i+1/2} \quad \text{.....3.3}$$

The pressure at node *i*+1 can be calculated by

$$p_{i+1}^{n+1}=p_i^{n+1}-\left(\rho\right)_{i+1/2}^{n}\Delta z_{i+1/2}\left[\frac{\left(\rho f v^2\right)_{i+1/2}^{n+1}}{R}+\frac{2\gamma}{R}\left(\rho_I v_I v\right)_{i+1/2}^{n+1}+\left(\rho v\right)_{i+1/2}^{n+1}\frac{v_{i+1}^{n+1}-v_i^{n+1}}{\Delta z_{i+1/2}}+\left(\rho g\sin\theta\right)_{i+1/2}\right] \quad \text{.....3.4}$$

For each term in the energy balance equation (Eq. **2.35**), the discretized energy balance equation is given by

$$\begin{aligned}&\left(\rho\hat{C}_p\right)_i^n\frac{T_i^{n+1}-T_i^n}{\Delta t}-\beta_i^n T_i^{n+1}\frac{p_i^{n+1}-p_i^n}{\Delta t}-\frac{2\gamma}{R}\left(\rho_I v_I\right)_i^{n+1}\left(\hat{C}_p\right)_i^n\left(T_I-T\right)_i^{n+1}\\&-\frac{2(1-\gamma)}{R}U_T\left(T_I-T\right)_i^{n+1}+\left(\rho\hat{C}_p\right)_i^n v_i^{n+1}\frac{T_{i+1/2}^{n+1}-T_{i-1/2}^{n+1}}{\Delta z_i}\\&-\left(\beta_i^n T_i^{n+1}-1\right)v_i^{n+1}\frac{p_{i+1/2}^{n+1}-p_{i-1/2}^{n+1}}{\Delta z_i}+\rho_i^n v_i^{n+1}\left(g\sin\theta\right)_i=0\end{aligned} \quad \text{.....3.5}$$

Rearrangement yields

$$\frac{\left(\rho\hat{C}_p\right)_i^n v_i^{n+1}}{\Delta z_i} T_{i+1/2}^{n+1} + \left[\frac{\left(\rho\hat{C}_p\right)_i^n}{\Delta t} + \frac{2\gamma}{R}\left(\rho_I v_I\right)_i^{n+1}\left(\hat{C}_p\right)_i^n + \frac{2(1-\gamma)}{R}U_T\right] - \frac{\left(\rho\hat{C}_p\right)_i^n v_i^{n+1}}{\Delta z_i} T_{i-1/2}^{n+1}$$

$$= \frac{\left(\rho\hat{C}_p\right)_i^n}{\Delta t} T_i^n + \beta_i^n T_i^{n+1}\frac{p_i^{n+1}-p_i^n}{\Delta t} + \left[\frac{2\gamma}{R}\left(\rho_I v_I\right)_i^{n+1}\left(\hat{C}_p\right)_i^n + \frac{2(1-\gamma)}{R}U_T\right] T_{I,i}^{n+1}$$

$$+ \left(\beta_i^n T_i^{n+1} - 1\right) v_i^{n+1}\frac{p_{i+1/2}^{n+1} - p_{i-1/2}^{n+1}}{\Delta z_i} - \rho_i^n v_i^{n+1}\left(g\sin\theta\right)_i$$

.....3.6

and the temperature at node *i* can be solved by

$$T_i^{n+1} = \left[\frac{\left(\rho\hat{C}_p\right)_i^n}{\Delta t} + \frac{2\gamma}{R}\left(\rho_I v_I\right)_i^{n+1}\left(\hat{C}_p\right)_i^n + \frac{2(1-\gamma)}{R}U_T + \frac{\left(\rho\hat{C}_p\right)_i^n v_{i-1/2}^{n+1}}{\Delta z_i}\right.$$

$$\left. - \beta_i^n\frac{p_i^{n+1}-p_i^n}{\Delta t} - \beta_i^n v_{i-1/2}^{n+1}\frac{p_i^{n+1}-p_{i-1}^{n+1}}{\Delta z_i}\right]^{-1} \cdot \left\{\frac{\left(\rho\hat{C}_p\right)_i^n v_{i-1/2}^{n+1}}{\Delta z_i} T_{i-1}^{n+1}\right. \quad \text{.....3.7}$$

$$+ \frac{\left(\rho\hat{C}_p\right)_i^n}{\Delta t} T_i^n + \left[\frac{2\gamma}{R}\left(\rho_I v_I\right)_i^{n+1}\left(\hat{C}_p\right)_i^n + \frac{2(1-\gamma)}{R}U_T\right] T_{I,i}^{n+1}$$

$$\left. - v_{i-1/2}^{n+1}\frac{p_i^{n+1}-p_{i-1}^{n+1}}{\Delta z_i} - \rho_i^n v_{i-1/2}^{n+1}\left(g\sin\theta\right)_i\right\}$$

Since the differenced equations do not form a complete set of equations for the variables at all node positions, they must be supplemented by additional relationships, which produce a "weighted donor cell" difference scheme that is particularly stable. Assuming the wellbore fluid flow is positive upward, we can define the weighting parameter

$$\beta_{i-1/2} = \frac{v_{i-1/2}}{\left|v_{i-1/2}\right|} \quad \text{.....3.8}$$

and the density at grid boundaries are given by

$$\rho_{i-1/2}^{n+1} = \left(\frac{1+\beta_{i-1/2}}{2}\right)\rho_{i-1}^{n+1} + \left(\frac{1-\beta_{i-1/2}}{2}\right)\rho_i^{n+1} = \rho_{i-1}^{n+1} \quad \text{.....3.9}$$

$$\rho_{i+1/2}^{n+1} = \left(\frac{1+\beta_{i+1/2}}{2}\right)\rho_i^{n+1} + \left(\frac{1-\beta_{i+1/2}}{2}\right)\rho_{i+1}^{n+1} = \rho_i^{n+1} \quad \text{.....3.10}$$

$$v_i^{n+1} = \left(\frac{1+\beta_i}{2}\right)v_{i-1/2}^{n+1} + \left(\frac{1-\beta_i}{2}\right)v_{i+1/2}^{n+1} = v_{i-1/2}^{n+1} \quad \text{.....3.11}$$

$$v_{i+1}^{n+1} = \left(\frac{1+\beta_i}{2}\right)v_{i+1/2}^{n+1} + \left(\frac{1-\beta_i}{2}\right)v_{i+3/2}^{n+1} = v_{i+1/2}^{n+1} \quad \text{.....3.12}$$

$$T_{i-1/2}^{n+1} = \left(\frac{1+\beta_{i-1/2}}{2}\right)T_{i-1}^{n+1} + \left(\frac{1-\beta_{i-1/2}}{2}\right)T_i^{n+1} = T_{i-1}^{n+1} \quad \text{.....3.13}$$

$$T_{i+1/2}^{n+1} = \left(\frac{1+\beta_{i+1/2}}{2}\right)T_i^{n+1} + \left(\frac{1-\beta_{i+1/2}}{2}\right)T_{i+1}^{n+1} = T_i^{n+1} \quad \text{.....3.14}$$

$$p_{i-1/2}^{n+1} = \left(\frac{1+\beta_{i-1/2}}{2}\right)p_{i-1}^{n+1} + \left(\frac{1-\beta_{i-1/2}}{2}\right)p_i^{n+1} = p_{i-1}^{n+1} \quad \text{.....3.15}$$

$$p_{i+1/2}^{n+1} = \left(\frac{1+\beta_{i+1/2}}{2}\right)p_i^{n+1} + \left(\frac{1-\beta_{i+1/2}}{2}\right)p_{i+1}^{n+1} = p_i^{n+1} \quad \text{.....3.16}$$

After discretizing the wellbore into nonuniform small control volumes, we obtain the wellbore numerical model. Since the wellbore numerical model equations are nonlinear, it is difficult to solve the whole system simultaneously. In this research work, the wellbore model is solved iteratively with the following boundary and initial conditions.

1) For mass balance equation (Eq. **3.2**),

$$v_0 = 0 \quad \text{at } i = 0 \quad \text{.....3.17}$$

and the initial condition is

$$v_i = 0 \quad \text{for } 0 \le i \le NZ \quad \text{.....3.18}$$

2) For momentum balance equation (Eq. **3.4**),

$$p_0 = p_{r_0} \quad \text{at } i = 0 \quad \text{.....3.19}$$

where $\boldsymbol{p_{r_0}}$ is the reservoir pressure at $i = 0$. The initial condition is

$$p_i = p_{r_i} \quad \text{for } 0 \le i \le NZ \quad \text{.....3.20}$$

where $\boldsymbol{p_{r_i}}$ is the initial reservoir pressure.

3) For energy balance equation (Eq. **3.7**)

$$T_0 = T_{G_0} \text{ at } i = 0 \quad \text{.....3.21}$$

where $\boldsymbol{T_{G_0}}$ is the geothermal temperature at $i = 0$. The initial condition is

$$T_i = T_{G_i} \text{ for } 0 \le i \le NZ \quad \text{.....3.22}$$

where $\boldsymbol{T_{G_i}}$ is the geothermal temperature.

At each time step, first wellbore temperature and pressure profiles are assumed (usually the temperature and pressure profile from the previous time step is used). Then the wellbore fluid velocity is solved from mass balance equation. In this procedure, the sandface flow rate is provided by reservoir flow model. After obtaining the velocity profile, the pressure profile along the wellbore is then calculated by solving the momentum balance equation. Then the fluid properties are updated using new velocity and pressure. The comparison is made between the assumed pressure profile and the calculated pressure profile. If the differences are not within tolerance, we let the pressure profile be the new calculated values and do the calculation again. After pressure iteration converges, the temperature profile along the wellbore is calculated by solving the energy balance equation. Then the comparison is made between the assumed temperature profile and the calculated temperature profile. Once the discrepancy is within the tolerance, the temperature profile is believed to be converged and we can start a new time step. Actually, since the wellbore model and reservoir model are constrained each other, another iterative loop is need when we solve the whole system, which will be addressed in Section 3.4.

3.2 ANALYTICAL SOLUTIONS OF RESERVOIR FLOW MODEL

To solve the diffusivity equations in individual layers (Eq. **2.36**), the following dimensionless variables are defined,

$$p_{jD} = \frac{2\pi\overline{kh}}{q\mu}\left(p_i - p_j\right) \quad \text{.....3.23}$$

$$t_D = \frac{\overline{kh}t}{\overline{\phi h}\mu c_t r_w^2} \quad \text{.....3.24}$$

$$r_D = r/r_w \quad \text{.....3.25}$$

$$r_{eD} = r_e/r_w \quad \text{.....3.26}$$

$$C_D = \frac{C}{2\pi\overline{\phi h}c_t r_w^2} \quad \text{.....3.27}$$

$$\overline{kh} = \sum_{j=1}^{n}(kh)_j \quad \text{.....3.28}$$

$$\overline{\phi h} = \sum_{j=1}^{n}(\phi h)_j \quad \text{.....3.29}$$

$$\kappa_j = (kh)_j / \overline{kh} \quad \text{.....3.30}$$

$$\omega_j = (\phi h)_j / \overline{\phi h} \quad \text{.....3.31}$$

and

$$\sigma_j = \sqrt{\frac{\omega_j}{\kappa_j}}\ell \quad \text{.....3.32}$$

Substitution of Eqs. **3.23** through **3.27** into Eqs. **2.36** to **2.41** results in

$$\kappa_j \nabla^2 p_{jD} = \omega_j \frac{\partial p_{jD}}{\partial t_D} \quad \text{.....3.33}$$

with the dimensionless boundary and initial conditions, the wellbore boundary condition becomes

$$p_{wD} = p_{jD}(1, t_D) - s_j \left.\frac{\partial p_{jD}}{\partial r_D}\right|_{r_D=1} \quad \text{.....3.34}$$

and

$$1 = C_D \frac{dp_{wD}}{dt_D} - \sum_{j=1}^{n} \kappa_j \left.\frac{\partial p_{jD}}{\partial r_D}\right|_{r_D=1} \quad \text{.....3.35}$$

The no-flow outer boundary condition becomes

$$\left.\frac{\partial p_{jD}}{\partial r_D}\right|_{r_{eD}} = 0 \quad \text{.....3.36}$$

The individual layer flow rate equation becomes

$$q_{jD}(t_D) = \frac{q_j}{q} = -\kappa_j \left.\frac{\partial p_{jD}}{\partial r_D}\right|_{r_D=1} \quad \text{.....3.37}$$

and for initial condition, we have

$$p_{jD}(r_D, 0) = 0 \quad \text{.....3.38}$$

The dimensionless equations (Eq. **3.33**) can be solved using Laplace transform. First we define ℓ as the Laplace space variable, the dimensionless diffusivity equation and boundary conditions can be transformed to Laplace space as follows,

$$\kappa_j \nabla^2 \overline{p}_{jD} = \omega_j \ell \overline{p}_{jD} \quad \text{.....3.39}$$

with

$$\text{B.C. 1} \quad \overline{p}_{wD} = \overline{p}_{jD}(1, \ell) - s_j \left.\frac{\partial \overline{p}_{jD}}{\partial r_D}\right|_{r_D=1} \quad \text{.....3.40}$$

$$\text{B.C. 2} \quad \frac{1}{\ell} = C_D \overline{p}_{wD} \ell - \sum_{j=1}^{n} \kappa_j \left.\frac{\partial \overline{p}_{jD}}{\partial r_D}\right|_{r_D=1} \quad \text{.....3.41}$$

$$\text{B.C. 3} \quad \left.\frac{\partial \overline{p}_{jD}}{\partial r_D}\right|_{r_{eD}} = 0 \quad \text{.....3.42}$$

The general solution of Eq. **3.39** is

$$\overline{p}_{jD} = A_j K_0\left(r_D \sqrt{\frac{\omega_j}{\kappa_j}\ell}\right) + B_j I_0\left(r_D \sqrt{\frac{\omega_j}{\kappa_j}\ell}\right) = A_j K_0(r_D \sigma_j) + B_j I_0(r_D \sigma_j) \quad \text{.....3.43}$$

where A_j and B_j are constants to be determined from Eqs. **3**.**40** to **3**.**42**. Substitution of the general solution (Eq. **3**.**43**) into Eqs. **3**.**40** to **3**.**42** yields,

$$\overline{p}_{wD}(z) = A_j K_0(\sigma_j) + B_j I_0(\sigma_j) - s_j\left[-\sigma_j A_j K_1(\sigma_j) + \sigma_j B_j I_1(\sigma_j)\right] \quad \text{.....3.44}$$

$$\sum_{j=1}^{n} \kappa_j \sigma_j \left[A_j K_1(\sigma_j) - B_j I_1(\sigma_j)\right] = \frac{1}{\ell}\left(1 - C_D \overline{p}_{wD} \ell^2\right) \quad \text{..... 3.45}$$

$$-\sigma_j A_j K_1(\sigma_j r_{eD}) + \sigma_j B_j I_1(\sigma_j r_{eD}) = 0 \quad \text{.....3.46}$$

The outer boundary condition (Eq. **3**.**46**) yields

$$B_j = A_j \frac{K_1(\sigma_j r_{eD})}{I_1(\sigma_j r_{eD})} \quad \text{.....3.47}$$

If we denote $b_j = \frac{K_1(\sigma_j r_{eD})}{I_1(\sigma_j r_{eD})}$, then we have $B_j = b_j A_j$. For the (*j-1*) th layer and the *j*th layer, the inner boundary condition (Eq. **3**.**44**) becomes

$$\begin{aligned} &A_{j-1}K_0(\sigma_{j-1}) + B_{j-1}I_0(\sigma_{j-1}) + s_{j-1}\sigma_{j-1}\left[A_{j-1}K_1(\sigma_{j-1}) - B_{j-1}I_1(\sigma_{j-1})\right] \\ &\quad - A_j K_0(\sigma_j) - B_j I_0(\sigma_j) - s_j\sigma_j\left[A_j K_1(\sigma_j) - B_j I_1(\sigma_j)\right] = 0 \end{aligned} \quad \text{..... 3.48}$$

or written as

$$\begin{aligned} &A_{j-1}\left\{K_0(\sigma_{j-1}) + b_{j-1}I_0(\sigma_{j-1}) + s_{j-1}\sigma_{j-1}\left[K_1(\sigma_{j-1}) - b_{j-1}I_1(\sigma_{j-1})\right]\right\} \\ &\quad + A_j\left\{-K_0(\sigma_j) - b_j I_0(\sigma_j) - s_j\sigma_j\left[K_1(\sigma_j) - b_j I_1(\sigma_j)\right]\right\} = 0 \end{aligned} \quad \text{.....3.49}$$

From Eq. **3**.**41**, we have

$$\sum_{j=1}^{n} \kappa_j \sigma_j \left[A_j K_1(\sigma_j) - b_j A_j I_1(\sigma_j)\right] = \frac{1}{\ell}\left(1 - C_D \overline{p}_{wD} \ell^2\right) \quad \text{.....3.50}$$

The *n* equations Eq. **3.49** and **3.50** are linear equations in the A_j coefficients. The matrix format is given by Eq. **3.51**, and the coefficients A_j can be determined by Eq. **3**.**52**,

$$\begin{pmatrix} K_0(\sigma_1)+b_1 I_0(\sigma_1)+ & -K_0(\sigma_2)-b_2 I_0(\sigma_2)- & & & \\ s_1\sigma_1[K_1(\sigma_1)-b_1 I_1(\sigma_1)] & s_2\sigma_2[K_1(\sigma_2)-b_2 I_1(\sigma_2)] & \cdots & \cdots & 0 \\ 0 & K_0(\sigma_2)+b_2 I_0(\sigma_2)+ & \cdots & \cdots & 0 \\ & s_2\sigma_2[K_1(\sigma_2)-b_2 I_1(\sigma_2)] & \cdots & & \\ \cdots & \cdots & \cdots & \cdots & \cdots \\ 0 & 0 & \cdots & K_0(\sigma_{n-1})+b_{n-1} I_0(\sigma_{n-1})+ & -K_0(\sigma_n)-b_n I_0(\sigma_n)- \\ & & & s_{n-1}\sigma_{n-1}[K_1(\sigma_{n-1})-b_{n-1} I_1(\sigma_{n-1})] & s_n\sigma_n[K_1(\sigma_n)-b_n I_1(\sigma_n)] \\ \kappa_1\sigma_1[K_1(\sigma_1)-b_1 I_1(\sigma_1)] & \kappa_2\sigma_2[K_1(\sigma_2)-b_2 I_1(\sigma_2)] & \cdots & \cdots & \kappa_n\sigma_n[K_1(\sigma_n)-b_n I_1(\sigma_n)] \end{pmatrix} \begin{pmatrix} A_1 \\ A_2 \\ A_3 \\ \cdots \\ A_{n-1} \\ A_n \end{pmatrix} = \begin{pmatrix} 0 \\ 0 \\ 0 \\ \cdots \\ 0 \\ 1/\ell \end{pmatrix}$$

.....3.51

$$\begin{pmatrix} A_1 \\ A_2 \\ A_3 \\ \cdots \\ A_{n-1} \\ A_n \end{pmatrix} = \begin{pmatrix} K_0(\sigma_1)+b_1 I_0(\sigma_1)+ & -K_0(\sigma_2)-b_2 I_0(\sigma_2)- & & & \\ s_1\sigma_1[K_1(\sigma_1)-b_1 I_1(\sigma_1)] & s_2\sigma_2[K_1(\sigma_2)-b_2 I_1(\sigma_2)] & \cdots & \cdots & 0 \\ 0 & K_0(\sigma_2)+b_2 I_0(\sigma_2)+ & \cdots & \cdots & 0 \\ & s_2\sigma_2[K_1(\sigma_2)-b_2 I_1(\sigma_2)] & \cdots & & \\ \cdots & \cdots & \cdots & \cdots & \cdots \\ 0 & 0 & \cdots & K_0(\sigma_{n-1})+b_{n-1} I_0(\sigma_{n-1})+ & -K_0(\sigma_n)-b_n I_0(\sigma_n)- \\ & & & s_{n-1}\sigma_{n-1}[K_1(\sigma_{n-1})-b_{n-1} I_1(\sigma_{n-1})] & s_n\sigma_n[K_1(\sigma_n)-b_n I_1(\sigma_n)] \\ \kappa_1\sigma_1[K_1(\sigma_1)-b_1 I_1(\sigma_1)] & \kappa_2\sigma_2[K_1(\sigma_2)-b_2 I_1(\sigma_2)] & \cdots & \cdots & \kappa_n\sigma_n[K_1(\sigma_n)-b_n I_1(\sigma_n)] \end{pmatrix}^{-1} \begin{pmatrix} 0 \\ 0 \\ 0 \\ \cdots \\ 0 \\ 1/\ell \end{pmatrix}$$

.....3.52

The wellbore pressure without storage is given by

$$\bar{p}_{wD_{C_D=0}} = A_j \left\{ K_0(\sigma_j) + b_j I_0(\sigma_j) + s_j \sigma_j \left[K_1(\sigma_j) - b_j I_1(\sigma_j) \right] \right\} \quad \text{.....3.53}$$

and the solution with storage is given by

$$\bar{p}_{wD} = \frac{1}{\dfrac{1}{\bar{p}_{wD_{C_D=0}}} + C_D \ell^2} \quad \text{.....3.54}$$

The flow rates are given by

$$\begin{aligned} \bar{q}_{jD} &= \left(1 - C_D \bar{p}_{wD} \ell^2\right) \bar{q}_{jD_{C_D=0}} \\ &= \left(1 - C_D \bar{p}_{wD} \ell^2\right) \kappa_j \sigma_j A_j \left[K_1(\sigma_j) - b_j I_1(\sigma_j) \right] \end{aligned} \quad \text{.....3.55}$$

and the radial pressure distribution for each layer is given by

$$\begin{aligned} \bar{p}_{jD} &= \left(1 - C_D \bar{p}_{wD} \ell^2\right) \bar{p}_{jD_{C_D=0}} \\ &= \left(1 - C_D \bar{p}_{wD} \ell^2\right) A_j \left[K_0(\sigma_j r_D) + b_j I_0(\sigma_j r_D) \right] \end{aligned} \quad \text{.....3.56}$$

The analytical solutions of layer flow rates and reservoir pressure in real space can be obtained from numerical inversion of Laplace transform using Stehfest's algorithm (Stehfest, 1970).

In addition, for a constant-pressure outer boundary, the relationship between A_j and B_j becomes

$$B_j = -A_j \frac{K_0(\sigma_j r_{eD})}{I_0(\sigma_j r_{eD})} \quad \text{.....3.57}$$

and the final solutions are the same as the no-flow boundary condition.

3.3 FINITE DIFFERENCE EQUATIONS FOR RESERVOIR THERMAL MODEL

The reservoir thermal model can be solved numerically by using finite-difference method. To improve the calculation efficiency and accuracy, logarithmic grid blocks in the radial direction and nonuniform grid blocks in the vertical direction is used like **Fig. 3.2** shows. Here we assume there are *NR* grid blocks in radial direction and *NZ* grid blocks in *z* direction.

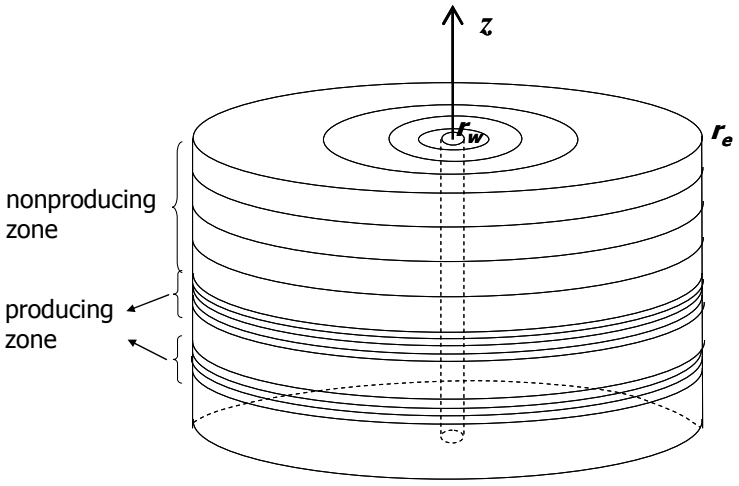

Fig. 3.2 Schematic plot of the discretized commingled multilayer reservoir

First, we transfer radial logarithmic grids into uniform grid by defining x grid system as follows,

$$x = \log_{a_{\lg}}\left(r/r_w\right),\ x = i\Delta x,\ \Delta x = 1 \quad \text{.....3.58}$$

The coefficient $a_{\lg}$ is defined as

$$a_{\lg} = \left(\frac{r_e}{r_w}\right)^{\frac{1}{NR-1}} \quad \text{.....3.59}$$

where NR represents the number of the grid block in the radial direction. Thereby any radial distance can be described as

$$r_i = r_w a_{\lg}^{i\Delta x} = r_w a_{\lg}^{i} \quad \text{.....3.60}$$

The partial derivatives of temperature and pressure with respect to time and space variable are given by

$$\frac{\partial T}{\partial r} = \frac{\partial T}{\partial x}\cdot\frac{dx}{dr} = \frac{\partial T}{\partial x}\cdot\frac{1}{r\ln a_{\lg}} \quad \text{.....3.61}$$

$$\frac{1}{r}\frac{\partial}{\partial r}\left(r\frac{\partial T}{\partial r}\right) = \left(\frac{1}{\ln a_{\lg}}\right)^2\frac{1}{r^2}\frac{\partial^2 T}{\partial x^2} \quad \text{.....3.62}$$

$$\frac{\partial p}{\partial r}=\frac{\partial p}{\partial x}\cdot\frac{dx}{dr}=\frac{\partial p}{\partial x}\cdot\frac{1}{r\ln a_{\lg}} \quad \text{.....3.63}$$

Substitution of Eqs. **3.61** through **3.63** into Eq. **2.59** results in

$$\begin{aligned}&\overline{\rho\hat{C}_p}r^2\frac{\partial T}{\partial t}-\phi\beta Tr^2\frac{\partial p}{\partial t}\\&=\frac{K_T}{\left(\ln a_{\lg}\right)^2}\frac{\partial^2 T}{\partial x^2}-\frac{k\rho\hat{C}_p}{\mu\left(\ln a_{\lg}\right)^2}\frac{\partial p}{\partial x}\frac{\partial T}{\partial x}+K_T r^2\frac{\partial^2 T}{\partial z^2}+\frac{k\left(\beta T-1\right)}{\mu\left(\ln a_{\lg}\right)^2}\left(\frac{\partial p}{\partial x}\right)^2\end{aligned} \quad \text{.....3.64}$$

The first derivative is approximated by forward differences and the second derivative is approximated by central differences. Therefore, the discretized reservoir energy balance equation is given by

$$\begin{aligned}&-\frac{\overline{\rho\hat{C}_p}r_w^2a_{\lg}^{2i}}{\Delta t}T_{i,j}^n+\frac{k}{4\mu\left(\ln a_{\lg}\right)^2}\left(p_{i+1,j}^{n+1}-p_{i-1,j}^{n+1}\right)^2\\&=T_{i,j-1}^{n+1}\left[\frac{K_T r_w^2a_{\lg}^{2i}}{\Delta z_{i,j-1}\cdot\frac{\left(\Delta z_{i,j-1}+\Delta z_{i,j}\right)}{2}}\right]+T_{i-1,j}^{n+1}\left[\frac{K_T}{\left(\ln a_{\lg}\right)^2}+\frac{k\rho\hat{C}_p}{4\mu\left(\ln a_{\lg}\right)^2}\left(p_{i+1,j}^{n+1}-p_{i-1,j}^{n+1}\right)\right]\\&+T_{i,j}^{n+1}\left[-\frac{2K_T}{\left(\ln a_{\lg}\right)^2}-\frac{K_T r_w^2a_{\lg}^{2i}}{\Delta z_{i,j-1}\cdot\frac{\left(\Delta z_{i,j-1}+\Delta z_{i,j}\right)}{2}}-\frac{K_T r_w^2a_{\lg}^{2i}}{\Delta z_{i,j}\cdot\frac{\left(\Delta z_{i,j-1}+\Delta z_{i,j}\right)}{2}}\right.\\&\left.+\frac{k\beta\left(p_{i+1,j}^{n+1}-p_{i-1,j}^{n+1}\right)^2}{4\mu\left(\ln a_{\lg}\right)^2}-\frac{\overline{\rho\hat{C}_p}r_w^2a_{\lg}^{2i}}{\Delta t}+\frac{\phi\beta r_w^2a_{\lg}^{2i}}{\Delta t}\left(p_{i,j}^{n+1}-p_{i,j}^{n}\right)\right]\\&+T_{i+1,j}^{n+1}\left[\frac{K_T}{\left(\ln a_{\lg}\right)^2}-\frac{k\rho\hat{C}_p}{4\mu\left(\ln a_{\lg}\right)^2}\left(p_{i+1,j}^{n+1}-p_{i-1,j}^{n+1}\right)\right]+T_{i,j+1}^{n+1}\left[\frac{K_T r_w^2a_{\lg}^{2i}}{\Delta z_{i,j}\cdot\frac{\left(\Delta z_{i,j-1}+\Delta z_{i,j}\right)}{2}}\right]\end{aligned} \quad \text{.....3.65}$$

or rewritten as

$$a_S T_{i,j-1}^{n+1}+a_W T_{i-1,j}^{n+1}+a_C T_{i,j}^{n+1}+a_E T_{i+1,j}^{n+1}+a_N T_{i,j+1}^{n+1}=a_F \quad \text{.....3.66}$$

where the coefficients are given by

$$a_S = \frac{K_T r_w^2 a_{\lg}^{2i}}{\Delta z_{i,j-1} \cdot \frac{\left(\Delta z_{i,j-1} + \Delta z_{i,j}\right)}{2}} \quad \text{.....3.67}$$

$$a_W = \frac{K_T}{\left(\ln a_{\lg}\right)^2} + \frac{k\rho\hat{C}_p}{4\mu\left(\ln a_{\lg}\right)^2}\left(p_{i+1,j}^{n+1} - p_{i-1,j}^{n+1}\right) \quad \text{.....3.68}$$

$$a_C = -\frac{2K_T}{\left(\ln a_{\lg}\right)^2} - \frac{K_T r_w^2 a_{\lg}^{2i}}{\Delta z_{i,j-1} \cdot \frac{\left(\Delta z_{i,j-1} + \Delta z_{i,j}\right)}{2}} - \frac{K_T r_w^2 a_{\lg}^{2i}}{\Delta z_{i,j} \cdot \frac{\left(\Delta z_{i,j-1} + \Delta z_{i,j}\right)}{2}} \quad \text{.....3.69}$$

$$+ \frac{k\beta\left(p_{i+1,j}^{n+1} - p_{i-1,j}^{n+1}\right)^2}{4\mu\left(\ln a_{\lg}\right)^2} - \frac{\overline{\rho\hat{C}_p} r_w^2 a_{\lg}^{2i}}{\Delta t} + \frac{\phi\beta r_w^2 a_{\lg}^{2i}}{\Delta t}\left(p_{i,j}^{n+1} - p_{i,j}^{n}\right)$$

$$a_E = \frac{K_T}{\left(\ln a_{\lg}\right)^2} - \frac{k\rho\hat{C}_p}{4\mu\left(\ln a_{\lg}\right)^2}\left(p_{i+1,j}^{n+1} - p_{i-1,j}^{n+1}\right) \quad \text{.....3.70}$$

$$a_N = \frac{K_T r_w^2 a_{\lg}^{2i}}{\Delta z_{i,j} \cdot \frac{\left(\Delta z_{i,j-1} + \Delta z_{i,j}\right)}{2}} \quad \text{.....3.71}$$

$$a_F = -\frac{\overline{\rho\hat{C}_p} r_w^2 a_{\lg}^{2i}}{\Delta t} T_{i,j}^{n} + \frac{k}{4\mu\left(\ln a_{\lg}\right)^2}\left(p_{i+1,j}^{n+1} - p_{i-1,j}^{n+1}\right)^2 \quad \text{.....3.72}$$

The initial and boundary conditions can be discretized as follows.

$$T_{NR,j}^{n+1} = T_e \quad \text{at} \quad i = NR \quad \text{.....3.73}$$

$$T_{0,j}^{n+1} = \frac{2K_T - U_T^{\,*} r_w a_{\lg}^{0.5} \ln a_{\lg}}{2K_T + U_T^{\,*} r_w a_{\lg}^{0.5} \ln a_{\lg}} T_{1,j}^{n+1} + \frac{2U_T^{\,*} T_f^{n+1} \cdot r_w a_{\lg}^{0.5} \ln a_{\lg}}{2K_T + U_T^{\,*} r_w a_{\lg}^{0.5} \ln a_{\lg}} \quad \text{at} \quad i = 0 \quad \text{.....3.74}$$

$$T_{i,NZ}^{n+1} = T_e \quad \text{at} \quad j = NZ \quad \text{.....3.75}$$

$$T_{i,0}^{n+1} = T_e \quad \text{at} \quad j = 0 \quad \text{.....3.76}$$

$$T_{i,j}^{0} = T_e \quad \text{at} \quad t = 0 \quad \text{.....3.77}$$

Additionally, the timestep size selection for simulation is similar to grid spacing. Here logarithmic timestep spacing is used for a greater accuracy because temperature changes tend to be linear with the logarithm of time. Assume there are *NT* time steps in total, and the constant coefficient is given by

$$a_{\lg t} = \left(\frac{t_N}{t_1} \right)^{\frac{1}{NT-1}} \quad \text{.....3.78}$$

Thus the time point can be calculated by

$$t_n = t_1 a_{\lg t}^n \quad \text{.....3.79}$$

and the time spacing is given by

$$\Delta t_n = t_1 a_{\lg t}^{n-1} \left(a_{\lg t} - 1 \right) \quad \text{.....3.80}$$

3.4 SOLUTION PROCEDURE FOR THE COUPLED MODEL

After developing the wellbore and reservoir model, we can couple them together to solve for transient temperature and pressure profiles in formation and along the wellbore. It should be noted that besides the equations we presented above, some fluid property correlations are also employed to close the equation system. To solve the coupled wellbore/reservoir model, there are three major steps, which are shown as different sections in the following program flow chart (**Fig. 3.3**).

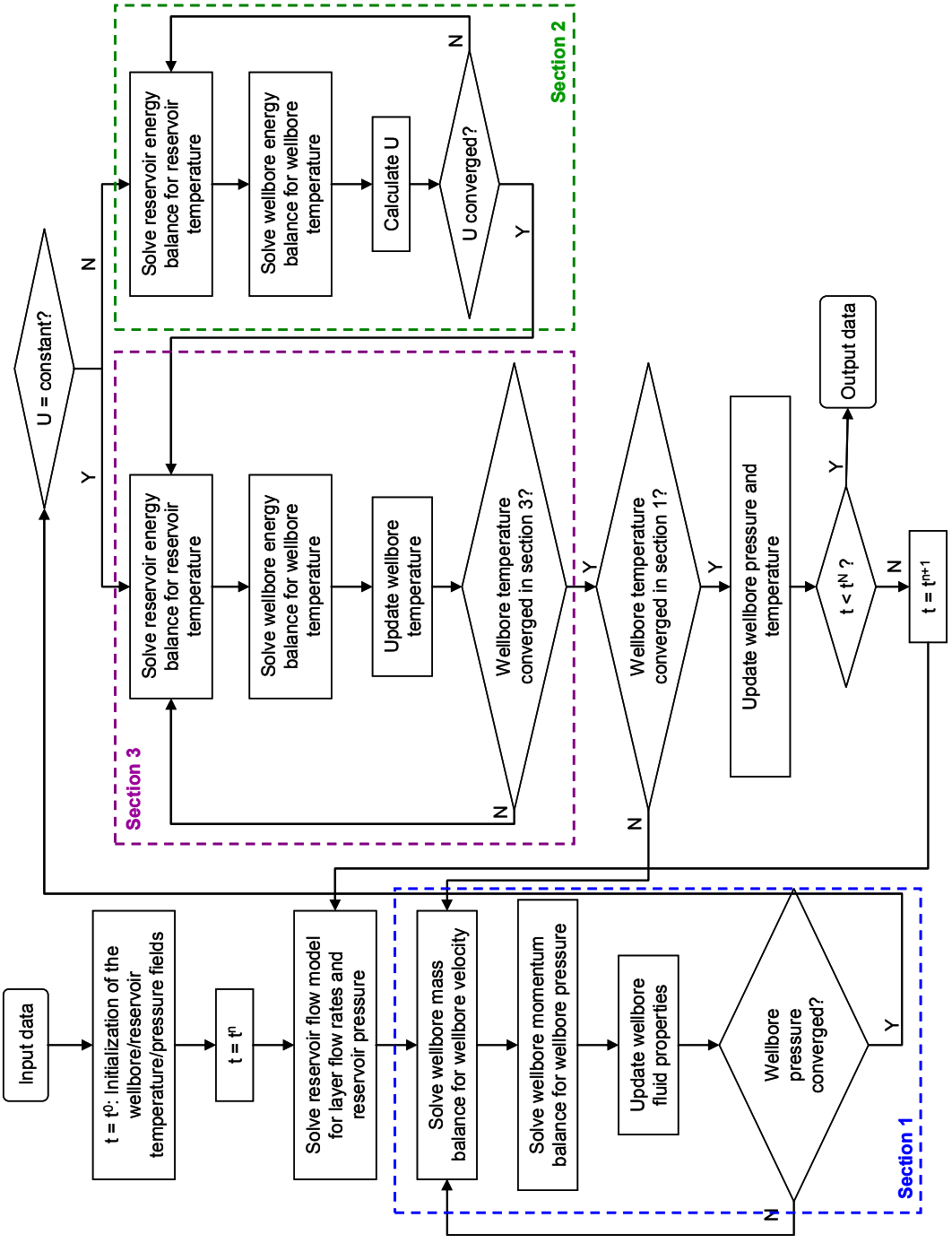

Fig. 3.3 Schematic of the solution procedure

The wellbore/reservoir temperature and pressure fields are initialized using initial conditions. At the nth time step, the reservoir flow model is solved first for layer flow rates and reservoir pressure distribution. Then the wellbore flow model (wellbore mass and momentum balance equations) is solved iteratively for wellbore velocity and pressure distribution until wellbore pressure converges (Section 1). If the overall heat transfer coefficient (U) between wellbore and formation needs to be calculated rigorously, since the annular fluid properties depends on the formation and wellbore fluid temperature, the reservoir and wellbore energy balance equation are solved iteratively until U converges (Section 2); otherwise, the overall heat transfer coefficient will be assumed as a constant and go to Section 3, where the reservoir and wellbore energy balance equations are solved iteratively until wellbore temperature converges. Then the obtained wellbore temperature are used to solve wellbore flow model again, the iteration lasts until wellbore temperature converges. At next time step t^{n+1} , the wellbore/reservoir temperature and pressure fields at the nth time step will be used as initial distributions, and the same procedure will be repeated.

3.5 FORWARD MODEL VALIDATION

The coupled wellbore/reservoir model established in this work is validated in several ways. Since the wellbore flow/thermal model and reservoir flow model have been validated in previous works (Yoshioka, 2007; Ehlig-Economides, 1987), here we will mainly address the validation of the reservoir thermal model. First, the results from transient reservoir thermal model are compared with the steady-state solutions for productive zones. Second, the transient reservoir thermal model results are compared with Ramey's solution for overburden regions. Finally, the coupled wellbore/reservoir model results are compared with the numerical solution given by the *Rubis* module in software package *Ecrin* v4.10.

3.5.1 Comparison with Steady-state Solutions

The transient formation energy balance equation (Eq. **2.59**) is solved numerically using finite difference method to simulate formation temperature behavior during the transient test. Assuming the vertical heat conduction can be neglected, the formation energy balance equation in steady-state form (Eq. **3.81**) (Yoshioka, 2007) can be solved analytically as follows,

$$\frac{2\pi hK_T}{q}r^2\frac{d^2T_o}{dr^2}-\left(\rho\hat{C}_p-\frac{2\pi hK_T}{q}\right)r\frac{dT_o}{dr}-\left(\frac{q\mu}{2\pi kh}\right)\beta T_o+\frac{q\mu}{2\pi kh}=0 \quad \text{.....3.81}$$

Similarly, for the near-wellbore damage region, the energy balance equation is written as

$$\frac{2\pi hK_T}{q}r^2\frac{d^2T_d}{dr^2}-\left(\rho\hat{C}_p-\frac{2\pi hK_T}{q}\right)r\frac{dT_d}{dr}-\left(\frac{q\mu}{2\pi k_s h}\right)\beta T_d+\frac{q\mu}{2\pi k_s h}=0 \quad \text{.....3.82}$$

The boundary conditions are as follows. For outer boundary, the formation temperature is assumed to be geothermal temperature,

$$T=T_e \text{ at } r=r_e \quad \text{.....3.83}$$

For inner boundary at the well, the radiation boundary condition is applied,

$$K_T\left.\frac{dT}{dr}\right|_{r=r_w}=U\left(T\big|_{r=r_w}-T_f\right) \text{ at } r=r_w \quad \text{.....3.84}$$

At the joint point between damage and undamage region, the temperature and heat flux are considered to be identical,

$$T_o = T_d \quad \text{at } r = r_d \qquad \text{.....3.85}$$

and

$$\frac{dT_o}{dr} = \frac{dT_d}{dr} \quad \text{at } r = r_d \qquad \text{.....3.86}$$

The solutions of the 2nd-order PDEs (Eqs. **3.81** and **3.82**) are

$$T_o(r) = \frac{1}{\beta} + c_1 r^{m_1} + c_2 r^{m_2} \qquad \text{.....3.87}$$

$$T_d(r) = \frac{1}{\beta} + c_3 r^{m_3} + c_4 r^{m_4} \qquad \text{.....3.88}$$

where

$$m_1 = \frac{q}{4\pi h}\left[\frac{\rho\hat{C}_p}{K_T} + \sqrt{\left(\frac{\rho\hat{C}_p}{K_T}\right)^2 + \frac{4\mu\beta}{kK_T}}\right] \qquad \text{.....3.89}$$

$$m_2 = \frac{q}{4\pi h}\left[\frac{\rho\hat{C}_p}{K_T} - \sqrt{\left(\frac{\rho\hat{C}_p}{K_T}\right)^2 + \frac{4\mu\beta}{kK_T}}\right] \qquad \text{.....3.90}$$

$$m_3 = \frac{q}{4\pi h}\left[\frac{\rho\hat{C}_p}{K_T} + \sqrt{\left(\frac{\rho\hat{C}_p}{K_T}\right)^2 + \frac{4\mu\beta}{k_s K_T}}\right] \qquad \text{.....3.91}$$

$$m_4 = \frac{q}{4\pi h}\left[\frac{\rho\hat{C}_p}{K_T} - \sqrt{\left(\frac{\rho\hat{C}_p}{K_T}\right)^2 + \frac{4\mu\beta}{k_s K_T}}\right] \qquad \text{.....3.92}$$

Applying the boundary conditions, we can determine the coefficients c_1, c_2, c_3, and c_4 as follows,

$$\begin{aligned} c_1 = \Big\{ & r_d^{\,m_2}\Big[(m_2 - m_4) r_d^{\,m_4} r_w^{\,m_3}\left(K_T m_3 - U r_w\right) \\ & - (m_2 - m_3) r_d^{\,m_3} r_w^{\,m_4}\left(K_T m_4 - U r_w\right)\Big]\left(-1 + \beta T_e\right) \\ & + U(m_3 - m_4) r_d^{\,m_3+m_4} r_e^{\,m_2} r_w\left(-1 + \beta T_f\right)\Big\} \Big/ D' \end{aligned} \qquad \text{.....3.93}$$

$$c_2 = \{r_d^{m_1}[-(m_1-m_4)r_d^{m_4}r_w^{m_3}(K_T m_3 - Ur_w) + (m_1-m_3)r_d^{m_3}r_w^{m_4}(K_T m_4 - Ur_w)](-1+\beta T_e) - U(m_3-m_4)r_d^{m_3+m_4}r_e^{m_1}r_w(-1+\beta T_f)\}/D' \quad \text{.....3.94}$$

$$c_3 = \{(m_1-m_2)r_d^{m_1+m_2}r_w^{m_4}(K_T m_4 - Ur_w)(-1+\beta T_e) + Ur_d^{m_4}[(-m_2+m_4)r_d^{m_2}r_e^{m_1} + (m_1-m_4)r_d^{m_1}r_e^{m_2}] r_w(-1+\beta T_f)\}/D' \quad \text{.....3.95}$$

$$c_3 = \{-(m_1-m_2)r_d^{m_1+m_2}r_w^{m_3}(K_T m_3 - Ur_w)(-1+\beta T_e) + Ur_d^{m_3}[(m_2-m_3)r_d^{m_2}r_e^{m_1} + (-m_1+m_3)r_d^{m_1}r_e^{m_2}] r_w(-1+\beta T_f)\}/D' \quad \text{.....3.96}$$

where

$$D' = \beta r_d^{m_4}[(m_2-m_4)r_d^{m_2}r_e^{m_1} + (-m_1+m_4)r_d^{m_1}r_e^{m_2}]r_w^{m_3}(K_T m_3 - Ur_w) + \beta r_d^{m_3}[(-m_2+m_3)r_d^{m_2}r_e^{m_1} + (m_1-m_3)r_d^{m_1}r_e^{m_2}]r_w^{m_4}(K_T m_4 - Ur_w) \quad \text{.....3.97}$$

According to the steady-state solutions derived above, we can compare the results of steady-state model and transient model for a fixed pressure distribution. A production well diagram from field is used for this comparison. This new production well is drilled through a 20m gas zone and a 2m oil zone, and only the oil zone is producing now. The well is perforated for producing the oil zone from 1872m to 1874m, and the production rate is 600 STB/d. The productive zone has a skin factor of 10, and the damage radius is assumed to be 1.2 ft. The well has a constant-pressure boundary at 1000 ft away from borehole. Unless otherwise specified, the same wellbore and reservoir diagram will also be used for the following two comparisons. Reservoir and fluid properties are listed in **Table 3.1**.

In this case, the steady-state reservoir pressure distribution at 1873 m is shown in **Fig. 3.4**. Reservoir temperature distribution at 1873 m calculated from steady-state solution and transient solution are shown in **Fig. 3.5**. We can see that the transient solution can match the steady-state solution at t = 50,000 days.

Table 3.1 Reservoir and fluid properties

Overall heat transfer coefficient (Btu/D/ft^2)	63.4
Oil Formation Volume Factor (bbl/STB):	1.4
Oil thermal conductivity (Btu/D/ft/ F):	1.9
Oil specific heat capacity (Btu/lbm/ F):	0.4
Formation thermal conductivity (Btu/D/ft/ F):	30.0
Rock specific heat capacity (Btu/lbm /F):	0.3
Rock density (lbm/ft^3):	140.0
Oil density (kg/m^3):	722.5

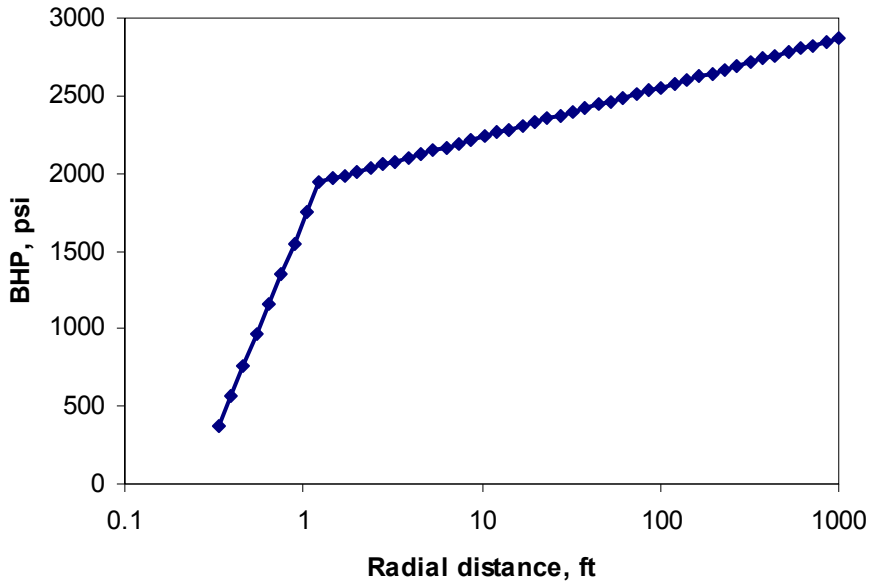

Fig. 3.4 Reservoir pressure distribution in producing layer

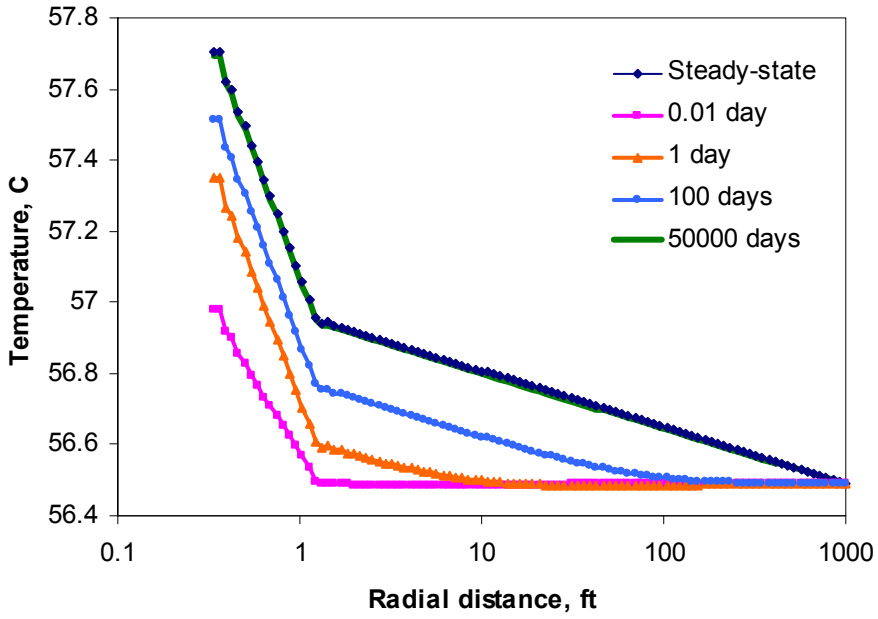

Fig. 3.5 Reservoir temperature distribution in producing layer

3.5.2 Comparison with the Ramey Solution

If a constant production rate is assumed, the heat transfer between wellbore and the overburden formation can be approximated by using the Ramey (1962) solution for single-phase fluid flow in a vertical well. For a production well, the wellbore temperature profile can be calculated by solving

$$\frac{\partial T_f}{\partial z}+\frac{T_f}{A}-\frac{T_{Ge}}{A}=0 \quad \text{.....3.98}$$

where

$$A=\frac{q\rho_f C_f\left[k_h+r_{ci}Uf(t)\right]}{2\pi r_{ci}Uk_h} \quad \text{.....3.99}$$

$$f(t)\cong -\ln\left(r_{ce}/2\sqrt{\kappa t}\right)-0.290 \quad \text{.....3.100}$$

The solution is given by (Curtis and Witterholt, 1973)

$$T_f(z,t)=T_{Ge}-g_G z+g_G A+\left(T_{fe}-T_{Ge}-g_G A\right)e^{-z/A} \quad \text{.....3.101}$$

Considering the same reservoir and wellbore scenarios used in Section 3.5.1 and assuming the well has been producing for 50 days, we can calculate wellbore temperature for overburden region which is above 1872 m using Eq. **3.101** and the transient reservoir thermal model. The calculated temperature profiles are presented in **Fig. 3.6**, which shows close results between two methods. Comparing Eq. **2.35** and Eq. **3.98**, we can see that the transient temperature model developed in this work can take into account Joule-Thomson effect and can be applied for compressible fluids, while Ramey's solution cannot, which results in the mismatch in **Fig. 3.6**. A better match can be obtained by turning off the Joule-Thomson term and using a constant fluid density in the transient model. The matching results are shown in **Fig. 3.7** where we can see that two methods can achieve a fairly good agreement.

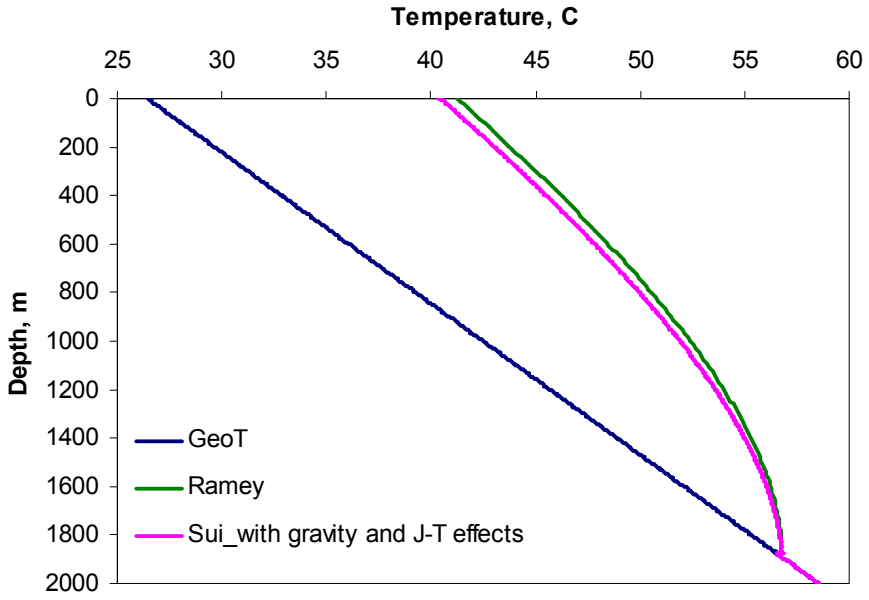

Fig. 3.6 Wellbore temperature profiles given by Ramey's solution and developed transient model (t = 50 days) with Joule-Thomson effect and changing fluid density

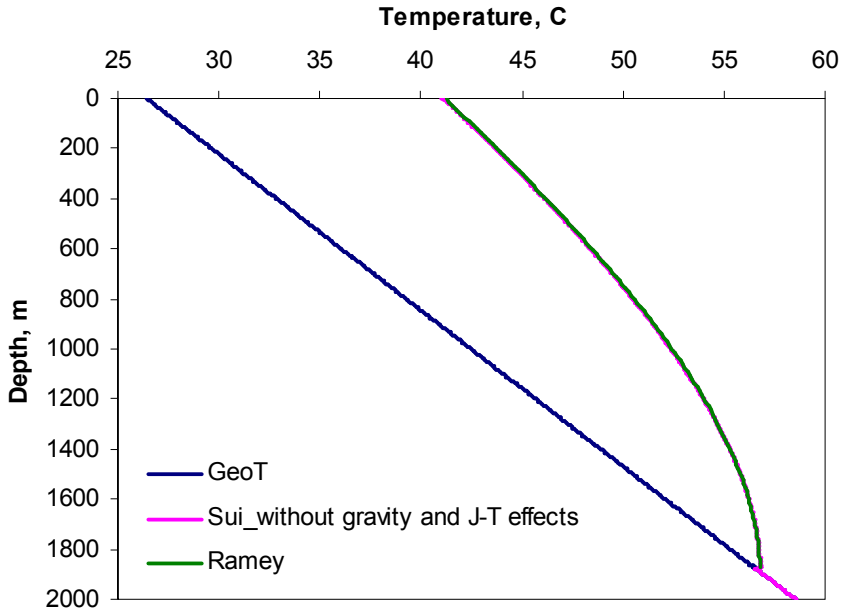

Fig. 3.7 Wellbore temperature profiles given by Ramey's solution and developed transient model (t = 50 days) without Joule-Thomson effect and changing fluid density

3.5.3 Comparison with the Numerical Solution

With a popular application of temperature sensors, the thermal option has been incorporated into some reservoir simulators with the subtle thermal effects like Joule-Thomson effect taken into account. The numerical model developed in the *Rubis* software has been used to compare with our model. Some characteristics in both models are listed in **Table 3.2**. The reservoir model and wellbore model has been compared in **Table 3.3** and **Table 3.4**.

Table 3.2 Model characteristic comparison

	Sui	***Rubis***
Phase	Single phase fluid flow (oil/gas-without Non Darcy effect)	Single phase fluid flow (oil/gas-with Non Darcy effect)
Dimension	2D (r, z), single well	3D (x, y, z), multiple wells
Symmetry	Symmetry w.r.t. well axis	Not required well-centered symmetry

Table 3.2 Continued

	Sui	***Rubis***
Grid	structured, logarithmic grid in radial direction; structured, local grid refinement	unstructured, Voronoi grid in horizontal direction; structured, local grid refinement in vertical direction
Formulation Discretization	Finite volume, upstream scheme	Finite volume, upstream scheme
Rock properties	Constant: permeability, porosity, rock density, rock thermal conductivity	Constant: permeability, Forchheimer coefficient, porosity, rock density, rock thermal conductivity
Fluid PVT properties	Depending on *P* and *T* (viscosity, density, thermal conductivity)	Depending on *P* and *T* (viscosity, density, thermal conductivity, fluid mass enthalpy)
Reservoir Model	Solve *P* and *T* sequentially	Solve *P* and *T* simultaneously
Well/Reservoir Coupled Model	Solved sequentially	Solved sequentially

Table 3.3 Reservoir model comparison

Reservoir Model	**Sui**	***Rubis***
Equation	Darcy's Law equation Mass conservation equation Energy conservation equation (without considering potential energy)	Forchheimer equation Mass conservation equation Energy conservation equation (considering potential energy)
Boundary conditions	1. Pressure: constant pressure or no flow at lateral boundary; 2. Temperature: geothermal temperature at the reservoir lateral, bottom and top bounds.	1. Pressure: constant pressure / no flow / aquifer (numerical or analytical) at lateral, bottom and top bounds; 2. Temperature: geothermal temperature at the reservoir lateral, bottom and top bounds.
Solution	3. Derive multilayer solution by using Darcy's law, mass conservation equation and appropriate boundary conditions; 4. Solve reservoir pressure first and then substitute it into energy balance equation for solving reservoir temperature.	Solve reservoir pressure and temperature simultaneously.

Table 3.4 Wellbore model comparison

Wellbore Model	**Sui**	***Rubis***
Equation	Mass balance equation Momentum balance equation (stationary) Energy balance equation (transient)	Mass conservation equation Pressure drop equation (stationary) Energy conservation equation (transient)
Constraint equation	1. Constant surface flow rate 2. Temperature at bottom is geothermal temperature	1. Mass constraint equation: flow rate or pressure; 2. Energy constraint equation: for producer, the temperature at the top reference point is known.
Assumption	1. Vertical conduction can be neglected; 2. Pressure drop due to kinetic energy change can be neglected.	1. Vertical conduction can be neglected; 2. Pressure drop due to kinetic energy change can be neglected.

From above comparisons, we can see that *Rubis* model is a 3D single-phase reservoir simulator that can simulate multiple wells simultaneously, and it can be used for gas reservoir with the consideration of non-Darcy effect. However, for the purpose of inversing formation properties by nonlinear regression, the single-well simulator is much more efficient. The case in Section 3.5.1 is used here for comparison. Rubis model and the model from this work are both used for calculating bottomhole pressure and wellbore temperature profile. Bottomhole pressure during transient test is shown in **Fig. 3.8**. Wellbore temperature profile and the temperature history profiless at different stations are shown in **Fig. 3.9** and **Fig. 3.10**. The comparison results show a reasonable match between two models.

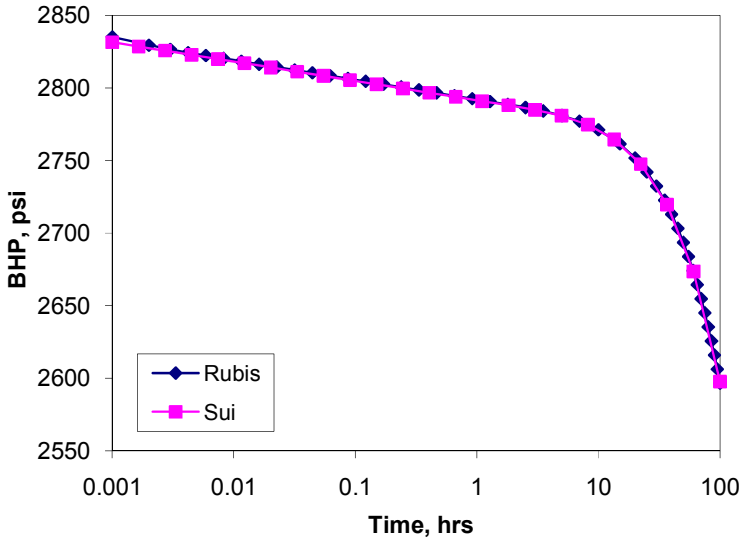

Fig. 3.8 Bottomhole pressure during transient test

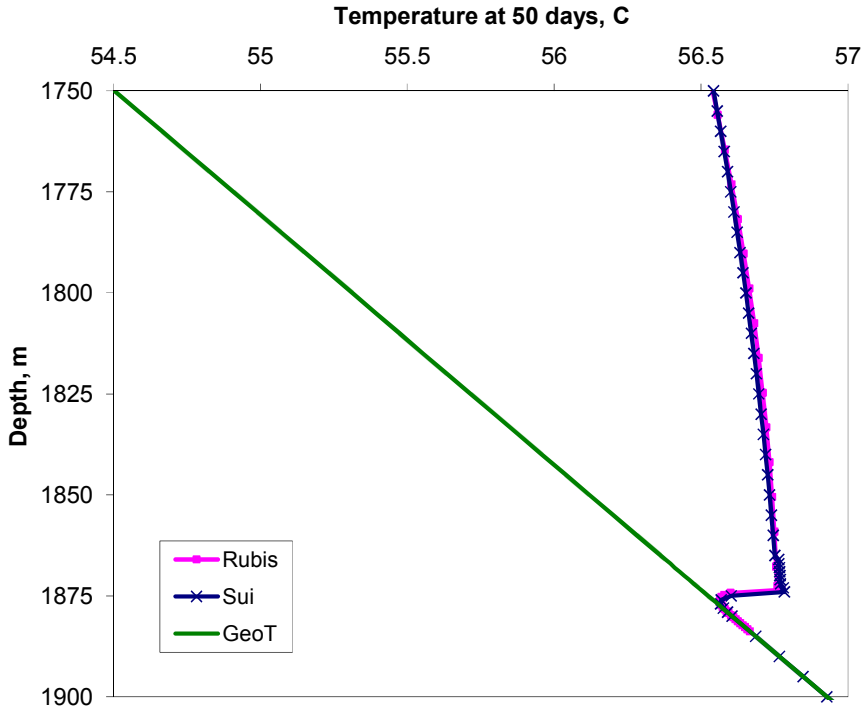

Fig. 3.9 Wellbore temperature profile at t = 100 hrs

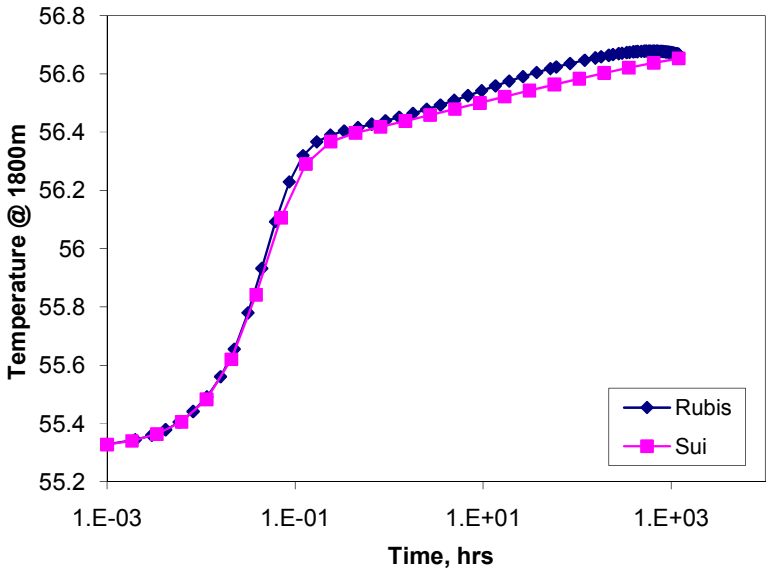

Fig. 3.10 Temperature history profiles during test for the model comparison case

3.6 ILLUSTRATIVE EXAMPLE

A hypothetical example will be presented to illustrate how the forward model can be used to simulate the transient temperature and pressure for the proposed testing method. The fluid and formation parameters are given in **Table 3.5**.

Table 3.5 Reservoir and fluid properties for a two-layer case

Initial reservoir pressure at reference depth (psi)	5920
Formation surface temperature (°C)	15
Geothermal gradient (°C/m)	0.018
Reference depth (m)	3550
Wellbore radius (ft)	0.27
Porosity	0.2
Total system compressibility (psi^{-1})	1.9e-5

A commingled oil reservoir shown in **Fig. 3.11** has two layers with different permeability and skin, where the skin is caused by formation damage. The layer properties are given in **Table 3.6**.

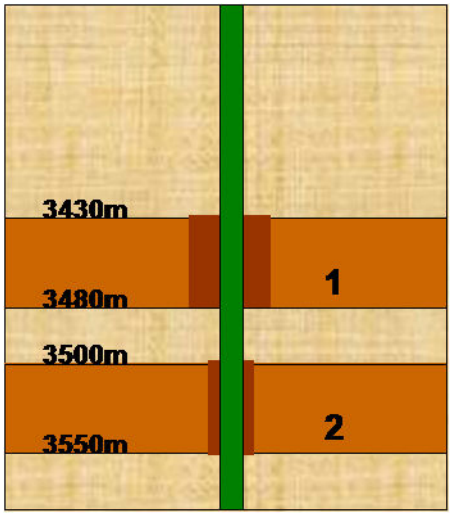

Fig. 3.11 Reservoir diagram for the illustrative example

Table 3.6 Layer properties for the two-layer case

	k (md)	k_s (md)	r_s (ft)	s
Layer 1	100	14.4	1.45	10
Layer 2	60	13.1	0.63	3

The production rate scheme is shown in **Fig. 3.12**. Assume the oil cumulative production for this well before the transient test is $N_p = 3.33\times10^5$ STB and the last production rate is $q_{last} = 8{,}000$ STB/d. To start the transient test, the surface production rate is cut back to be 4,000 STB/d for 24 hrs. According to Horner's approximation method, the pseudoproducing time can be calculated by

$$t_{pH} = \frac{N_p}{q_{last}} = 1{,}000 \text{ hrs} \quad \text{.....3.102}$$

Thus the actual flow rate history can be simplified as 1000hr production at the rate of 8,000 STB/d and 24hr production at the rate of 4,000 STB/d, which is shown in **Fig. 3.13**.

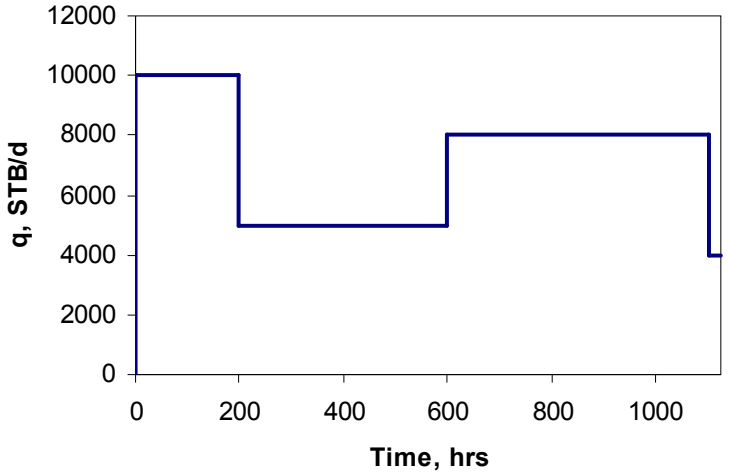

Fig. 3.12 Actual production rate scheme

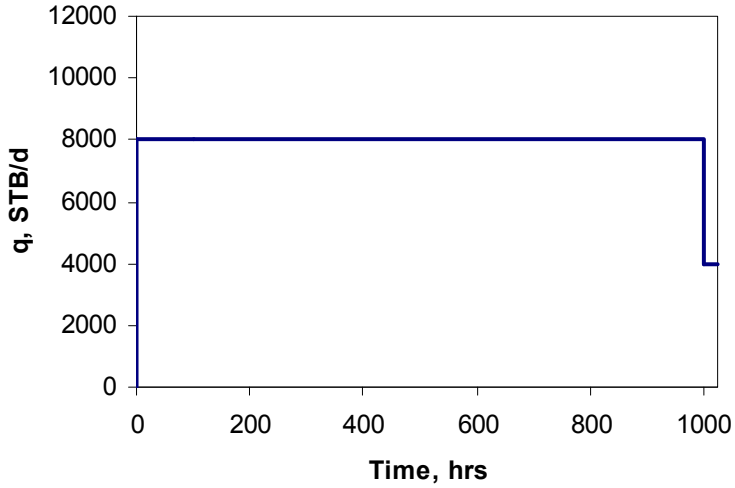

Fig. 3.13 Simplified production rate scheme

Since both mass and energy are conserved, representing the production history by 1,000-hr of production at the rate of 8,000 STB/d provides the same layer pressures, and the same temperature profile at the start of the test as would result from the actual rate history, as shown by the last computed pressures in **Fig. 3.14** and the last computed temperatures in **Fig. 3.15**. If we use $p_s(t_{pH})$ and $T_s(t_{pH})$ to denote the last computed

pressure and temperature for the single-rate history, and use $p_m(t_p)$ and $T_m(t_p)$ for the actual rate history, we can see that $p_s(t_{pH}) = p_m(t_p)$ and $T_s(t_{pH}) = T_m(t_p)$.

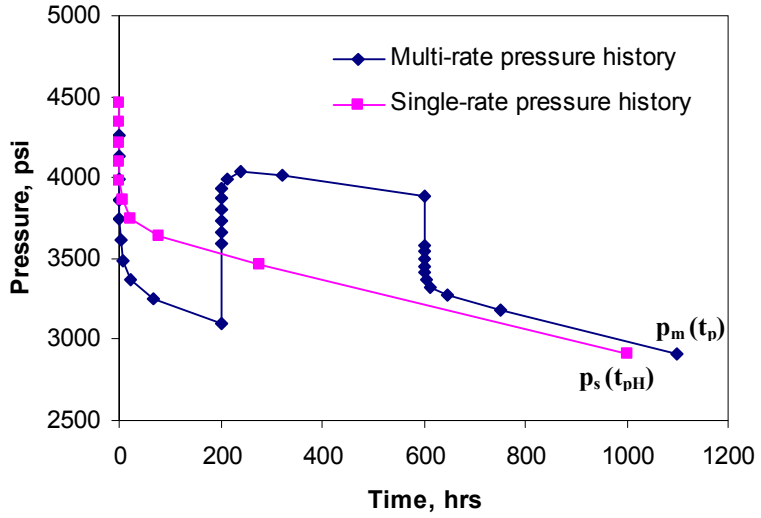

Fig. 3.14 Pressure history comparison

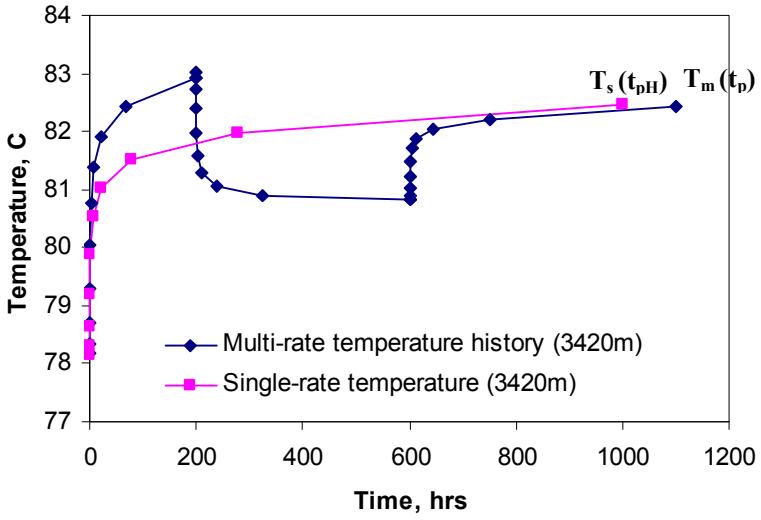

Fig. 3.15 Temperature history comparison

For simplicity, we assume the wellbore storage coefficient to be zero in this case. It should be noted that the length of the test period depends on specific fluid and reservoir properties. In general, an appropriate time length should be designed using the forward simulator with approximated formation properties. The time length of the transient test must be long enough to see the transient temperature variations caused by skin factors in the various layers.

The developed forward model can be used to simulate the temperature distribution along the wellbore (**Fig. 3.16**) and the pressure at bottom of the flowing interval during the 24-hr test. The log-log pressure change and derivative curves plotted in **Fig. 3.17** shows apparent radial flow followed by a drop in the derivative showing the superposition effect caused by the rate cut back. To apply the new testing approach, only the temperature values at specific locations are required. In this case, temperature data at the bottom of the reservoir (3550m) and the temperature data at the top of each layer (3490m and 3420m) are required for later interpretation. The temperature histories at these depths during the test can be seen in **Fig. 3.18**. The logarithmic time step has been adopted in the forward simulator to accelerate the simulation. From **Fig. 3.18**, we can see that this time step strategy provides the early time temperature behavior very well. The observed temperature trends are different above and below the upper layer.

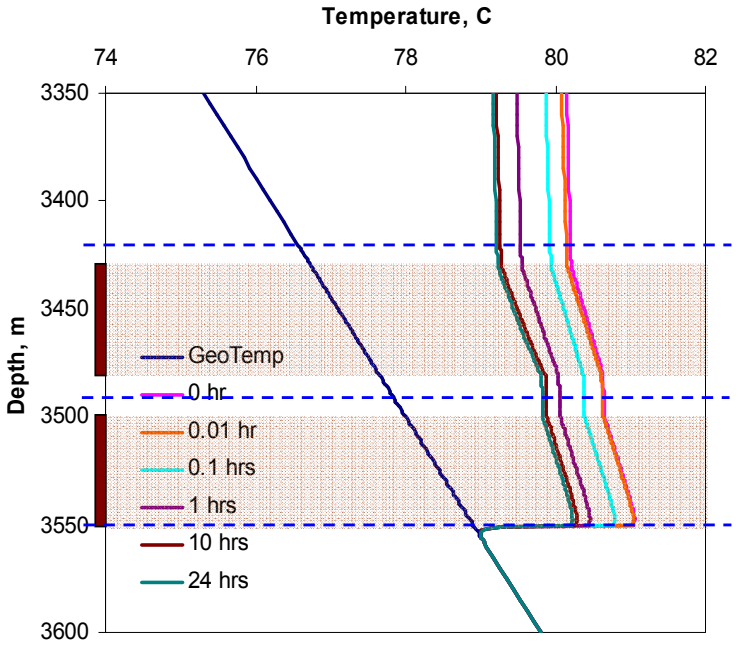

Fig. 3.16 Transient temperature profile during test for the illustrative example

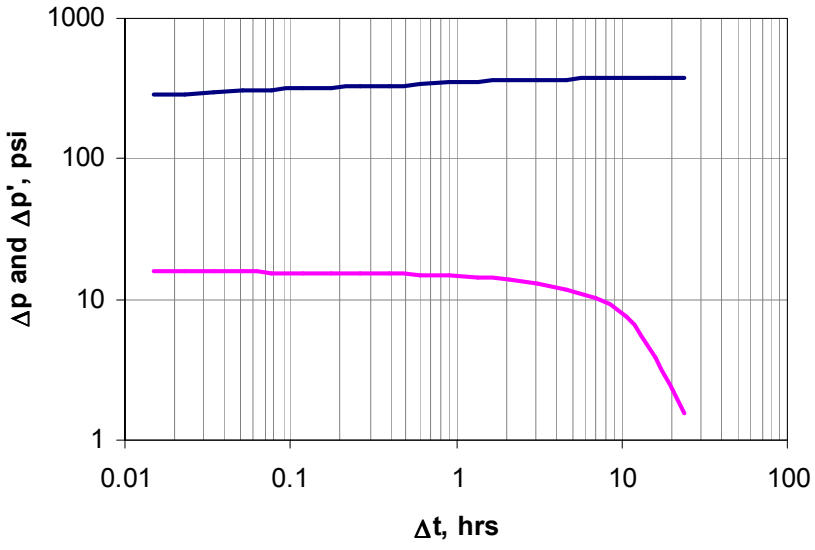

Fig. 3.17 Log-log pressure change and derivative during test for the illustrative example

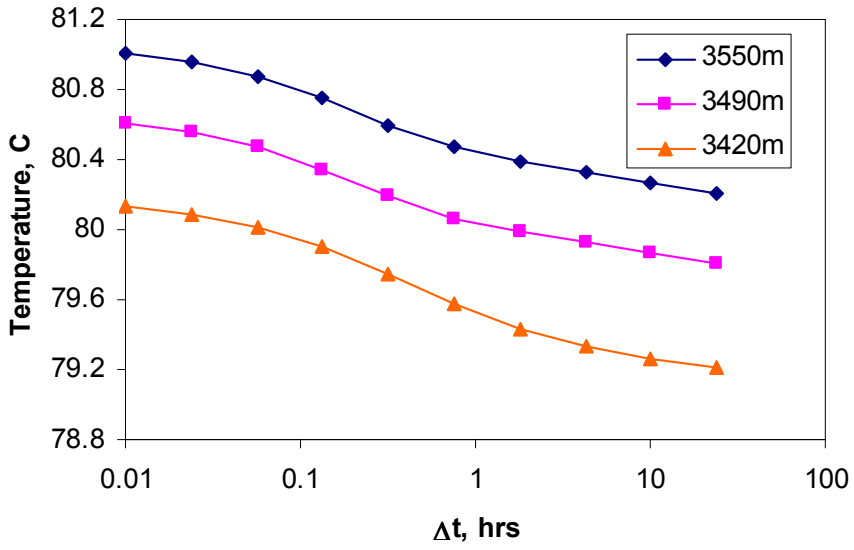

Fig. 3.18 Temperature history profiles during test for the illustrative example

In addition, the formation temperature distribution was also simulated by solving the reservoir energy balance equation. The formation temperature field was generated at each time step to help understand the transient temperature variations during test. **Fig. 3.19** shows the temperature changes from geothermal temperature at the start of the test, i.e. $\Delta T_1 = T - T_G$. The temperature difference presentation removes the effect of the geothermal temperature gradient. The temperature change is greater near the wellbore in the upper layer and appears over a greater skin radius as expected given the model inputs. Because of its low permeability, the lower layer has a greater pressure drop outside the damage radius.

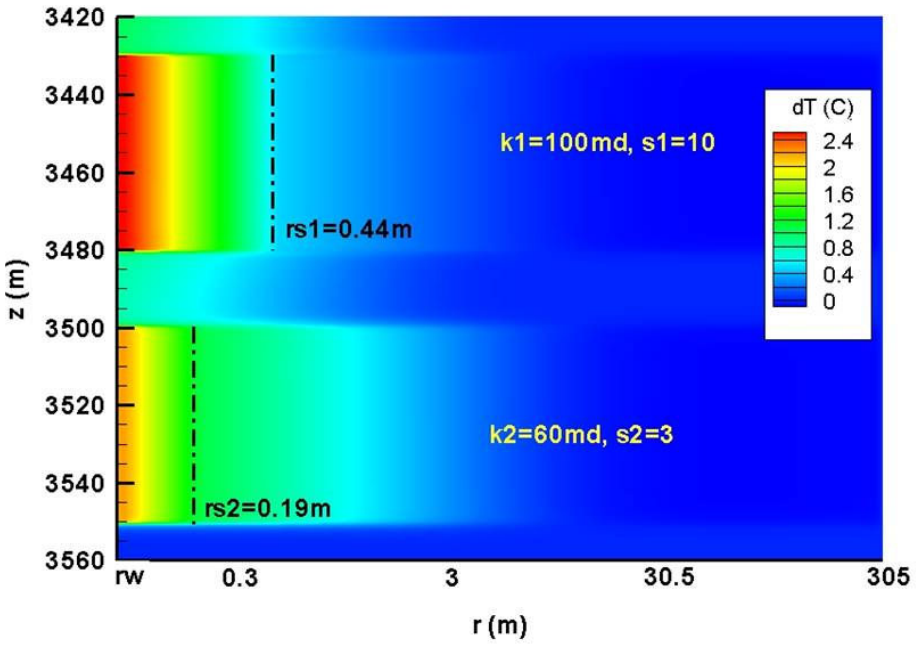

Fig. 3.19 Formation temperature change at the start of test (ΔT1)

4 INVERSE MODEL

4.1 METHODOLOGY

The forward model described in previous section is used to simulate and understand the transient temperature and pressure response to variations of layer permeabilities and skin factors, while the inverse model is developed to determine layer permeability and skin factor from the measured temperature and pressure data. Since the forward model is developed for a transient condition, we are matching the history of temperature and pressure during the transient flow period. By matching the history of temperature and pressure, the unique solution of formation properties can be determined, a proven previous theory of Multilayer Transient Test.

In the inverse model, we regard transient temperature and pressure measurements as observation data, and formation properties as parameters to be estimated. Some selected measured temperature and pressure data will be input into the inverse simulator as observation data. Meanwhile, some arbitrary initial guesses of the formation properties are also input into the inverse simulator. The inverse simulator can simulate the temperature and pressure responses using the initial guesses of the formation properties and calculate the discrepancy between the simulated and measured data. By applying the Levenberg-Marquardt algorithm, the layer properties can be updated in each iteration step until the discrepancy is minimized.

4.2 LEAST-SQUARE REGRESSION

The inverse model can be considered as a least-squares nonlinear regression problem. An objective function is constructed to describe the discrepancy between measured and

---

* Part of this chapter is reprinted with permission from "Determining Multilayer Formation Properties from Transient Temperature and Pressure Measurements" by Sui, W., Zhu, D., Hill, A.D., and Ehlig-Economides, C., 2007. Paper SPE 116270 presented at the SPE Annual Technical Conference and Exhibition, Denver, Colorado, 21-24 September.

simulated temperature and pressure data.

The inverse model can be considered as a least-squares nonlinear regression problem. An objective function is constructed to describe the discrepancy between measured and simulated temperature and pressure data.

$$\mathbf{f}(\mathbf{x}) = \frac{1}{2}\left\|\mathbf{d} - \mathbf{g}(\mathbf{x})\right\|_2^2 = \frac{1}{2}\left(\mathbf{d} - \mathbf{g}(\mathbf{x})\right)^T \mathbf{C}_n^{-1}\left(\mathbf{d} - \mathbf{g}(\mathbf{x})\right) \quad \text{.....4.1}$$

where **x** represents the formation properties (layer permeability, damage permeability, and damage radius); **d** represents the measured temperature and pressure data; **g**(**x**) is the simulated temperature and pressure data; $\mathbf{C}_n$ is the the covariance matrix to take into account measurement errors and different units of different type of data.

Assume there are N productive layers in the reservoir, the vector **x** representing individual layer properties has a dimension of $3N \times 1$ and can be written as follows,

$$\mathbf{x} = \left[k_1, k_2, \cdots, k_N, k_{s1}, k_{s2}, \cdots, k_{sN}, r_{s1}, r_{s2}, \cdots, r_{sN}\right]^T_{3N\times 1} \quad \text{.....4.2}$$

According to the proposed testing procedure, the wellbore pressure and temperature at the bottom of the reservoir and temperature at the top of each productive layer are required to be measured. For an N-layer reservoir, the measurements from (N+1) locations are required for interpretation. During a transient flow test, assuming the measurements from M different time points are used for inversion, the vectors **d** and **g**(**x**) both have a dimension of $M(N+2)\times 1$.

$$\mathbf{d} = \left[p_{o11}, T_{o11}, \cdots, T_{o1(N+1)}, \cdots, p_{oM1}, T_{oM1}, \cdots, T_{oM(N+1)}\right]^T_{M(N+2)\times 1} \quad \text{.....4.3}$$

$$\mathbf{g}(\mathbf{x}) = \left[p_{c11}, T_{c11}, \cdots, T_{c1(N+1)}, \cdots, p_{cM1}, T_{cM1}, \cdots, T_{cM(N+1)}\right]^T_{M(N+2)\times 1} \quad \text{.....4.4}$$

Additionally, the matrix C_n is a diagonal matrix and has a dimension of $M(N+2)\times M(N+2)$.

$$\mathbf{C}_n = \begin{bmatrix} \sigma_{p11}^2 & & & & & & & \\ & \sigma_{T11}^2 & & & & & & \\ & & \ddots & & & & & \\ & & & \sigma_{T1(N+1)}^2 & & & & \\ & & & & \ddots & & & \\ & & & & & \sigma_{pM1}^2 & & \\ & & & & & & \sigma_{TM1}^2 & \\ & & & & & & & \ddots \\ & & & & & & & & \sigma_{TM(N+1)}^2 \end{bmatrix}_{M(N+2)\times M(N+2)} \quad \text{.....4.5}$$

The matrix C_n is called observation weight matrix, which is used to consider the problem in parameter estimation caused by different types of data. It is very common to have several different types of data measurements used simultaneously in the regression procedure. Since the units of different data types are different, the numbers used to represent them may be of vastly different magnitudes such as pressure in *Pascal* and temperature in *Kelvin*. Under this circumstance, the larger numbers will dominate the estimation and the small number will be neglected improperly. This issue can be overcome by using the observation weight matrix. In this work, we assign the weight for pressure variable is 1, and the weight for temperature is 6.25×10^{12}, which is from a common Joule-Thomson coefficient for oil (Yoshioka, 2007):

$$K_{JT} = \left(\frac{\Delta T}{\Delta p}\right)_H = \frac{1}{6.25\times10^{12}}\frac{\mathrm{K}}{\mathrm{Pa}} \quad \text{.....4.6}$$

To simplify the objective function (Eq. **4.1**), we define **e** as

$$\begin{aligned} \mathbf{e} &= \mathbf{C}_n^{-1/2}\left(\mathbf{d}-\mathbf{g}(\mathbf{x})\right) \\ &= \mathbf{C}_n^{-1/2}\big[p_{o11}-p_{c11}, T_{o11}-T_{c11}, \cdots, T_{o1(N+1)}-T_{c1(N+1)}, \cdots, \\ &\qquad p_{oM1}-p_{cM1}, T_{oM1}-T_{cM1}, \cdots, T_{oM(N+1)}-T_{cM(N+1)}\big]^T_{M(N+2)\times1} \end{aligned} \quad \text{.....4.7}$$

then the objective function Eq. **4.1** is simplified into

$$\mathbf{f}(\mathbf{x}) = \frac{1}{2}\mathbf{e}^{\mathrm{T}}\mathbf{e} \quad \text{.....4.8}$$

The objective function can be minimized by updating the parameter vector **x** iteratively,

$$\mathbf{x}_{m+1} = \mathbf{x}_m + \delta\mathbf{x}_m, \quad (4.9)$$

until we get small enough residuals

$$\mathbf{f}(\mathbf{x}_m) - \mathbf{f}(\mathbf{x}_{m+1}) \le \varepsilon_1, \quad (4.10)$$

or small enough relative error for certain times.

$$\frac{\mathbf{f}(\mathbf{x}_m) - \mathbf{f}(\mathbf{x}_{m+1})}{\mathbf{f}(\mathbf{x}_m)} \le \varepsilon_2. \quad (4.11)$$

Since iterating to convergence (to the machine accuracy or to the roundoff limit) is usually wasteful and unnecessary, we usually use the stopping condition given by Eq. **4.11** instead of that given by Eq. **4.10**. Then we believe we get the best-fit between data and model.

4.3 REALIZATION OF LEVENBERG-MARQURDT METHOD

For Eq. **4.9**, we have several options for updating x_m. Here the Levenberg-Marquardt algorithm is used. The Levenberg-Marquardt algorithm is a blend of the Gauss-Newton algorithm and the gradient descent method. Since the Levenberg-Marquardt algorithm works well in practice, it has become the standard nonlinear least-squares routine. The Levenberg-Marquardt step-size is given by

$$\delta\mathbf{x}_m = -(\mathbf{H} + \lambda\mathbf{I})^{-1}\mathbf{w} = -(\mathbf{J}^{\mathrm{T}}\mathbf{J} + \lambda\mathbf{I})^{-1}\mathbf{J}^{\mathrm{T}}\mathbf{e}, \quad (4.12)$$

where **w** is the gradient of $f(\mathbf{x})$,

$$\nabla\mathbf{f}(\mathbf{x}) = \mathbf{w} = \mathbf{J}^{\mathrm{T}}\mathbf{e}, \quad (4.13)$$

and Jacobian matrix is defined as the gradient of **e**,

$$\mathbf{J} = \nabla\mathbf{e} = \begin{bmatrix} \frac{\partial e_1}{\partial x_1} & \frac{\partial e_1}{\partial x_2} & \cdots & \frac{\partial e_1}{\partial x_n} \\ \frac{\partial e_2}{\partial x_1} & \frac{\partial e_2}{\partial x_2} & \cdots & \frac{\partial e_2}{\partial x_n} \\ \cdots & \cdots & \cdots & \cdots \\ \frac{\partial e_m}{\partial x_1} & \frac{\partial e_m}{\partial x_2} & \cdots & \frac{\partial e_m}{\partial x_n} \end{bmatrix}. \quad (4.14)$$

Here **H** is the Hessian matrix of $f(\mathbf{x})$, and the rigorous solution of Hessian matrix should be

$$\mathbf{H} = \mathbf{J}^{\mathrm{T}}\mathbf{J} + \sum_{i=1}^{m} e_i T_i \,, \qquad \text{.....4.15}$$

where m is the number of elements in **e**, **T** is the Hessian matrix of **e**. For low residuals or quasi-linear system, the **H** can be approximated by

$$\mathbf{H} = \mathbf{J}^{\mathrm{T}}\mathbf{J} \qquad \text{.....4.16}$$

It should be noted that this approximation doesn't affect the final minimum but only the search procedure.

The sensitivity matrix **G** is defined as

$$\mathbf{G} = -\begin{bmatrix} \frac{\partial p_{c11}}{\partial k_1} & \cdots & \frac{\partial p_{c11}}{\partial k_N} & \frac{\partial p_{c11}}{\partial k_{s1}} & \cdots & \frac{\partial p_{c11}}{\partial k_{sN}} & \frac{\partial p_{c11}}{\partial r_{s1}} & \cdots & \frac{\partial p_{c11}}{\partial r_{sN}} \\ \frac{\partial T_{c11}}{\partial k_1} & \cdots & \frac{\partial T_{c11}}{\partial k_N} & \frac{\partial T_{c11}}{\partial k_{s1}} & \cdots & \frac{\partial T_{c11}}{\partial k_{sN}} & \frac{\partial T_{c11}}{\partial r_{s1}} & \cdots & \frac{\partial T_{c11}}{\partial r_{sN}} \\ & \cdots & & & \cdots & & & \cdots & \\ \frac{\partial T_{c1(N+1)}}{\partial k_1} & \cdots & \frac{\partial T_{c1(N+1)}}{\partial k_N} & \frac{\partial T_{c1(N+1)}}{\partial k_{s1}} & \cdots & \frac{\partial T_{c1(N+1)}}{\partial k_{sN}} & \frac{\partial T_{c1(N+1)}}{\partial r_{s1}} & \cdots & \frac{\partial T_{c1(N+1)}}{\partial r_{sN}} \\ & \cdots & & & \cdots & & & \cdots & \\ \frac{\partial p_{cM1}}{\partial k_1} & \cdots & \frac{\partial p_{cM1}}{\partial k_N} & \frac{\partial p_{cM1}}{\partial k_{s1}} & \cdots & \frac{\partial p_{cM1}}{\partial k_{sN}} & \frac{\partial p_{cM1}}{\partial r_{s1}} & \cdots & \frac{\partial p_{cM1}}{\partial r_{sN}} \\ \frac{\partial T_{cM1}}{\partial k_1} & \cdots & \frac{\partial T_{cM1}}{\partial k_N} & \frac{\partial T_{cM1}}{\partial k_{s1}} & \cdots & \frac{\partial T_{cM1}}{\partial k_{sN}} & \frac{\partial T_{cM1}}{\partial r_{s1}} & \cdots & \frac{\partial T_{cM1}}{\partial r_{sN}} \\ & \cdots & & & \cdots & & & \cdots & \\ \frac{\partial T_{cM(N+1)}}{\partial k_1} & \cdots & \frac{\partial T_{cM(N+1)}}{\partial k_N} & \frac{\partial T_{cM(N+1)}}{\partial k_{s1}} & \cdots & \frac{\partial T_{cM(N+1)}}{\partial k_{sN}} & \frac{\partial T_{cM(N+1)}}{\partial r_{s1}} & \cdots & \frac{\partial T_{cM(N+1)}}{\partial r_{sN}} \end{bmatrix}_{M(N+2)\times 3N}$$

.....4.17

Here the sensitivity matrix **G** is calculated by perturbation method. For instance, $\frac{\partial T_{c11}}{\partial k_1}$ can be calculated by perturbing k_1 and keeping other parameters constant. $\frac{\partial T_{c11}}{\partial k_1}$ can be approximated by

$$\frac{\partial T_{c11}}{\partial k_1} \cong \frac{T_{c11}\left(k_1 + \delta k_1, \cdots, k_N, k_{s1}, \cdots, k_{sN}, r_{s1}, \cdots, r_{sN}\right)}{\delta k_1} - \frac{T_{c11}\left(k_1, \cdots, k_N, k_{s1}, \cdots, k_{sN}, r_{s1}, \cdots, r_{sN}\right)}{\delta k_1} \qquad \text{.....4.18}$$

As it can be seen from Eq. **4.18**, each column of the sensitivity matrix needs one forward

simulation run. Since we have $3N$ parameters in total, $3N$ forward simulations need to be run to obtain the whole sensitivity matrix.

Now the Jacobian matrix can be written by

$$\mathbf{J} = \nabla \mathbf{e} = -\mathbf{C}_n^{-1/2}\mathbf{G} \quad \text{.....4.19}$$

Substitution of Eq. 4.19 into Eq. 4.12 results in

$$\delta \mathbf{x}_m = -\left(\mathbf{G}^{\mathrm{T}}\mathbf{C}_n^{-1}\mathbf{G} + \lambda \mathbf{I}\right)^{-1}\mathbf{G}^{\mathrm{T}}\mathbf{C}_n^{-1}\left(\mathbf{d} - \mathbf{g}(\mathbf{x})\right), \quad \text{.....4.20}$$

where the identity matrix has the dimension of $3N \times 3N$.

4.4 SOLUTION PROCEDURE FOR THE INVERSE MODEL

To do the nonlinear regression, the procedure is shown as follows.

1) With the initial guesses of the formation property values $\mathbf{x_m}$, calculate the corresponding pressure and temperature data $\mathbf{g}(\mathbf{x_m})$ using the forward simulator.

2) Calculate objective function value using $\mathbf{x}_\mathrm{m}$, $\mathbf{g}(\mathbf{x_m})$, $\mathbf{d}$, and $\mathbf{C_n}$.

$$\mathbf{f}(\mathbf{x}) = \frac{1}{2}\left\|\mathbf{d} - \mathbf{g}(\mathbf{x}_m)\right\|_2^2 = \frac{1}{2}\left(\mathbf{d} - \mathbf{g}(\mathbf{x}_m)\right)^T \mathbf{C}_n^{-1}\left(\mathbf{d} - \mathbf{g}(\mathbf{x}_m)\right)$$

3) Generate the sensitivity matrix **G** by perturbation method. In this case, we have six layer properties to be regressed, thus the sensitivity matrix has six columns. To generate the sensitivity matrix, we need to run the forward simulator six times by perturbing each of the layer property and generate one column every time.

4) Calculate the Hessian matrix **H** by

$$\mathbf{H} = \mathbf{G}^{\mathrm{T}}\mathbf{C}_n^{-1}\mathbf{G}$$

5) Calculate the derivative vector **w** by

$$\mathbf{w} = \mathbf{G}^{\mathrm{T}}\mathbf{C}_n^{-1}\left(\mathbf{d} - \mathbf{g}(\mathbf{x}_m)\right)$$

6) Calculate the upgrade vector $\delta \mathbf{x}_m$ by

$$\delta \mathbf{x}_m = -\left(\mathbf{H} + \lambda \mathbf{I}\right)^{-1}\mathbf{w}$$

where the initial value of λ is set to be 1.

7) Update the property vector by

$$\mathbf{x}_{m+1} = \mathbf{x}_m + \delta \mathbf{x}_m$$

8) Calculate objective function value with the updated property vector.

$$\mathbf{f}(\mathbf{x}) = \frac{1}{2}\left\|\mathbf{d} - \mathbf{g}(\mathbf{x}_{m+1})\right\|_2^2 = \frac{1}{2}\left(\mathbf{d} - \mathbf{g}(\mathbf{x}_{m+1})\right)^T \mathbf{C}_n^{-1}\left(\mathbf{d} - \mathbf{g}(\mathbf{x}_{m+1})\right)$$

Denote the objective function to be $\mathbf{f}(\mathbf{x})_N$ that is calculated using $\lambda = 1$.

9) Determine the optimum value of the damping factor λ. First of all, change the damping factor λ to be $M\lambda$ and λ/M respectively, where M is a given constant number. Calculate the new property vectors $\mathbf{x}_{m+1}(M\lambda)$, $\mathbf{x}_{m+1}(\lambda/M)$ and corresponding objective function values $\mathbf{f}(\mathbf{x})_{Up}$ and $\mathbf{f}(\mathbf{x})_{Down}$. Comparing $\mathbf{f}(\mathbf{x})_N$, $\mathbf{f}(\mathbf{x})_{Up}$ and $\mathbf{f}(\mathbf{x})_{Down}$, if $\mathbf{f}(\mathbf{x})_{Up} < \mathbf{f}(\mathbf{x})_{Down}$ and $\mathbf{f}(\mathbf{x})_{Up} < \mathbf{f}(\mathbf{x})_N$, then update λ to be $M\lambda$; if $\mathbf{f}(\mathbf{x})_{Down} < \mathbf{f}(\mathbf{x})_{Up}$ and $\mathbf{f}(\mathbf{x})_{Down} < \mathbf{f}(\mathbf{x})_N$, then update λ to be λ/M; otherwise keep the original λ value.

10) Regenerate the upgrade vector $\delta\mathbf{x}_m$ by using the optimum damping factor and calculate the objective function value. The property vector now is updated to be $\mathbf{x}_{m+1} = \mathbf{x}_m + \delta\mathbf{x}_m$. Then go to the next regression step.

4.5 PROPOSED TEST AND ANALYSIS PROCEDURE

The working principle of the new testing method is to measure the wellbore pressure and temperature at the bottom of the reservoir and temperature at the top of each productive layer during the transient flow period. The transient downhole pressure is measured by a downhole pressure gauge and is used to reveal the behavior of the total system, while transient temperature is recorded by multipoint temperature sensors and is used to reveal the behavior of individual producing intervals. The general testing scheme is shown in **Fig. 4.1**. The test uses a combination of a downhole pressure gauge and multiple downhole temperature sensors.

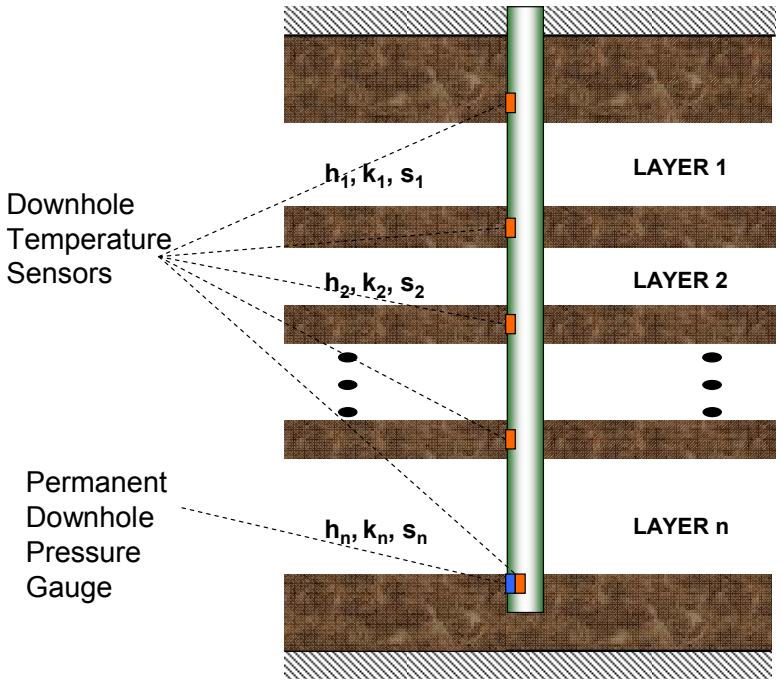

Fig. 4.1 Data acquisition configuration

For the new multilayer test method, only one surface rate change operation is required to induce a transient flow period. Considering that most production wells are usually producing at maximum rate, the transient flow period should be induced by decreasing the surface flow rate by half or one third. However, from a theoretical point of view, either a flow rate increase or decrease can achieve the same objective.

Additionally, the Horner's approximation method (Horner, 1967) instead of superposition is used to model the production history. Assuming the test equipments have been installed before the transient test, recording of temperature and pressure data should start while the well is in a stabilized flow condition. Then the surface rate should be stepped up or down to a new flow rate while transient pressure and temperature data are acquired in the positions shown in **Fig. 4.1**.

After collecting the measurement data, a series of data points with logarithmic time spacing are selected for regression. Given some arbitrary initial guesses, the Levenberg-Marquardt regression is applied to find out the formation property values. The general workflow of the proposed test and analysis are summarized as follows,

1) Conduct a transient flow test and collect transient temperature and pressure data at required stations as observed data points;
2) Input the observed pressure and temperature data into the inverse simulator;
3) Given some arbitrary guesses of the formation properties (k, k_s, and r_s);
4) Run the inverse simulator to do nonlinear regression until the optimum solutions are found out;
5) The optimum solutions are believed to be the formation properties we are looking for.

More details about setting test stations and data selection can be found in Section 5.

5 RESULTS AND DISCUSSION

5.1 INTRODUCTION

A coupled wellbore/reservoir semi-transient thermal simulator has been developed using C code to implement the mathematical model presented in Sections 2 and 3. Also, the inverse model has been incorporated into the simulator for regression. In this section, we discuss the forward and inverse simulation results. First, feasibility studies of model application are performed to examine the effect on transient temperature behavior of changing formation properties. Second, a hypothetical example is presented to illustrate how to predict multilayer formation properties using the proposed testing and analysis approach. The second example is presented to show how this interpretation technique can be applied for low productivity diagnosis. Some practical implications are considered including temperature resolution and data noise impact, possible improvements by data filtering, and data rate impact on interpretation results.

5.2 FEASIBILITY OF MODEL APPLICATION

The objective of this section is to demonstrate that transient temperature and pressure behavior is sensitive to layer permeability and skin values. Since the bottomhole pressure can only reveal the behavior of the total system and transient temperature at multiple locations are sensitive to individual layer performance, the sensitivity study will focus on the transient temperature instead of pressure. However, transient pressure is required for inversing formation properties.

In this section, the developed forward model has been applied to several hypothetical cases to study the transient temperature sensitivities on damage radius, damage permeability, and formation permeability. The input fluid and formation parameters used in this section are shown in **Table 5.1** unless otherwise specified.

Table 5.1 Reservoir and fluid properties for synthetic examples

Initial reservoir pressure at reference depth (psi)	5920
Formation surface temperature (°C)	15
Geothermal gradient (°C/m)	0.018
Reference depth (m)	3550
Wellbore radius, (ft)	0.27
Porosity	0.2
Total system compressibility (psi^{-1})	1.9e-5

5.2.1 The Relationship of the Transient Temperature and Layer Skin Factors

According to the forward model studies, skin factor will affect transient wellbore temperature in two different ways. For the formation side, the skin factor will results in a larger pressure gradient within the damage region and further causes a larger temperature increase compared with a non-damage case. For the wellbore side, different individual layer skin factor will lead to distinct individual layer flow rate transient behavior, which will affect wellbore fluid temperature by the mixing process. Here, we will investigate the skin effect by using three cases that represent simple and complicated situations. The three cases are a one-layer, a two-layer, and a three-layer case respectively.

First, a single-layer reservoir is used to examine the effect of skin factor on transient temperature. Assuming the productive interval is 50 m thick and the skin factor is 10, the reservoir diagram is shown in **Fig. 5.1**. The oil well has been producing at 1200 STB/d up to 100 hrs. **Fig. 5.2** shows the transient reservoir temperature behavior at depth of 3525m (within the productive interval) during the test. From **Fig. 5.2**, we can see that there is a larger temperature gradient and the gradient increases with respect to time. Compared with the no-skin case (**Fig. 5.3**), we can see a distinct temperature increase caused by the damage region.

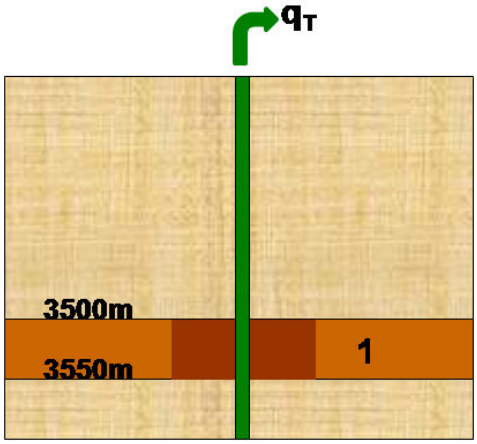

Fig. 5.1 Reservoir diagram for the study of skin factor (single-layer case)

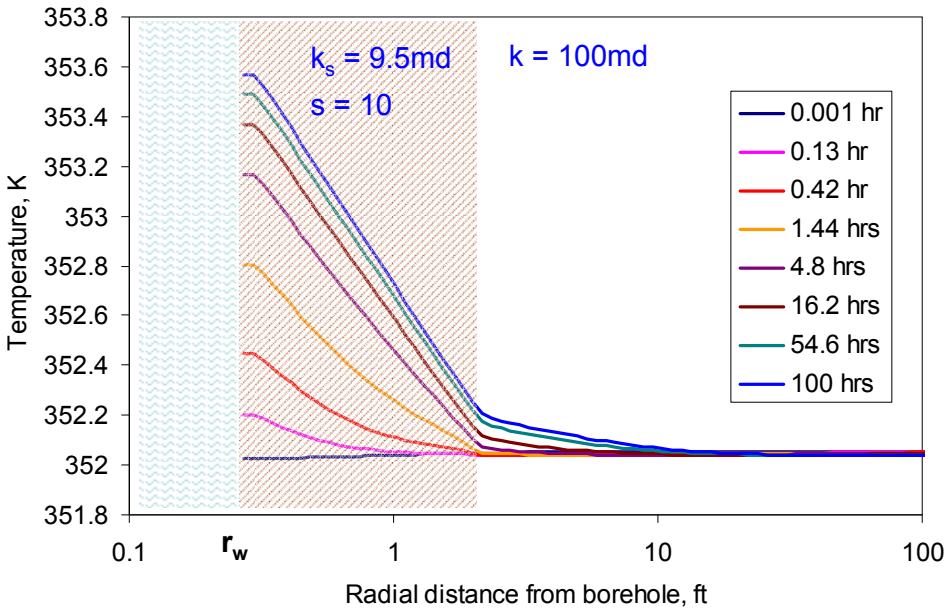

Fig. 5.2 Reservoir temperature variations during test for one-layer case

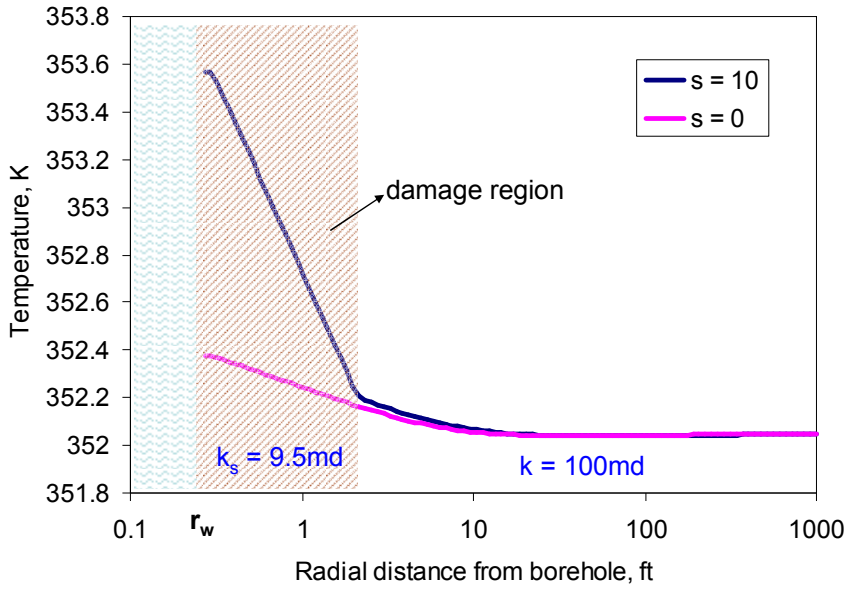

Fig. 5.3 Reservoir temperature at the middle of the reservoir depth (t = 100 hrs)

Then a two-layer reservoir case is studied to investigate the skin effect in commingled multilayer reservoirs. The reservoir diagram is shown in **Fig. 5.4**, and the test scheme is shown in **Fig. 5.5**. To induce a transient flow period, the surface flow rate is increased to 8000 STB/d from 4000 STB/d for 100 hrs. To understand the skin effect in multilayer reservoir, four different scenarios are considered and listed in **Table 5.2**.

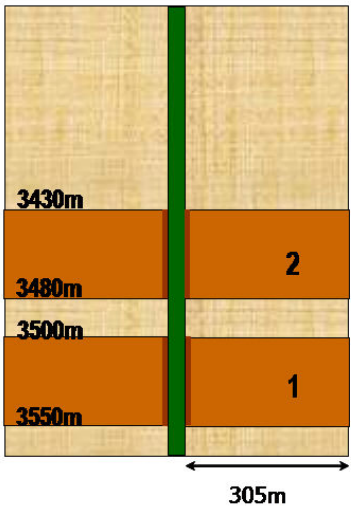

Fig. 5.4 Reservoir diagram for the study of skin factor (two-layer case)

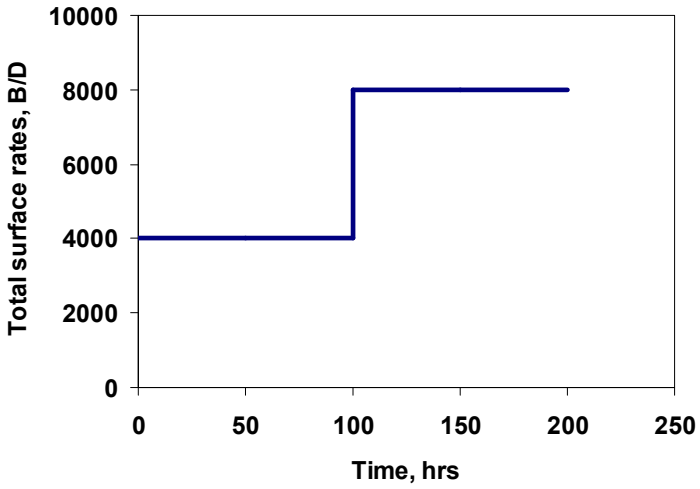

Fig. 5.5 Test scheme for the two-layer case

Table 5.2 Damage scenarios for the two-layer case

Layer No.	Case 1 (s)	Case 2 (s)	Case 3 (s)	Case 4 (s)
1	0	0	10	10
2	0	10	0	10

The flowing pressure behaviors for different damage scenarios are shown in **Fig. 5.6**, which indicates that the flowing pressure is only sensitive to the total skin factor, but they cannot tell the location of skin. However, the normalized layer flow rate changes are sensitive to the location of skin, which is shown in **Fig. 5.7**. Here the normalized layer flow rate change is used to measure the fraction of layer flow rate changes and it is defined as follows.

$$d\hat{q}_j = \frac{\Delta q_j(\Delta t)}{\sum_{j=1}^{N} \Delta q_j(\Delta t)} \quad \text{..... 5.1}$$

where layer flow-rate difference is defined as

$$\Delta q_j(\Delta t) = \left| q_j(\Delta t) - q_j(t_1) \right| \quad \text{..... 5.2}$$

The transient flow test just before t_1, and Δt means the elapsed time after rate change. Furthermore, by calculating the formation temperature change distribution during the test (**Fig. 5.8**), we can see that the transient temperature is sensitive to individual layer skin factor and even the damage radius which will be discussed later.

The transient temperature profiles of the second scenario are shown in **Fig. 5.9**. From **Fig. 5.9**, we can see that the temperature change over the upper producing interval is larger than that in the bottom layer due to the skin effect. The positive skin in the upper layer results in a higher entering fluid temperature and a smaller layer flow rate, which will lead to a relatively higher final wellbore fluid temperature.

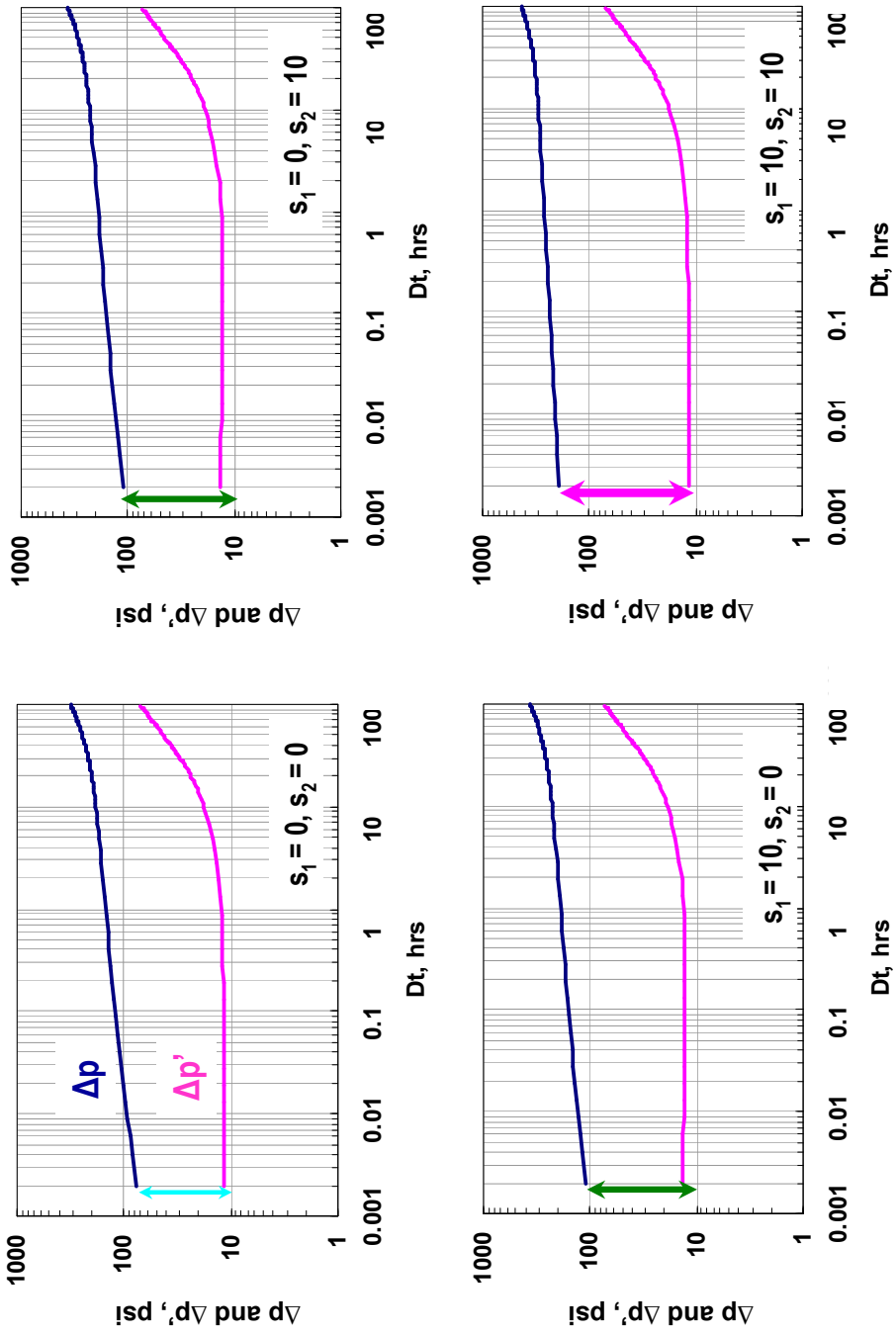

Fig. 5.6 Flowing pressure for different damage scenarios for the two-layer case

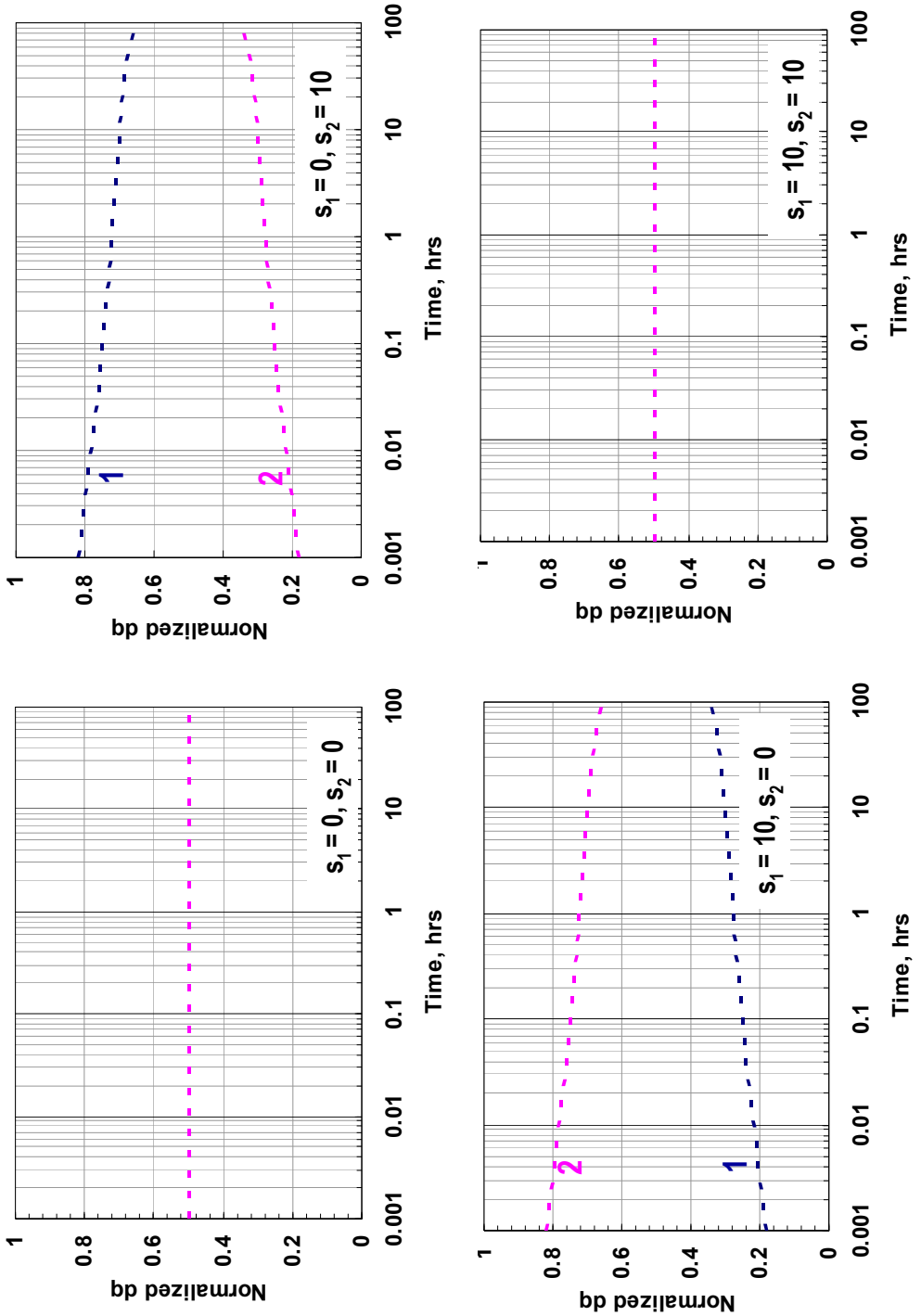

Fig. 5.7 Normalized layer flow rate changes for the two-layer case

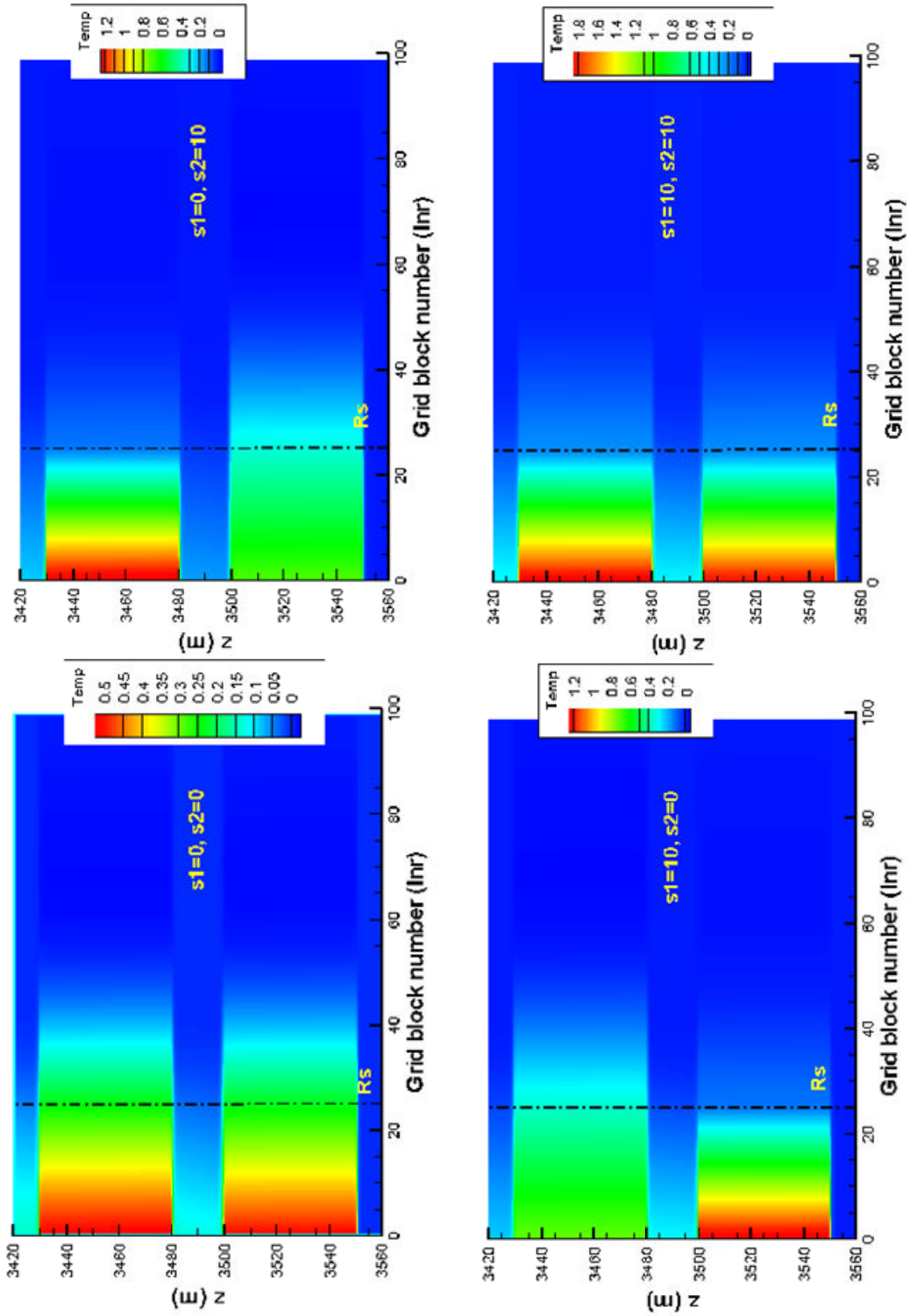

Fig. 5.8 Formation temperature change distribution at the end of test for the two-layer case

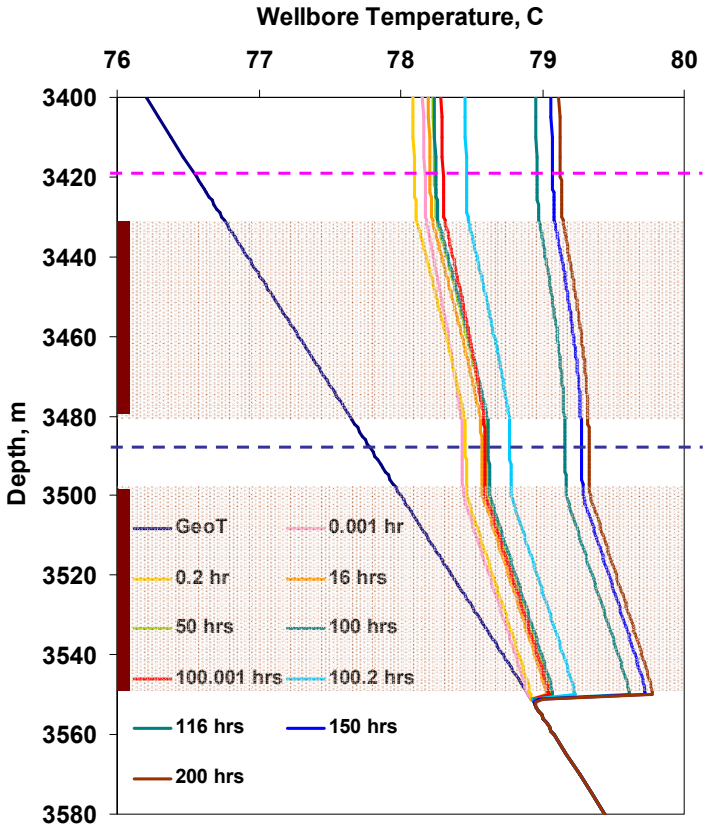

Fig. 5.9 Wellbore temperature profiles ($s_1 = 0$, $s_2 = 10$)

In the end, a more complicated three-layer reservoir case is presented. The reservoir diagram is shown in **Fig. 5.10**. To induce a transient flow period, the surface flow rate is cut back to 4000 STB/d from 8000 STB/d for 24 hrs. The layer properties are given in **Table 5.3**. In this commingled three-layer reservoir, the same permeability values are assigned to all layers to eliminate the permeability effect, and the wellbore storage coefficient is 0.01 bbl/psi. The upper layer (Layer 1) has a skin factor of 10, the middle layer (Layer 2) has a skin factor of 3, and the skin factor for the bottom layer (Layer 3) is zero.

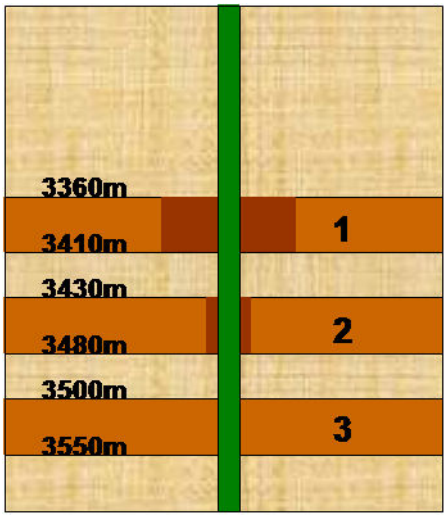

Fig. 5.10 Reservoir diagram for the study of skin factor (three-layer case)

Table 5.3 Damage scenarios for the three-layer case

Case 2	k (md)	k_s (md)	r_s (ft)	s
Layer 1	30	4.3	1.42	10
Layer 2	30	4.3	0.44	3
Layer 3	30	-	-	0

The transient temperature profiles during the test (**Fig. 5.11**) are shift to lower temperatures from the start of the test. However, the temperature shifts at different locations are not uniform. For this three-layer reservoir, temperature data at four different stations (3550m, 3490m, 3420m, and 3350m) are required for analysis, and the temperature versus time response in **Fig. 5.12** shows parallel temperatures decreases at 3550m and 3490m, and parallel temperature decreases at 3420m and 3350m that are steeper during the early-time period. At about $\Delta t = 2$ hrs and $\Delta t = 7$ hrs, the temperature at 3420m and 3350m respectively became parallel to the other two temperature curves. Section 5.2.2 will relate this behavior to the magnitude of the damage radius. In this case, Layer 1 has the deepest damage; thereby it takes the longer time for the temperature at 3350m to become parallel to other temperature curves. This example indicates that the damage radius is critical information for transient temperature simulations.

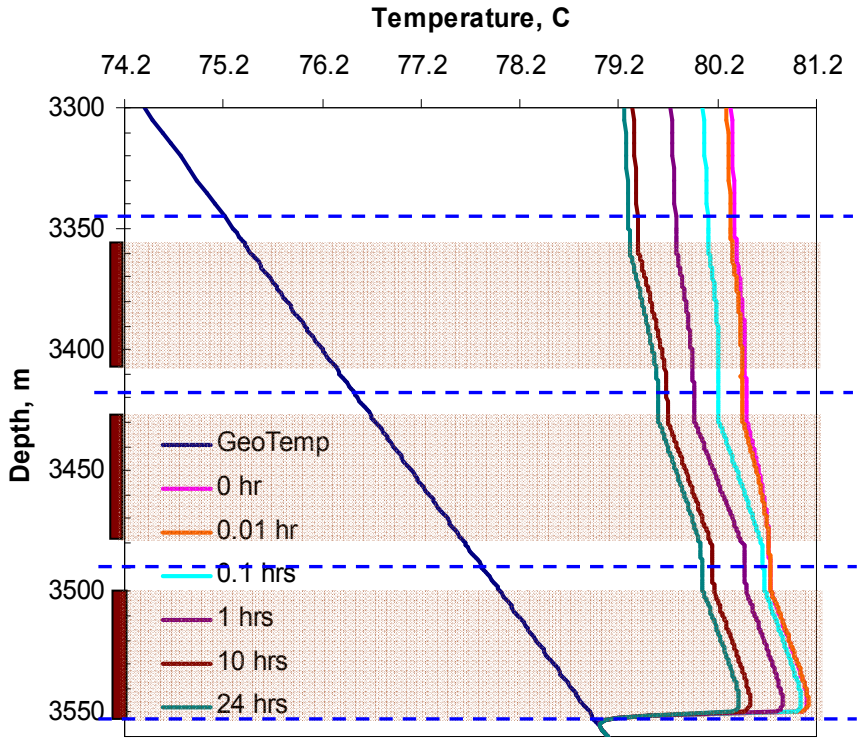

Fig. 5.11 Transient temperature profile during test for the study of skin factor

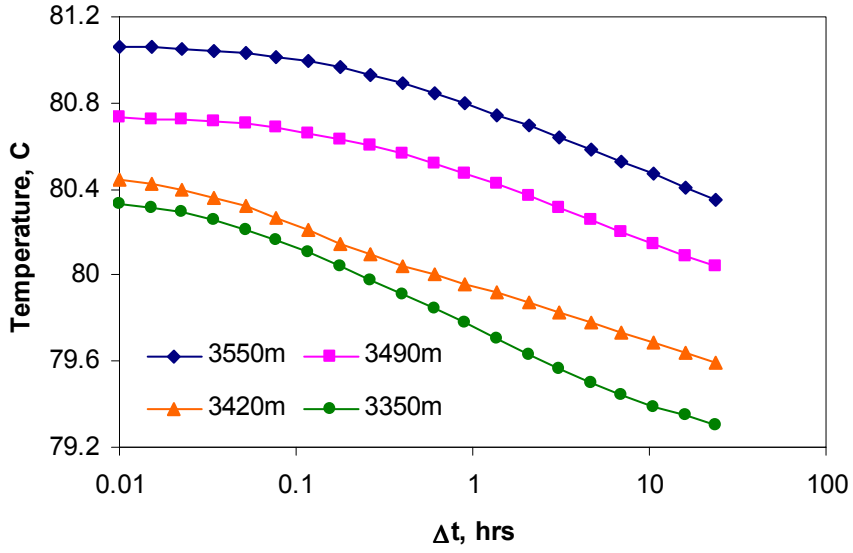

Fig. 5.12 Semi-log temperature history profiles during test for the study of skin factor

The transient reservoir temperature change profiles are shown in **Fig. 5.13** as the formation temperature change ($\Delta T(r) = T(r) - T_{ST}(r)$) at the end of test. It can be seen that Layer 1 has the largest near well temperature gradient during the test, and the temperature gradient in Layer 3 is the smallest. Additionally, we can see that the temperature gradients in Layer 1 and 2 mostly happen within the damage regions. From the simulated reservoir pressure change distribution ($\Delta p(r) = p(r) - p_{ST}(r)$) at the end of test (**Fig. 5.14**), we see that the layer pressure changes are consistent with the reservoir temperature changes, thus verifying previous comments that the formation temperature changes mostly depend on the pressure changes.

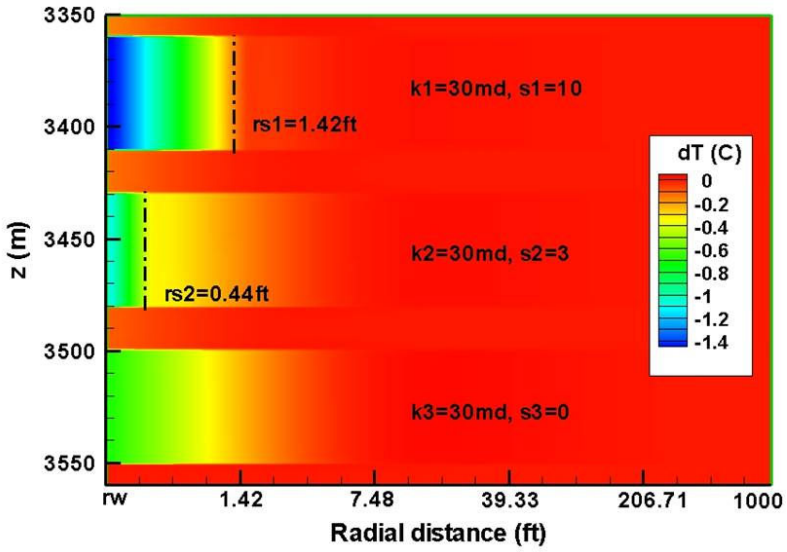

Fig. 5.13 Formation temperature variations at the end of test

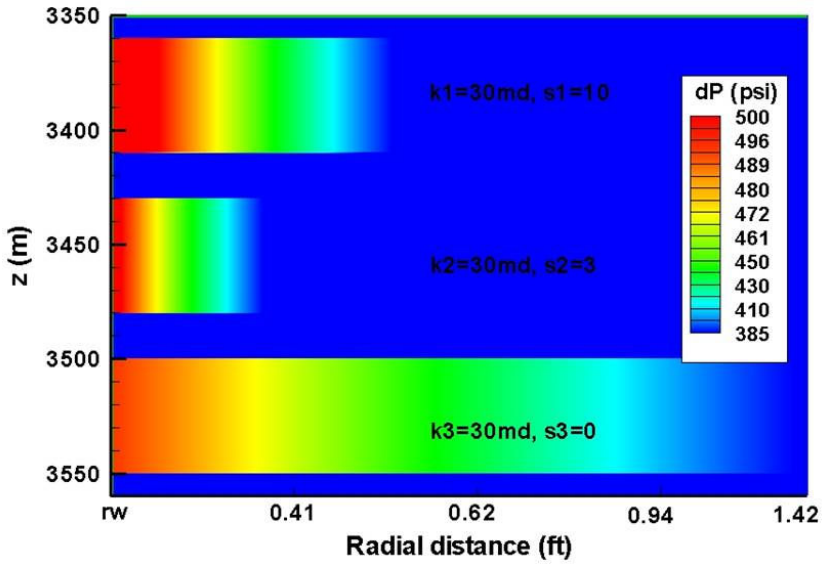

Fig. 5.14 Reservoir pressure change at the end of test for the study of skin factor

Besides the sandface formation fluid temperature, the final wellbore fluid temperature also depends on wellbore mixing process. For this case, the normalized layer flow rate changes during the test have been calculated and shown in **Fig. 5.15**. With a decreased surface flow rate, this case shows more complicated situation than the preceding two-layer case. On one hand, Layer 1 has a smaller layer flow rate before and after the surface flow rate change, which leads to a smaller wellbore fluid temperature change over Layer 1 in vertical direction (**Fig. 5.11**); on the other hand, Layer 1 has a larger temperature decrease in temporal direction (**Fig. 5.11**) due to a larger temperature decrease of entering formation fluids (**Fig. 5.13**).

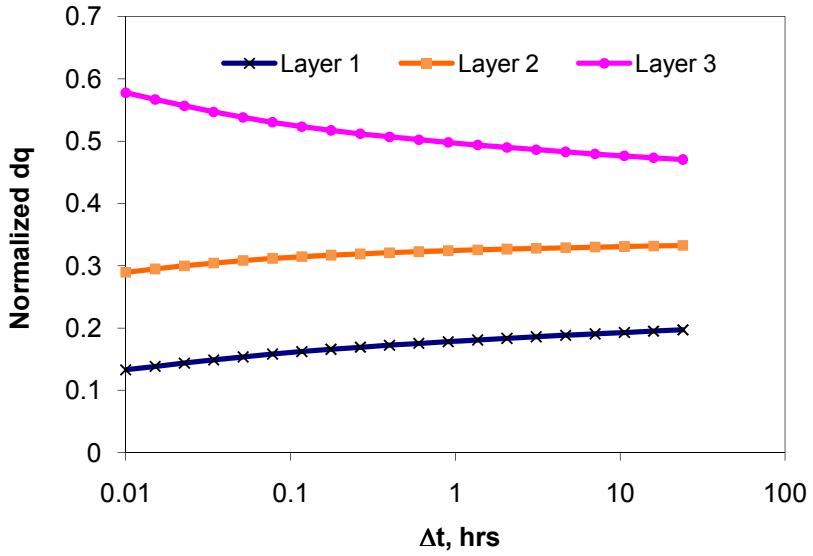

Fig. 5.15 Layer flow rate during test

5.2.2 The Relationship of the Transient Temperature and the Damage Radius

One of the most significant results from this work is the discovery of the relationship between the transient temperature behavior and the damage radius and permeability. The effect of the damage radius and permeability on transient temperature results from the altered reservoir pressure gradient in the damage zone. The wellbore fluid temperature depends on the entering formation fluid temperature, while the formation fluid temperature is directly related to the reservoir pressure gradient. For the layers with non-negligible skin factors, there exists a larger pressure gradient in the damage zone. During the early-time transient flow period, the reservoir pressure variations within the damage zone are also larger than other producing intervals, which will affect the transient heat transfer in the formation.

The sensitivity of the transient temperature on damage radius has been studied using the following hypothetical case. The synthetic commingled reservoir shown in **Fig. 5.16** has two layers and the upper layer has a skin factor. The reservoir properties are given in **Table 5.4**. To study the effects of different damage radius, four different combinations of damage radius and permeability that result in the same Hawkin skin

values are adopted to cover a wide range of damage scenarios. To induce a transient flow period, the surface flow rate is cut back to 4000 STB/d from 8000 STB/d for 24 hrs. For simplicity, we assume the wellbore storage coefficient to be zero in this case.

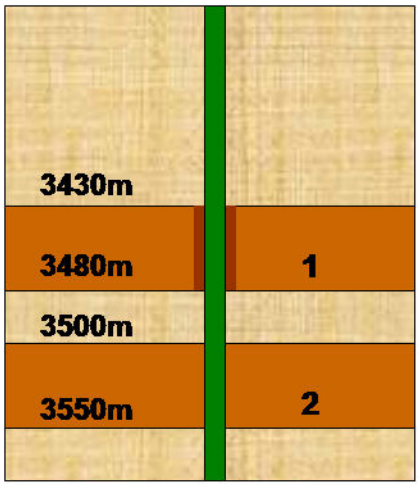

Fig. 5.16 Reservoir diagram for the study of damage radius

Table 5.4 Layer properties for studying the effect of damage radius

Case 1	k (md)	k_s (md)	r_s	s
Layer 1	30	0.7	1 in	10
	30	1.4	2 in	10
	30	4.1	1 ft	10
	30	5.3	2 ft	10
Layer 2	30	-	-	0

Transient temperature profiles output by the model for the case with $r_s = 1$ ft are shown in **Fig. 5.17**. The temperature profile versus depth just before the step rate change is decreasing for decreasing depth across from the deeper interval (layer 2). However, because of the skin, the fluid entering the wellbore at the bottom of the shallower interval (layer 1) is at a higher temperature and increases with decreasing depth across that interval. Above both intervals, the temperature decreases with decreasing depth as heat is lost by conduction to the overburden.

Because the surface rate was decreased, the temperature profiles shift to lower temperatures with increasing time except for the profile at 0.01 hr, which shows warming in layer 1 caused by the fluid compression heating due to the reservoir pressure increase.

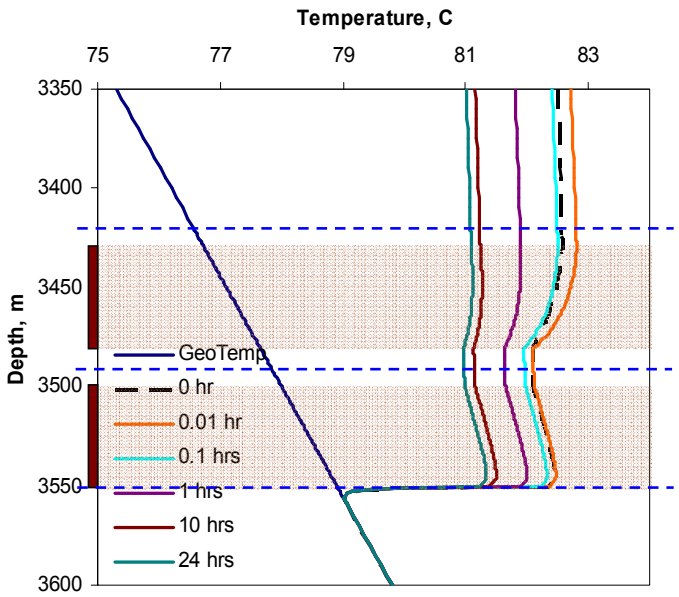

Fig. 5.17 Transient temperature profile during test (rs = 1ft)

Only temperature data at the bottom and above each productive layer are required to determine individual layer properties. For this case, the temperature measurement stations are 3550m, 3490m, and 3420m. For different damage radius, the temperature behavior versus time for each of the two layers is shown in **Fig. 5.18**. From **Fig. 5.18**, we can see that for different damage radius, the wellbore temperature at 3550m and 3490m are always the same, and only the temperature at 3420m varies differently, which is because the positive skin is in the top layer. Only the temperature at 3420m is sensitive to the effects of formation damage. **Fig. 5.18** also indicates that for different damage radius, the transient temperature responses are different. Although the four temperature curves approach the same temperature value at the end of test, their behavior versus time is distinct.

The variation characteristics for different damage radius are enhanced by plotting the derivative of temperature with respect to the elapsed time as shown in **Fig. 5.19**. **Fig. 5.19** shows that for different damage radius, the peak of the temperature derivative curves appears at different time points, clearly showing the sensitivity of the transient temperature response to the damage radius.

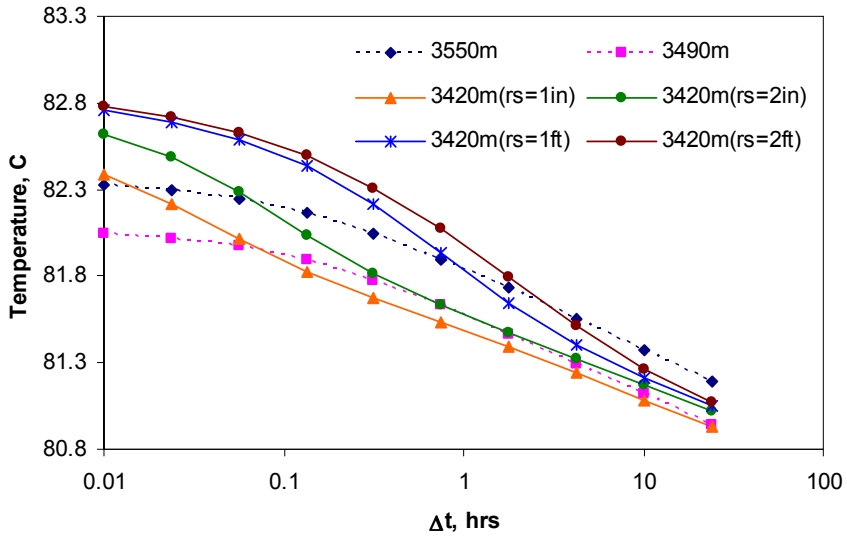

Fig. 5.18 Temperature history profiles for different damage radius

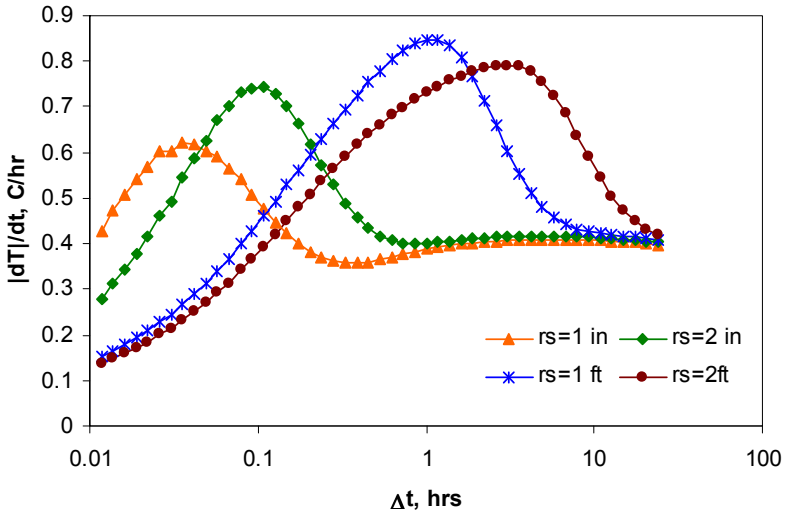

Fig. 5.19 Temperature derivative behavior for different damage radius

During the 24-hr test, the reservoir temperature profile can be simulated at each time step using the forward simulator. Using the initial temperature field right before test, we can compute the temperature change $\Delta T(r) = T(r) - T_{ST}(r)$ versus radial distance, where the subscript 'ST' means 'at the start of test'. Again for the damage radius of 1 ft, the transient temperature change in Layer 1 (3470 m) is shown in **Fig. 5.20**. **Fig. 5.20** shows that the early-time temperature changes only occur in the damage region because the larger pressure gradient within the damage zone leads to a larger temperature gradient, and the larger temperature variation needed a longer time to establish the local thermal equilibrium compared with Layer 2. Once the local thermal equilibrium is established, the heat transfer begins to pass beyond the damage region and extend to the further formation. From fff, we can see the turning point seems to occur after 1.4 hrs which corresponds with the time when the temperature curve at 3420m becomes parallel to the temperature at 3490m and 3550m in **Fig. 5.18**.

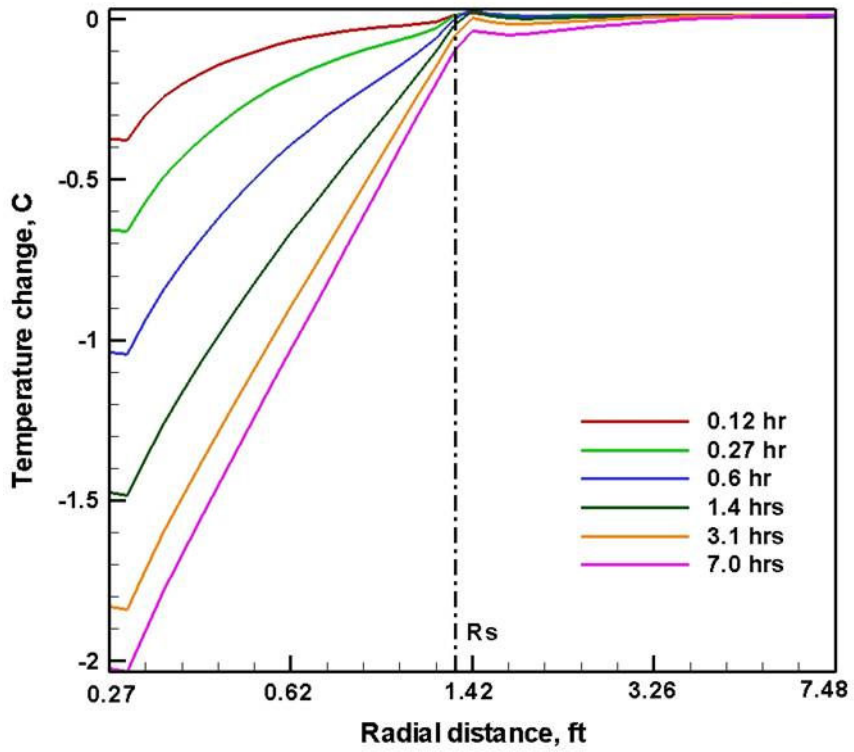

Fig. 5.20 Transient temperature change profile during test (3470m)

Additionally, this case indicates the damage radius effects can be seen by transient temperature but not transient pressure, which is because pressure propagation in the formation is much faster than temperature propagation. The damage radius effects will disappear in very early time so that cannot be observed in the test.

5.2.3 The Relationship of the Transient Temperature and Permeability

Here the same principles will be used to study the sensitivity of transient temperature to layer permeabilities. The reservoir diagram is shown in **Fig. 5.21**. The layer properties are listed in **Table 5.5**. The upper layer (Layer 1) has the highest permeability of 40md, and the middle layer (Layer 2) has the lowest permeability of 5md. All of the productive layers have a zero skin factor. To induce a transient flow period, the surface flow rate is cut back to 4000 STB/d from 8000 STB/d for 24 hrs. For simplicity, we assume the wellbore storage coefficient to be zero in this case.

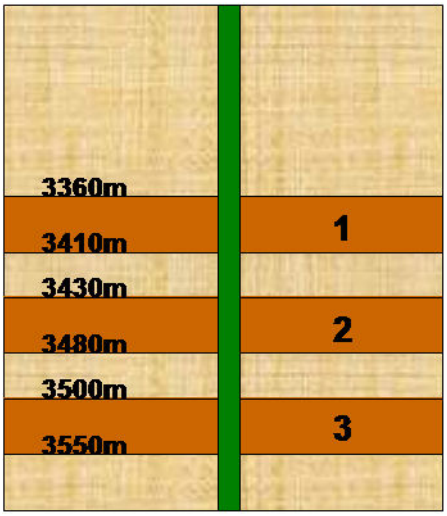

Fig. 5.21 Reservoir diagram for the study of permeability

Table 5.5 Layer properties for studying the effect of permeability

Case 3	k (md)	s
Layer 1	40	0
Layer 2	5	0
Layer 3	20	0

The transient temperature profiles during the test are shown in **Fig. 5.22**. We can see that the wellbore temperature profiles shift much more uniformly when there are no major contrasts in the layer skin factors, and **Fig. 5.23** also shows parallel behavior in temperature versus time at the various measurement depths.

The synchronous temperature changes can be understood by observing the formation fluid temperature change profiles in **Fig. 5.24**. Since the formation fluid temperature change mainly depends on the reservoir pressure change and the reservoir pressure change profile (**Fig. 5.25**) in each layer is very similar during the early-time transient period, similar temperature change profiles are observed in each of the layers. Additionally, from the transient temperature behavior in the formation at 3400 m (**Fig. 5.26**), we see no sudden temperature changes in the producing layer, and thus the temperature curves in **Fig. 5.23** are parallel to each other.

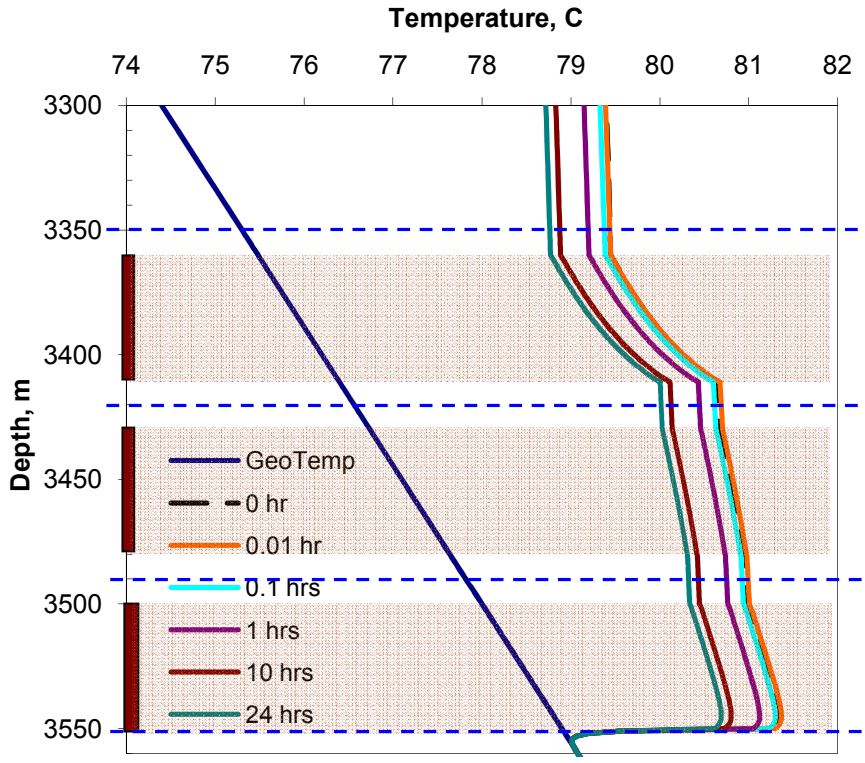

Fig. 5.22 Transient temperature profile during test for the study of permeability

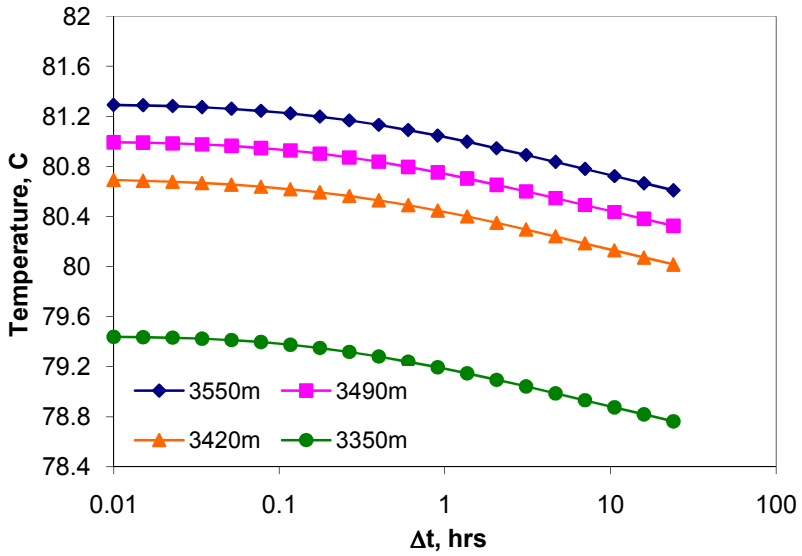

Fig. 5.23 Semi-log temperature history profiles during test for the study of permeability

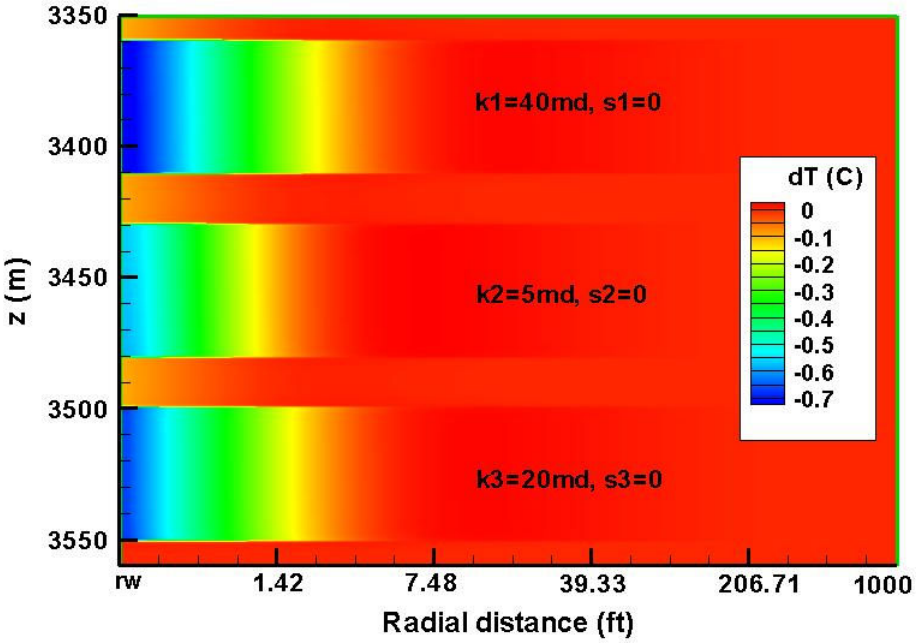

Fig. 5.24 Formation temperature variations at the end of test (ΔT2)

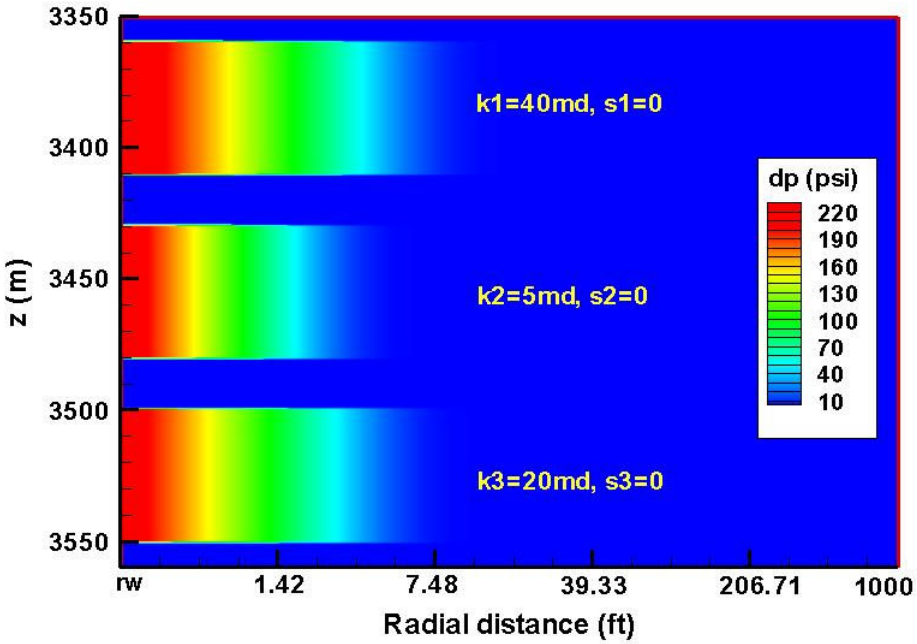

Fig. 5.25 Reservoir pressure change at the end of test for the study of permeability

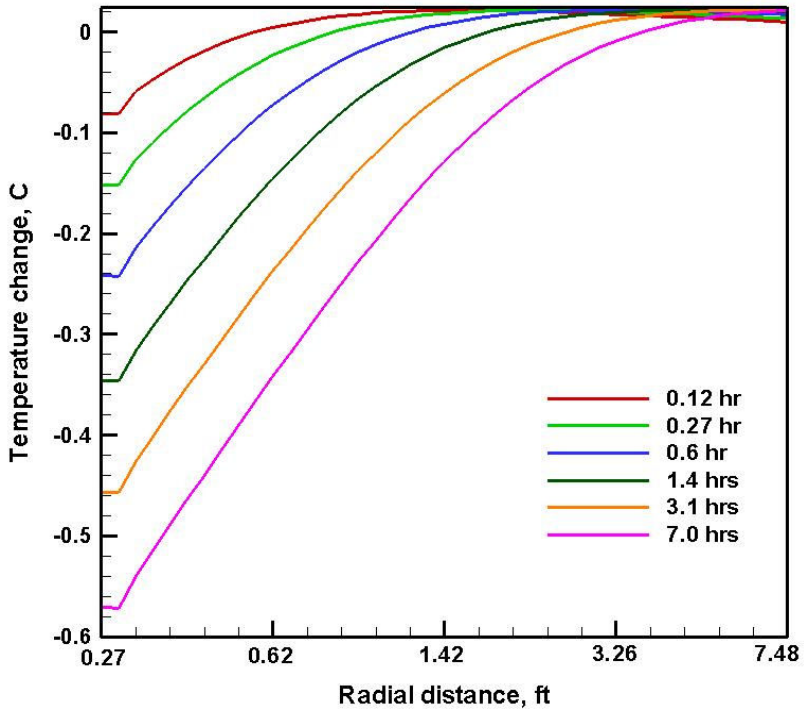

Fig. 5.26 Transient formation temperature profiles during test

Although the layer permeability difference did not lead to any signature in the formation temperature variations, it has a great impact on wellbore mixing procedure. From the simulated layer flow rates shown in **Fig. 5.27**, we see that Layer 1 has the highest flow rate, which pulled the wellbore temperature toward the geothermal temperature and yielded a relatively low wellbore mixture temperature; while Layer 2 is producing the least formation fluids, the wellbore temperature does not have much variation over Layer 2.

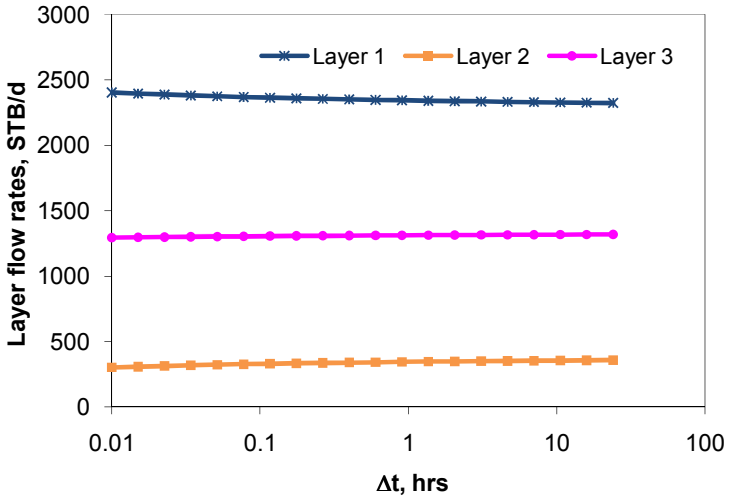

Fig. 5.27 Layer flow rate variations during test

5.3 A HYPOTHETICAL EXAMPLE FOR PREDICTING FORMATION PROPERTIES

Here a synthetic case is designed to show how to predict multilayer formation properties using the proposed testing and analysis approach. Theoretically, our model can be applied for arbitrary number of productive zones, and a four-layer case is used here for illustration.

Assume we have a four-layer commingled reservoir with different permeability and skin, where the skin is caused by formation damage. Thereby the damage permeability and damage radius are defined separately and are considered as independent variables in the inverse model. A 24-hr transient test is induced by cutting

back the surface flow rate from 8000 STB/d to 4000 STB/d. The wellbore storage coefficient is 0.1 bbl/psi. The layer properties are listed in **Table 5.6**. The reservoir diagram is shown in **Fig. 5.28**.

Table 5.6 Layer properties for the four-layer case

	k (md)	k_s (md)	r_s (ft)	s
Layer 1	100	10.1	1.45	15
Layer 2	40	14.8	0.88	2
Layer 3	200	23.6	1.04	10
Layer 4	300	27.4	0.45	5

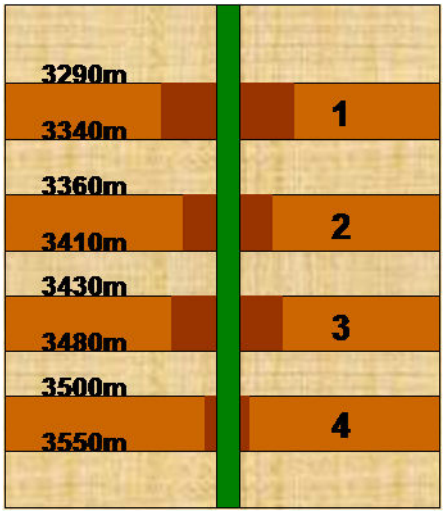

Fig. 5.28 Reservoir diagram for the hypothetical example

First, the pressure and temperature at stations should be recorded right before the surface flow rate change. Then, during the 24 hr-test, the pressure and temperature at required locations are measured at different time points. For the hypothetical case, the temperature distribution along the well during the test (**Fig. 5.29**) and the pressure at the bottom (**Fig. 5.30**) were simulated using the forward simulator. From the log-log pressure and derivative curves (**Fig. 5.30**), we can identify the existence of the wellbore storage effect. To apply the new testing approach, only the temperature values at specific

locations are required. In this case, temperature data at the bottom (3550m) of the reservoir and the temperature data at the top of each layer (3490m, 3420m, 3350m, and 3280m) are required for interpretation. The temperature histories at these depths during the test can be seen in **Fig. 5.31**. To accelerate the speed of regression convergence, logarithmic time steps are used to select the pressure and temperature data to be matched with the model. For this 24-hr test, measurements at six time points were sufficient for the regression. During the 24-hr test, the selected pressure and temperature measurement data at required time points are shown in **Fig. 5.32** and **Fig. 5.33**.

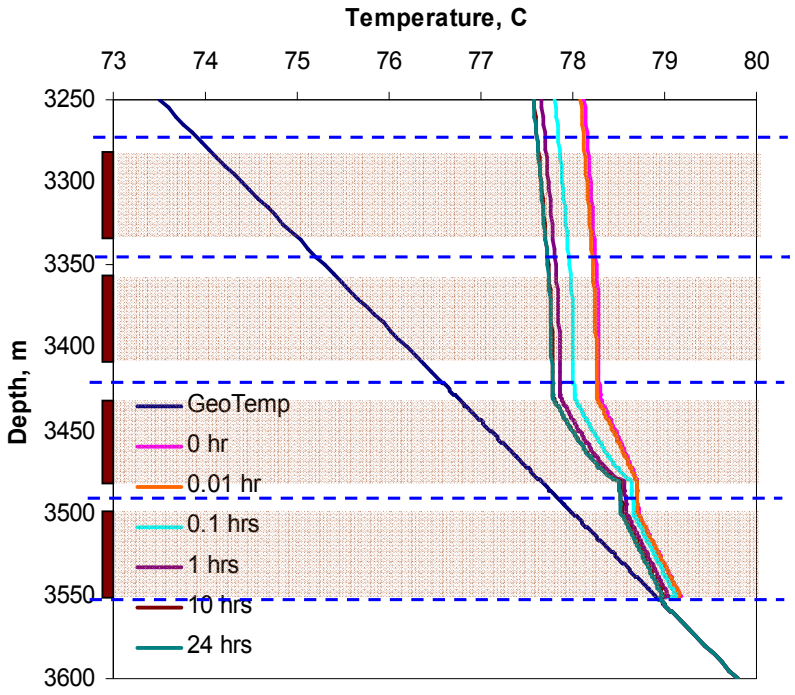

Fig. 5.29 Transient temperature profile during test for the hypothetical example

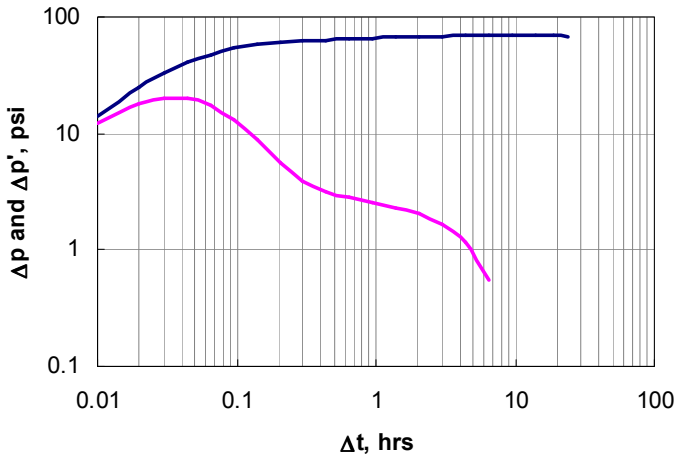

Fig. 5.30 Log-log pressure change and derivative during test for the hypothetical example

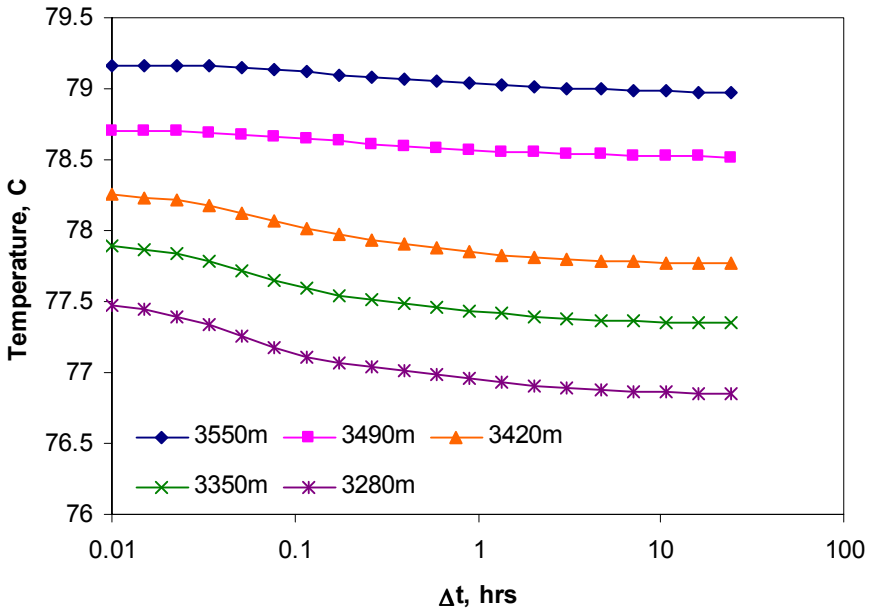

Fig. 5.31 Semi-log temperature history profiles during test for the hypothetical example

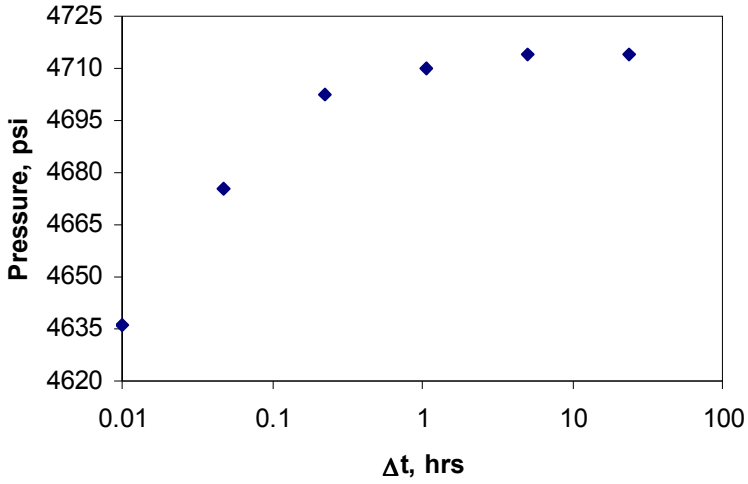

Fig. 5.32 Measured pressure data in four-layer case

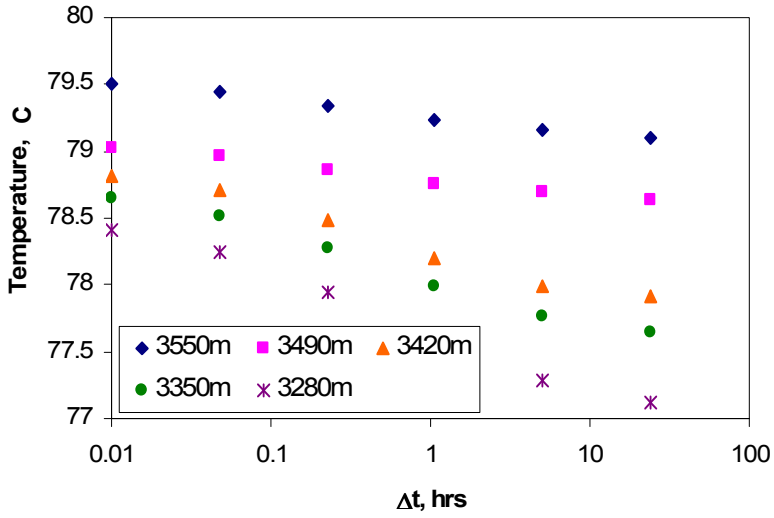

Fig. 5.33 Measured temperature data in four-layer case

Given some arbitrary initial guesses of formation properties, the inverse simulator can obtain the regression results after several iteration steps. The regression results are shown in Table 5.7. We can see that regression results are very close to the true values. All the regression parameters (permeability, damage permeability, damage

radius, and skin) have been determined to very high accuracies. The regression results also indicate that the wellbore storage effect did not impact the interpretation. Thus we can say that the inversion method performs very well for the complicated reservoir situation.

Table 5.7 True values, initial guesses, and regression results for the four-layer case

	True values				Initial guesses				Regression results			
	k (md)	k_s (md)	r_s (ft)	s	k (md)	k_s (md)	r_s (ft)	s	k (md)	k_s (md)	r_s (ft)	s
Layer 1	100	10.1	1.45	15	150	14.2	0.63	8	100.03	10.1	1.45	15.002
Layer 2	40	14.8	0.88	2	150	14.2	0.63	8	40.00	14.8	0.88	2.000
Layer 3	200	23.6	1.04	10	150	14.2	0.63	8	199.97	23.7	1.04	9.996
Layer 4	300	27.4	0.45	5	150	14.2	0.63	8	299.96	27.5	0.45	4.992

5.4 APPLICATION EXAMPLE–LOW PRODUCTIVITY DIAGNOSIS

The example in this section shows that the new proposed testing method can be used for low productivity diagnosis. Assume we have an oil well producing in a three-layer commingled reservoir and the reservoir diagram is shown in **Fig. 5.34**. If reservoir production log profile were acquired in this well, we would find the second layer is only producing about ten percent of the total flow rate. The reason of the low production rate in this layer could be caused by the formation damage or the low layer permeability, but this cannot be determined from one production log. In Case (a) the middle layer has a skin factor of 10; in Case (b), the middle layer has a low permeability. The Layer 2 productivity is the same for both cases. The remaining layer properties are given in **Table 5.8**.

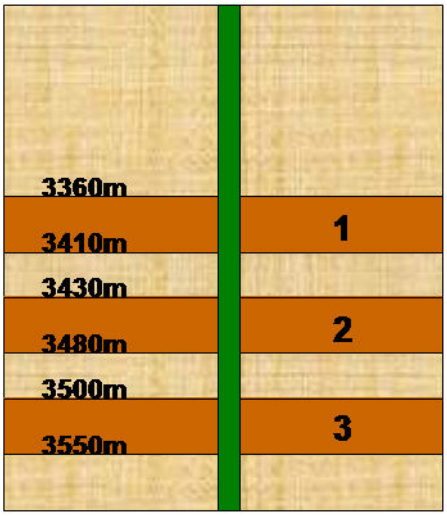

Fig. 5.34 Reservoir diagram for low productivity diagnosis

Table 5.8 Layer properties for low productivity diagnosis

	k (md)	k_s (md)	r_s (ft)	s
Case (a)				
Layer 1	30	-	-	0
Layer 2	20	1.5	0.63	10
Layer 3	20	-	-	0
Case (b)				
Layer 1	30	-	-	0
Layer 2	8	-	-	0
Layer 3	20	-	-	0

To induce a transient flow period, the surface flow rate is cut back to 4000 STB/d from 8000 STB/d for 24 hrs. The temperature versus time behavior for both cases is shown in **Fig. 5.35** and **Fig. 5.36**. We can see that the transient temperature responses for the two cases are quite distinct. If the low productivity in Layer 2 is due to positive skin, the temperature curve at the top of Layer 2 (3420m) shows a different slope from the temperature curves at 3550m and 3490m. Additionally, since the temperature at Layer 2 has an effect on the temperature at Layer 1, the temperature curve at 3350m is parallel to the 3420m temperature curve. If the Layer 2 has a low permeability, the temperature curve at each location would be parallel to each other, demonstrating that the low-

permeability situation can be easily differentiated from the skin situation. This result is important because in the case Layer 2 has a positive skin its productivity could be improved with matrix acidizing; while in the case Layer 2 has low permeability, its productivity could be improved by hydraulically fracturing the layer.

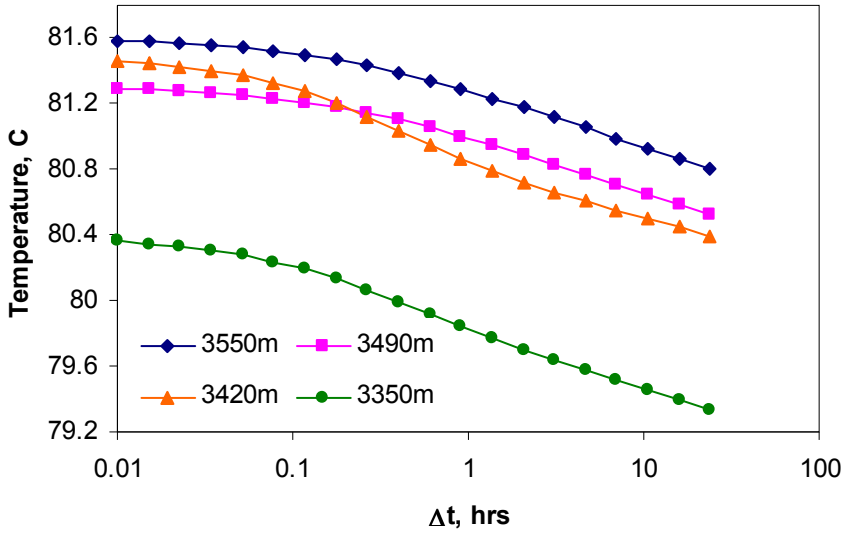

Fig. 5.35 Temperature history profiles for Case (a)

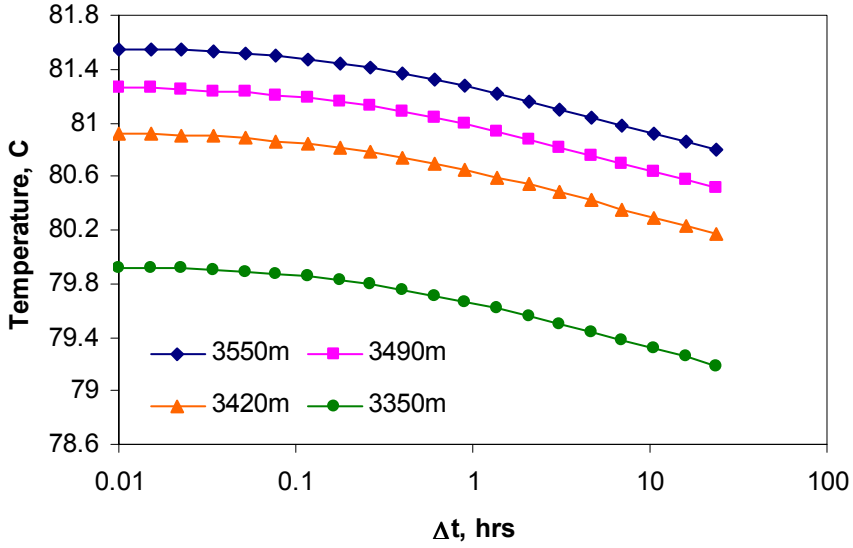

Fig. 5.36 Temperature history profiles for Case (b)

5.5 PRACTICAL IMPLICATION

5.5.1 Temperature Resolution and Noise Impact

For any testing approach, one of the most important things for practical applications is to understand the data resolution and the impact of noise on the interpretation results. The objective of this section is to quantify the required resolution and allowable noise level for the multilayer reservoir characterization, which can provide a lot more confidence in applying this new testing and analysis approach.

Regarding data rate, it is important to have usable measurements as early in time as 0.01 hr (36 s). We presume that the temperature sensors can only resolve the temperature change to some minimum discreet value denoted as the sensor resolution. The resolution value may vary greatly for different types of temperature sensors. To investigate the temperature resolution impact on this new testing approach, four different levels of resolution (σ = 0.001 ºC, 0.01 ºC, 0.1 ºC, and 0.2 ºC) have been introduced into the ideal temperature measurement data, which are predicted by forward model in hypothetical cases. The corresponding regression results are obtained using inverse simulator. The same reservoir and production rate schemes in Section 3.6 were used here for this investigation. The generated temperature data with different resolution values are shown in **Fig. 5.37** to **Fig. 5.40**.

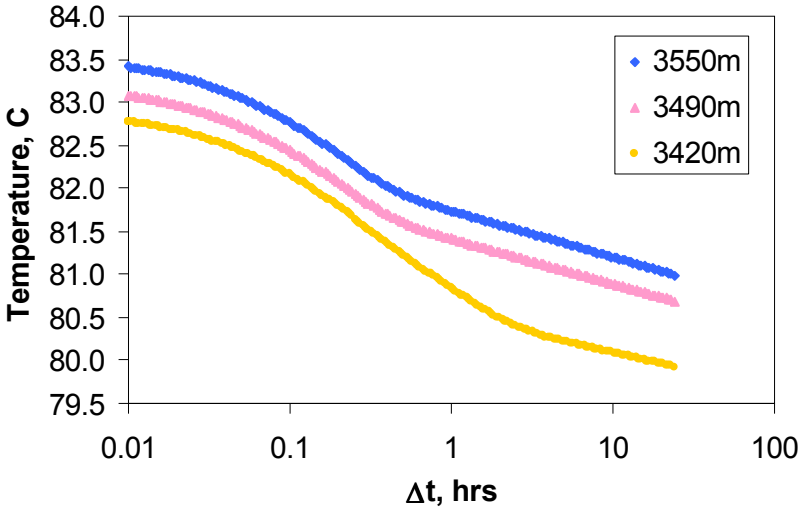

Fig. 5.37 Temperature data with resolution of 0.001 ºC

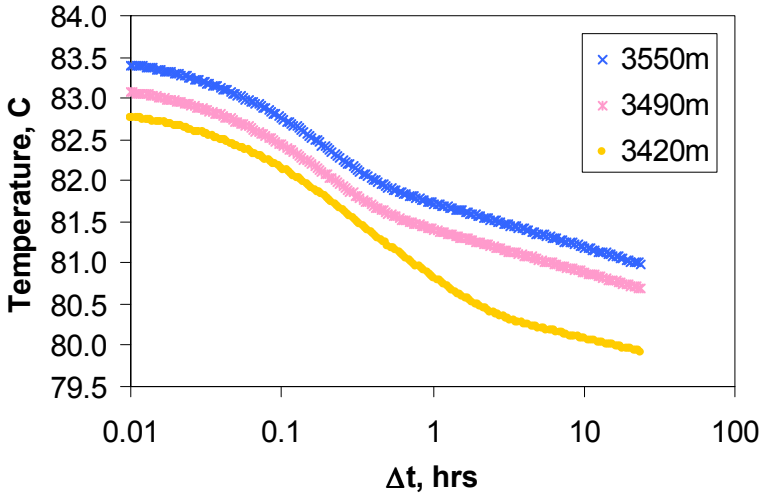

Fig. 5.38 Temperature data with resolution of 0.01 ºC

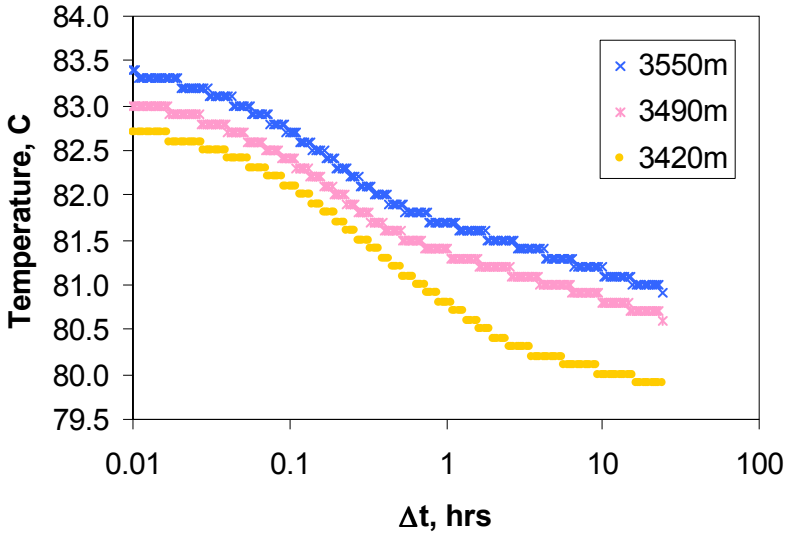

Fig. 5.39 Temperature data with resolution of 0.1 ºC

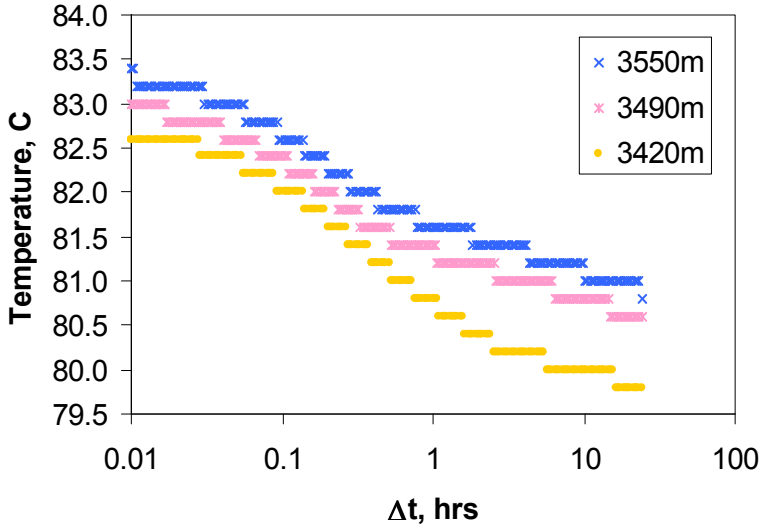

Fig. 5.40 Temperature data with resolution of 0.2 ºC

For the regression analysis, the data points were selected logarithmically as before. The regression results for different levels of noise are given in **Table 5.9**. We can see that the resolution of 0.001 °C or 0.01 °C only has a small impact on regression results and the results are still very close to the true values; the resolution of 0.1 °C

makes the regression results deviate from the true values, but the regression results are still very informative. However, when temperature resolution is up to 0.2 °C, the regression results are no longer reliable.

Table 5.9 Regression results for temperature data with different temperature resolution

	True values				Initial guesses				Regression results			
	k (md)	k_s (md)	r_s (ft)	s	k (md)	k_s (md)	r_s (ft)	s	k (md)	k_s (md)	r_s (ft)	s
σ = 0.001 °C												
Layer 1	100	14.4	1.45	10	75	4.7	0.4	5	100.06	14.4	1.45	9.997
Layer 2	60	13.1	0.63	3	75	4.7	0.4	5	59.99	13.1	0.63	3.0005
σ = 0.01 °C												
Layer 1	100	14.4	1.45	10	75	4.7	0.4	5	100.29	14.5	1.45	9.917
Layer 2	60	13.1	0.63	3	75	4.7	0.4	5	59.95	13.1	0.63	3.006
σ = 0.1 °C												
Layer 1	100	14.4	1.45	10	75	4.7	0.4	5	107.71	15.3	1.71	11.171
Layer 2	60	13.1	0.63	3	75	4.7	0.4	5	58.92	12.4	0.63	3.158
σ = 0.2 °C												
Layer 1	100	14.4	1.45	10	75	4.7	0.4	5	61.94	8.4	0.53	4.26
Layer 2	60	13.1	0.63	3	75	4.7	0.4	5	56.36	7.9	0.45	3.07

Besides the resolution impact, the original temperature signals contain noise, which can also harm the interpretation. To study the impact of the data noise, different levels of random noise (ε = 0.1 °C, 0.2 °C, and 0.5 °C) have been introduced into the temperature measurement data. For this case, we assume the resolution is 0.01 °C. The generated temperature data with different levels of noise are shown in **Fig. 5.41** to **Fig. 5.43**. The regression results are shown in **Table 5.10**. It can be seen that the data noise impact the interpretation results significantly. With the noise level of 0.1 °C, the regression results start deviating. When the noise level increases to 0.2 °C, the regression results deviate further but are still acceptable. However, when the noise level is up to 0.5 °C, the regression results are no longer informative. The sensitivity of interpretation results to data noise level results from the relatively small range of temperature variation. When the signal to noise ratio approaches 10% (for the layer with the least temperature variation), errors occur in the inverse solution. The same signal to noise concern applies for the pressure gauge, but in the cases presented here pressure changes

are sufficient that current gauge technology is easily adequate. For practical applications, the acceptable noise level should be determined by performing a sensitivity study of expected responses based on a range of expected permeability and skin values before selecting pressure and temperature sensors for each specific case. A larger flow surface rate change would improve the signal to noise behavior.

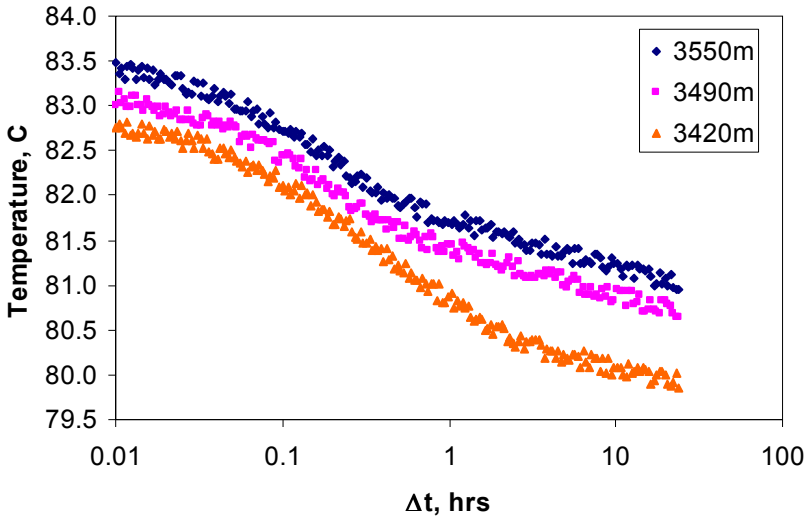

Fig. 5.41 Temperature data with noise (ε = 0.1 ºC)

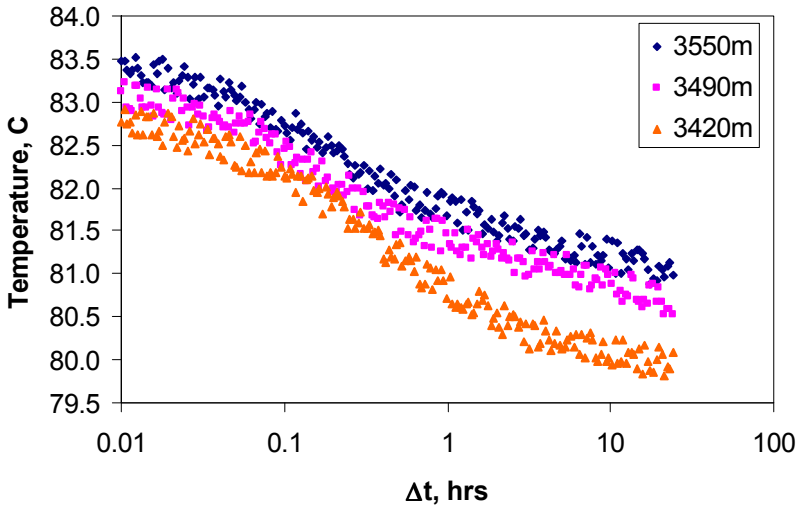

Fig. 5.42 Temperature data with noise (ε = 0.2 ºC)

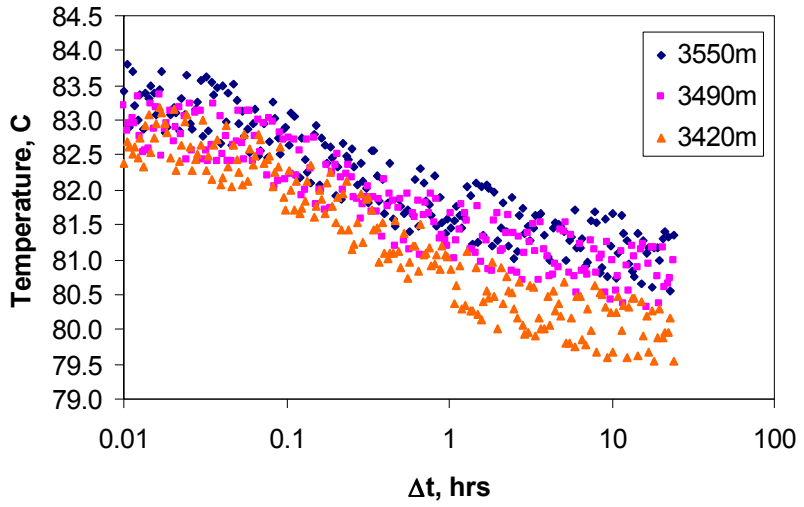

Fig. 5.43 Temperature data with noise (ε = 0.5 °C)

Table 5.10 Regression results for temperature data with different levels of noise

	True values				Initial guesses				Regression results			
	k (md)	k_s (md)	r_s (ft)	s	k (md)	k_s (md)	r_s (ft)	s	k (md)	k_s (md)	r_s (ft)	s
ε = 0.1 °C												
Layer 1	100	14.4	1.45	10	75	4.7	0.4	5	97.51	14.8	1.45	9.404
Layer 2	60	13.1	0.63	3	75	4.7	0.4	5	59.50	15.0	0.74	2.980
ε = 0.2 °C												
Layer 1	100	14.4	1.45	10	75	4.7	0.4	5	118.25	13.4	1.22	11.835
Layer 2	60	13.1	0.63	3	75	4.7	0.4	5	57.00	12.8	0.63	2.890
ε = 0.5 °C												
Layer 1	100	14.4	1.45	10	75	4.7	0.4	5	63.59	18.8	1.04	3.204
Layer 2	60	13.1	0.63	3	75	4.7	0.4	5	53.66	12.4	0.53	2.221

5.5.2 Improvements by Data Filtering

Data filtering is one of the major branches in digital signal processing field. Common methods include Moving Average Filtering, Savitzky-Golay Filtering and so on. Here, the Moving Average Filtering method is used for rejecting noise and improving the regression results. A moving average filter smoothes data by replacing each data point

with the average of the neighboring data points defined within the span, which can be represented by

$$y_s(i) = \frac{1}{2N+1}\left(y(i+N) + y(i+N-1) + \ldots + y(i-N)\right) \quad \text{.....5.3}$$

where $y_s(i)$ is the smoothed value for the ith data point, N is the number of neighboring data points on either side of $y_s(i)$, and $2N+1$ is the span.

To study the effects of data filtering, the case in the last section with a temperature noise level of 0.5 °C is used here for illustration. Given the span of 5, the temperature data are smoothed and shown in **Fig. 5.44**. It can be seen that the filtered temperature data become more informative.

With five selected time points during the transient test, the regression results are given in **Table 5.11**. We can see that the regression results after filtering have been improved significantly and are very close to the true values. This example indicates that data filtering is a crucial step in the new testing analysis. When data noise level is in an acceptable range and the data rate is high enough, data filtering can improve the interpretation accuracy significantly.

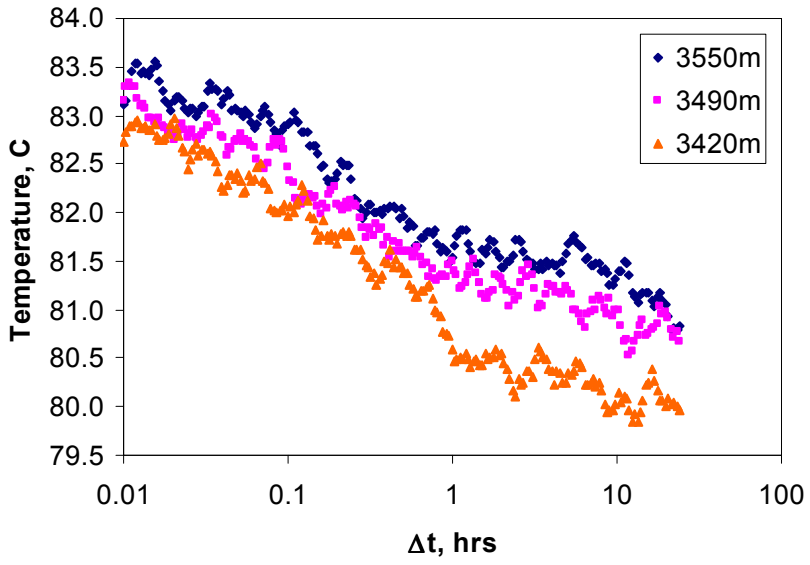

Fig. 5.44 Filtered temperature data (ε = 0.5 ºC), 200 data points during test

Table 5.11 Regression results for filtered temperature data (σ = 0.01 °C)

	True values				Initial guesses				Regression results			
	k (md)	k_s (md)	r_s (ft)	s	k (md)	k_s (md)	r_s (ft)	s	k (md)	k_s (md)	r_s (ft)	s
ε = 0.5 °C												
Layer 1	100	14.4	1.45	10	75	4.7	0.4	5	100.95	15.4	1.45	9.335
Layer 2	60	13.1	0.63	3	75	4.7	0.4	5	61.40	11.8	0.63	3.534

5.5.3 Data Rate Impact

Based on the preceding results, we can see that the early-time transient data measurement is essential to the later interpretations, which is because skin factor and permeability mainly affect temperature and pressure in early-time period. Therefore, data rate impact study is very important to practical applications. Since a logarithmic time step is adopted in our simulator, only the first time point is used for data rate impact study because it is the smallest time step during the test. The practical meaning of the first time point means the earliest time to start collecting data, which reflects the measurement speed of the temperature sensor.

A three-layer oil reservoir is used here for data rate studies and the reservoir diagram is shown in **Fig. 5.45**. The layer properties are listed in **Table 5.12**. A 24-hr transient test is induced by cutting back the surface flow rate from 8000 STB/d to 4000 STB/d. Given different start-time points from 0.0001 hr to 20 hrs, the corresponding regression results are shown in **Table 5.13**. The discrepancies between true values and estimated values are evaluated by *l*-2 norm which is defined as follows.

$$\|L\| = \sqrt{\sum_{j=1}^{3}\left(\frac{k_{j,true}-k_{j.inverted}}{k_{j,true}}\right)^2+\left(\frac{k_{s3,true}-k_{s3.inverted}}{k_{s3,true}}\right)^2+\left(\frac{r_{s3,true}-r_{s3.inverted}}{r_{s3,true}}\right)^2} \quad ..5.4$$

To find out the possible relationship between the *l*-2 norm and the temperature change derivatives, the *l*-2 norm values for each case are drawn in the temperature change derivative plot in **Fig. 5.46** and represented by the maroon points. For our studied cases, successful regression results usually appear with an $\|L\|$ smaller than 1.0.

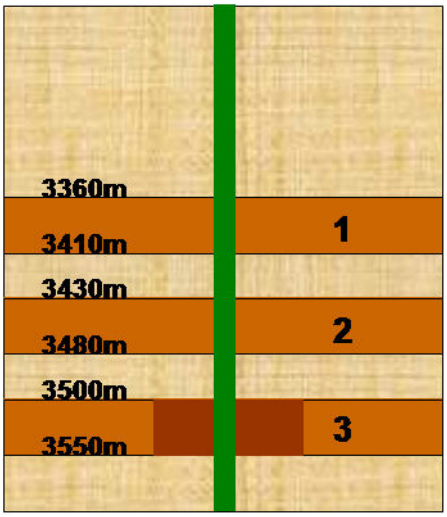

Fig. 5.45 Reservoir diagram for studying data rate impact

Table 5.12 Layer properties for data rate studies

	k (md)	k_s (md)	r_s (ft)	s
Layer 1	30	-	-	0
Layer 2	30	-	-	0
Layer 3	30	5.4	2.4	10

It can be seen clearly that the optimum start-time point is 2.5 hrs, which is very close to the peak of the temperature change derivative curve for Layer 3. Also, several better regressions are all around the peak point, which indicates that the regression results are related to the temperature change derivative curves. According to preceding discussions, we know that the peak of the temperature change derivative curves is determined by the damage radius. Therefore, we can draw the conclusion that regression results are related to the damage radius. The optimum start-time point possibly depends on the damage radius. This idea can be proved by using another two cases with different damage radius. Compared with the large damage radius used above, we studied a medium and a small damage radius case respectively. The optimum start-time point for three cases are shown from **Fig. 5.47** to **Fig. 5.49**, and we can see that the optimum start-time points always appear around the peak of temperature change derivative curves.

Therefore, this phenomenon indicates that the required data rate related to the specific damage radius in practical cases and it is more possible to get successful inversion around the peak of the temperature change derivative curves.

Table 5.13 Regression results for different start-time cases

t_0, hrs	k_1	k_2	k_3	k_{s1}	k_{s2}	k_{s3}	r_{s1}	r_{s2}	r_{s3}	s_1	s_2	s_3	f(t)	||L||
(True value)	30.0	30.0	30.0	-	-	5.4	-	-	2.39	0.000	0.000	10.000		
0.0001	30.5	31.6	30.5	27.5	31.6	1.9	0.38	2.39	0.63	0.037	0.004	12.629	1.36E+11	0.98
0.001	30.4	32.0	31.5	31.4	29.4	2.0	0.53	2.39	0.63	-0.021	0.188	12.335	6.47E+10	0.97
0.01	30.5	31.1	31.6	234.7	30.5	2.4	0.27	2.39	0.74	0.000	0.043	12.482	4.22E+10	0.89
0.1	30.4	31.5	35.6	35.5	30.1	2.2	0.38	2.39	0.74	-0.049	0.105	15.115	6.05E+10	0.93
1	30.0	30.4	31.5	26.1	31.7	2.9	0.32	2.39	0.88	0.025	-0.092	11.370	9.45E+09	0.78
2	30.2	30.2	31.0	32.2	30.2	3.0	0.38	2.39	0.88	-0.021	0.001	11.084	7.99E+09	0.78
2.1	30.0	30.9	31.9	26.7	58.7	3.5	0.32	0.38	1.22	0.021	-0.158	12.268	8.74E+09	0.60
2.3	30.0	30.9	31.8	25.8	59.8	3.5	0.32	0.38	1.22	0.027	-0.162	12.181	8.64E+09	0.60
2.5	30.0	30.0	30.0	30.1	315.0	5.4	2.39	0.27	2.39	-0.005	0.000	10.003	11682350	0.00
2.7	30.1	31.0	30.4	323.9	33.1	3.2	0.27	2.39	1.04	0.000	-0.136	11.500	1.17E+10	0.70
2.9	30.4	30.3	30.4	30.4	162.2	4.4	2.02	0.27	1.45	-0.003	0.000	9.813	1.12E+10	0.43
3	30.2	30.4	30.1	33.8	31.6	2.9	0.32	2.39	0.88	-0.018	-0.087	10.856	4.29E+09	0.78
4	45.3	44.5	30.4	6.4	5.3	1.0	0.38	0.38	0.38	2.045	2.467	9.864	3.12E+18	1.37
5	42.8	46.2	34.5	6.0	5.7	1.0	0.38	0.38	0.38	2.042	2.405	11.246	3.12E+18	1.37
6	41.5	52.0	24.3	6.8	3.3	1.0	0.38	0.38	0.38	1.716	4.893	7.802	3.12E+18	1.45
7	39.1	4408.0	9.0	7.5	2.0	1.0	0.38	0.38	0.38	1.423	753.943	2.673	3.12E+18	145.94
8	38.2	2359.1	8.1	8.0	2.0	1.0	0.38	0.38	0.38	1.261	394.570	2.381	3.12E+18	77.65
9	38.9	41.3	43.5	7.0	7.3	1.0	0.38	0.38	0.38	1.520	1.559	14.246	3.12E+18	1.34
10	35.3	41.9	24.6	9.6	8.3	1.5	0.38	0.38	0.53	0.897	1.356	10.476	2.10E+11	1.16
20	37.1	49.5	26.2	7.7	7.3	1.0	0.38	0.45	0.45	1.274	2.895	12.511	4.85E+11	1.35

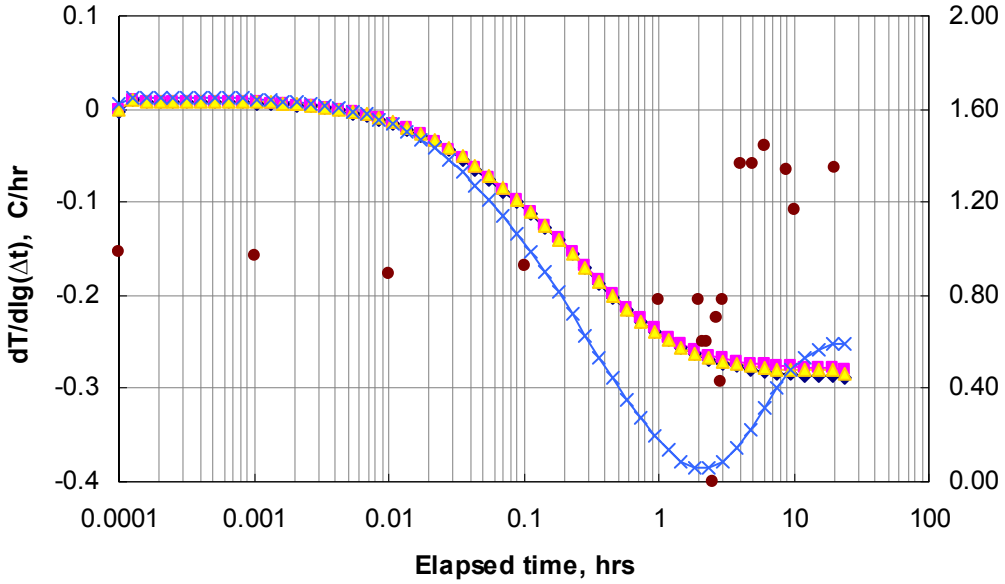

Fig. 5.46 Absolute error values of the estimated permeability on temperature derivative curves for different start-time data points

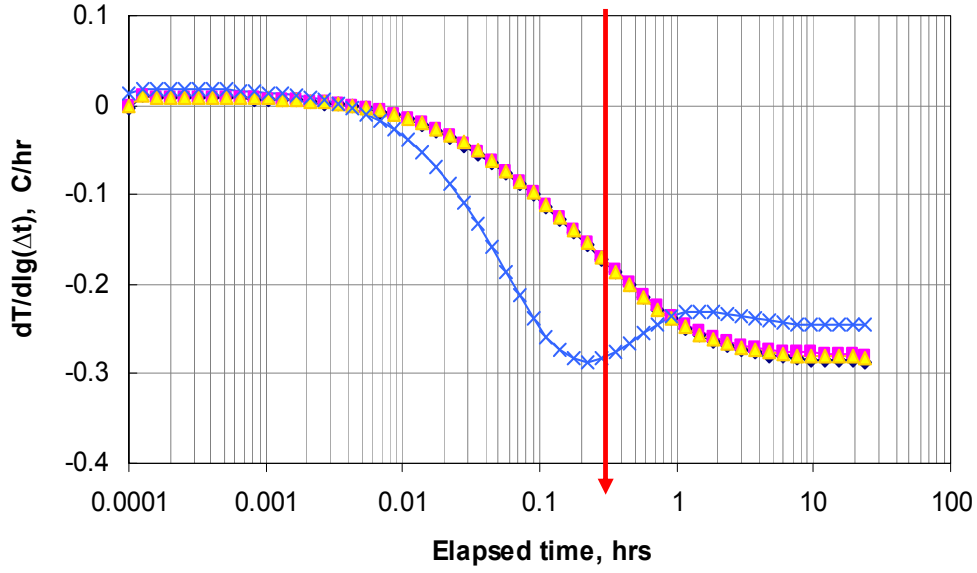

Fig. 5.47 Last start data point for inversing formation properties (r_s = 0.45ft)

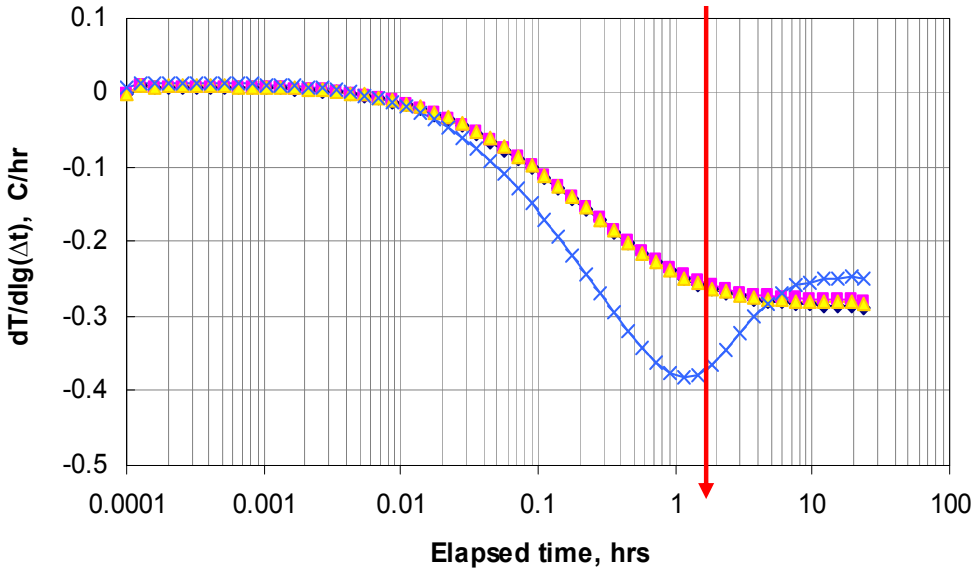

Fig. 5.48 Last start data point for inversing formation properties (r_s = 1.04ft)

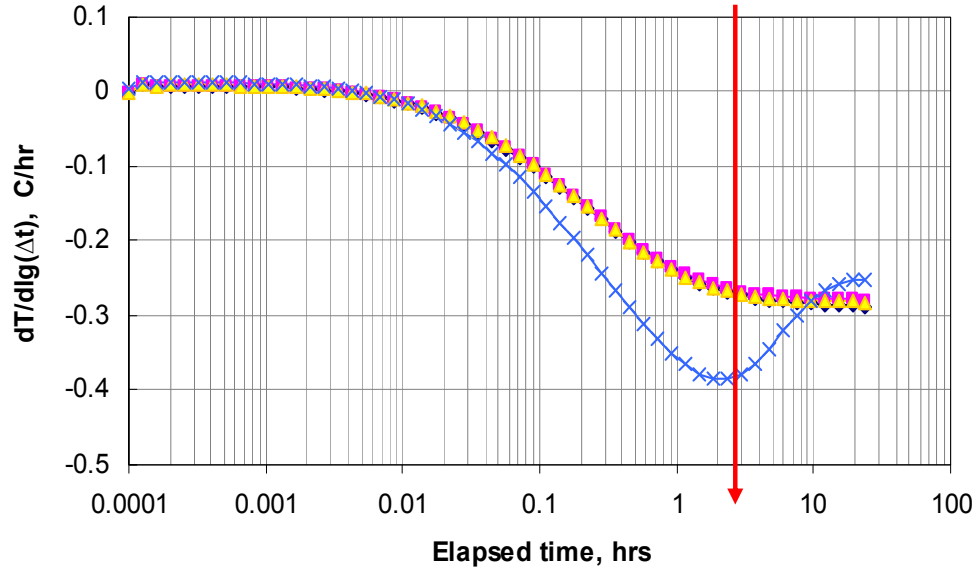

Fig. 5.49 Last start data point for inversing formation properties (r_s = 2.39ft)

6 CONCLUSIONS

A new testing approach has been proposed for multilayer reservoir characterization. The testing procedure has been presented, and the derivation of the model required for the test interpretation has been described in detail.

The developed forward model is used to simulate the wellbore and reservoir temperature and pressure profiles during the proposed test period, and mechanisms for transient temperature variation have been investigated in detail and used to study the effects of formation properties on transient temperature behavior.

Feasibility studies show that the skin factor and permeability affect transient temperature behavior differently, and justify why individual layer permeability and skin factor may be determined using transient temperature and pressure measurements during a single step change in the surface rate. An especially important finding is that the temperature response is sensitive not just to skin, but to the damage radius and permeability. This determination cannot be made from pressure and rate measurements. Additionally, the response for a low productivity layer depends whether the reason for low productivity is damage or low layer permeability, thus showing the potential of this new testing method to be used for explaining low-productivity.

With the developed forward model, the inverse model has also been formulated based on Levenberg-Marquardt algorithm. The inverse model is used to evaluate formation properties by minimizing the discrepancy between measured data and simulated data.

For the hypothetical cases, the proposed new multilayer testing method has successfully been applied for investigating formation properties in commingled multilayer reservoirs. The interpretations can also be successful with wellbore storage effects. Layer permeability, damage permeability, and damage radius can be uniquely determined using single-point transient pressure data and multipoint transient temperature data at appropriate locations. Due to the proposed data acquisition scheme,

only one surface flow rate change is needed to implement this testing approach, which significantly reduces the test duration compared to the standard multilayer transient testing approach using a series of flow rate changes. Of special interest, this is the first test design that shows promise for determination of the damage radius, which can be useful for well stimulation design. The developed model proved to be robust for a four-layer commingled reservoir with complicated layer property information and wellbore storage effect.

The potential impact of resolution, data noise, and data rate on the presented testing technique has also been explored. The study results indicate that temperature resolution, data noise level, and data rate have a significant impact on the interpretation results, and that data filtering can be effective in improving the interpretation accuracy at relatively high signal to noise level.

REFERENCES

Bird, R.B., Stewart, W.E., and Lightfoot, E.N. 2002. *Transport Phenomena*, New York: John Wiley and Sons.

Brown, G., Storer D., McAllister, K., al-Asimi, M., and Raghavan, K. 2003. Production Monitoring Through Openhole Gravel-Pack Completions Using Permanently Installed Fiber-Optic Distributed Temperature Systems in the BP-Operated Azeri Field in Azerbaijan. Paper SPE 84379 presented at the SPE Annual Technical Conference and Exhibition, Denver, Colorado, 5-8 October.

Brown, G., Field, D., Davies, J., Collins, P., and Garayeva, N. 2005. Production Monitoring Through Openhole Gravel-Pack Completions Using Permanently Installed Fiber-Optic Distributed Temperature Systems in the BP-Operated Azeri Field in Azerbaijan. Paper SPE 95419 presented at the SPE Annual Technical Conference and Exhibition, Dallas, Texas, 9-12 October.

Carnahan, B. D., Clanton, R.W., Koehler, K.D., and Williams, G.R. 1999. Fiber Optic Temperature Monitoring Technology. Paper SPE 54599 presented at the SPE Western Regional Meeting, Anchorage, Alaska, 26-27 May.

Carslaw, H.S. and Jaeger, J.C. ed. 1959. *Conduction of Heat in Solids*. London: Oxford University Press.

Ehlig-Economides, C. A. 1987. A New Test for Determination of Individual Layer Properties in a Multilayered Reservoir. *SPE Form Eval* **2** (3): 261-283. SPE-14167-PA.

Fryer, V., Deng, S., Otsubo, Y., Brown, G., and Guilfoyle, P. 2005. Monitoring of Real-Time Temperature Profiles Across Multizone Reservoirs During Production and Shut-in Periods Using Permanent Fiber-Optic Distributed Temperature Systems. Paper SPE 92962 presented at the SPE Asia Pacific Oil & Gas Conference and Exhibition, Jakarta, Indonesia, 5-7 April.

Grattan, K.T.V. and Sun, T. 2000. Fiber Optic Sensor Technology: An Overview. *Sensor and Actuators A: Physical* **82**: 40-61.

Hasan, A.R. and Kabir, C.S. 1991. Heat Transfer During Two-Phase Flow in Wellbores: Part I – Formation Temperature. Paper SPE 22866 presented at the SPE Annual Technical Conference and Exhibition, Dallas, 6-9 October.

Hill, A.D. 1990. *Production Logging–Theoretical and Interpretive Elements*, Monograph Series, SPE, Richardson, Texas **1**: 14-19.

Horner, D.R. 1967. *Pressure Buildup in Wells*. Reprint series, SPE, Richardson, Texas **9**: 25-43.

Johnson, D., Sierra, J., Kaura, J., and Gualtieri D. 2006. Successful Flow Profiling of Gas Wells Using Distributed Temperature Sensing Data. Paper SPE 103097 presented at the 2006 SPE Annual Technical Conference and Exhibition, San Antonio, Texas, 24-27 September.

Kragas, T. K., Williams, B. A. and Myers, G. A. 2001. The Optic Oil Field: Deployment and Application of Permanent In-Well Fiber Optic Sensing Systems for Production and Reservoir Monitoring. Paper SPE 71529 presented at the SPE Annual Technical Conference and Exhibition, New Orleans, Louisiana, 30 September-3 October.

Kuchuk, F., Karakas, M., and Ayestaran, L. 1986a. Well Testing and Analysis Techniques for Layered Reservoirs. *SPE Form Eval* **1** (4): 342-354. SPE-13081-PA.

Kuchuk, F. J., Shah, P.C., Ayestaran, L., and Nicholson, B. 1986b. Application of Multilayer Testing and Analysis: A Field Case. Paper SPE 15419 presented at the SPE Annual Technical Conference and Exhibition, New Orleans, LA, 5-8 October.

Kuchuk, F. J. and Wilkinson, D.J. 1991. Transient Pressure Behavior of Commingled Reservoirs. *SPE Form Eval* **6** (1): 111-120. SPE-18125-PA.

Lanier, G.H., Brown, G., and Adam, L. 2003. Brunei Field Trial of a Fiber Optic Distributed Temperature Sensor (DTS) System in a 1,000m Open Hole Horizontal Oil Producer. Paper SPE 84324 presented at the SPE Annual Technical Conference and Exhibition, Denver, Colorado, 5-8 October.

Larsen, L. 1999. Determination of Pressure-Transient and Productivity Data for Deviated Wells in Layered Reservoirs. *SPE Res Eval & Eng* **2** (1): 95-103. SPE-54701-PA.

Lefkovits, H. C. 1961. A Study of the Behavior of Bounded Reservoirs Composed of Stratified Layers. *SPE J.* **1** (1): 43-58. SPE-1329-G.

Mahrooqi M., Hinai G., Kuchel, M., and Al Sakhbouri, H. 2007. Detecting Water Influx in Beam Pump Lifted Horizontal Wells in a South Oman Field Using Temperature Measurements, Production Profiling, and Concentric Coiled Tubing. Paper SPE 110161 presented at the 2007 SPE Asia Pacific Oil and Gas Conference and Exhibition, Jakarta, Indonesia, 30 October-1 November.

Manrique, J.F. and Poe, B.D. 2007. A Unique Methodology for Evaluation of Multi-Fractured Wells in Stacked-Pay Reservoirs Using Commingled Production and Rate Transient Analysis. Paper SPE 110576 presented at the SPE Annual Technical Conference and Exhibition, Anaheim, California, 11-14 November.

Maubeuge, F., Didek, M.P., and Beardsell, M.B. 1994a. Temperature Model for Flow in Porous Media and Wellbore. Paper presented at SPWLA Annual Logging Symposium, 19-22 June.

Maubeuge, F., Didek, M.P., Beardsell, M.B., Arquis, E., Bertrand, O., and Caltagirone, J.P. 1994b. MOTHER: A Model for Interpreting Thermometrics. Paper SPE 28588 presented at the SPE Annual Technical Conference and Exhibition, New Orleans, LA, 25-28 September.

Nath, D.K., Sugianto, R., and Finley, D. 2007. Fiber-Optic Distributed –Temperature-Sensing Technology Used for Reservoir Monitoring in a Indonesia Steamflooding. *SPE Drill & Compl* **22**(2): 149-156. SPE 97912.

Ouyang, L. and Belanger, D. 2006. Flow Profiling via Distributed Temperature Sensor (DTS) System – Expectation and Reality. *SPE Prod & Oper* **21** (2): 269-281. SPE-90541-PA.

Pinzon, I. D., Davies, J.E., Mammadkhan, F., and Brown, G.A. 2007. Monitoring Production From Gravel-Packed Sand-Screen Completions on BP's Azeri Field Wells Using Permanently Installed Distributed Temperature Sensors. Paper SPE 110064 presented at the SPE Annual Technical Conference and Exhibition, Anaheim, California, 11-14 November.

Poe, B. D., Atwood, W.K., and Kohring, J. et al. 2006. Evaluation of Commingled Reservoir Properties Using Production Logs. Paper SPE 104013 presented at the International Oil Conference and Exhibition in Mexico, Cancun, Mexico, 31 August-2 September.

Prats, M. and Vogiatzis, J.P. 1999. Calculation of Wellbore Pressures and Rate Distribution in Multilayered Reservoirs. *SPE J.* **4** (4): 307-314. SPE-57241-PA.

Ramey, H.J. Jr. 1962. Wellbore Heat Transmission. *J. Pet Tech* **14** (4): 427-435; *Trans.*, AIME, 225. SPE-96-PA.

Sagar, R., Doty, D.R., and Schmldt, Z. 1991. Predicting Temperature Profiles in a Flowing Well. *SPE Prod Eng* **6** (4): 441-448. SPE-19702-PA.

Satter, A. 1965. Heat Losses During Flow of Steam Down a Wellbore. *J. Pet Tech* **17** (7): 845-851; *Trans.*, AIME, 234. SPE-1071-PA.

Schlumberger, M., Doll, H.G., and Perebinossoff, A.A. 1937. Temperature Measurements in Oil Wells. *JIPT* **23** (159): 1.

Shah, P. C., Karakas, M., Kuchuk, F., and Ayestaran, L. C., 1988. Estimation of the Permeabilities and Skin Factors in Layered Reservoirs With Downhole Rate and Pressure Data. *SPE Form Eval* **3** (3): 555-565. SPE-14131-PA.

Spath, J. B., Ozkan, E., and Raghavan, R. 1994. An Efficient Algorithm for Computation of Well Responses in Commingled Reservoirs. *SPE Form Eval* **9** (2): 115-121. SPE-21550-PA.

Spivey, J.P. 2006. Estimating Layer Properties for Wells in Multilayer Low-Permeability Gas Reservoirs by Automatic History-Matching Production and Production Log Data. Paper SPE 100509 presented at the SPE Gas Technology Symposium, Calgary, Alberta, Canada, 15-17 May.

Steffensen, R.J. and Smith, R.C. 1973. The Importance of Joule-Thomson Heating (or Cooling) in Temperature Log Interpretation. Paper SPE 4636 presented at the Annual Fall Meeting of AIME, Las Vegas, Nevada, 30 September – 3 October.

Stehfest, H. 1970. Algorithm 368, Numerical Inversion of Laplace Transforms. D-5 communications, *ACM* **13** (1): 47-49.

Tolan, M., Boyle, M., and Williams, G. 2001. The Use of Fiber-Optic Distributed Temperature Sensing and Remote Hydraulically Operated Interval Control Valves for the Management of Water Production in the Douglas Field. Paper SPE 71676 presented at the SPE Annual Technical Conference and Exhibition, New Orleans, Louisiana, 30 September-3 October.

Yoshioka, K., Zhu, D., Hill, A.D., and Lake, L. 2005a. Interpretation of Temperature and Pressure Profiles Measured in Multilateral Wells Equipped With Intelligent Completion. Paper SPE 94097 presented at the SPE/EAGE Annual Conference, Madrid, Spain, 13-16 June.

Yoshioka, K., Zhu, D., Hill, A.D. Dawkrajai, P., and Lake, L.W. 2005b. A Comprehensive Model of Temperature Behavior in a Horizontal Well. Paper SPE 95656 presented at the SPE Annual Technical Conference and Exhibition, Dallas, Texas, 9-12 October.

Yoshioka, K. 2007. Detection of Water or Gas Entry into Horizontal Wells by Using Permanent Downhole Monitoring System. PhD dissertation, Texas A&M U., College Station, TX.

Yoshioka, K., Zhu, D., and Hill, A.D. 2007a. A New Inversion Method to Interpret Flow Profiles From Distributed Temperature and Pressure Measurements in Horizontal Wells. Paper SPE 109749 presented at the SPE Annual Technical Conference and Exhibition, Anaheim, California, 11-14 November.

Yoshioka, K., Zhu, D., Hill, A.D., Dawkrajai, P., and Lake, L.W. 2007b. Prediction of Temperature Changes Caused by Water or Gas Entry Into a Horizontal Well. SPEPO 22 (4): 425-433. SPE-100209-PA.

VITA

Name:	Weibo Sui
Address:	EOR Center, China University of Petroleum, 18 Fuxue Road, Changping District, Beijing, China 102249
Email Address:	suiweibo@gmail.com
Education:	B.S., Petroleum Engineering, China University of Petroleum, 2003 M.S., Petroleum Engineering, China University of Petroleum, 2005 Ph.D., Petroleum Engineering, Texas A&M University, 2009